TOWARD A DURABLE, SMALL DIAMETER TISSUE ENGINEERED VASCULAR GRAFT: UNDERSTANDING THE UTILITY OF SURFACE MICROPATTERNING AND MAXIMIZING THE VALUE OF REAL-TIME EX VIVO THROMBOSIS TESTING

By

Matthew Walker Hagen

B.A., Reed College, 2011

A DISSERTATION

Presented to the Department of Biomedical Engineering
of the Oregon Health & Science University School of Medicine
in partial fulfillment of the requirements for the degree
of Doctor of Philosophy in Biomedical Engineering

December 2019

School of Medicine

Oregon Health & Science University

Certificate of Approval

This is to certify that the Ph.D. Dissertation of

Matthew W. Hagen

"*Toward a durable, small diameter tissue engineered vascular graft: understanding the utility of surface micropatterning and maximizing the value of real-time ex vivo thrombosis testing.*"

Has been approved

_____

Mentor: Monica Hinds, Ph.D

_____

Member/Chair: George Giraud, MD., Ph.D

_____

Member: Carolyn Ibsen, Ph.D

_____

Member: Owen McCarty, Ph.D

_____

Member: Anthony Barnes, Ph.D.

_____

Acknowledgments

Before and above anyone else, I owe the completion of this degree to my adviser, Dr. Monica Hinds, who has showed me what kind, compassionate, functional, and productive leadership in academic medicine can look like. Over the past four and a half years Monica has been a completely fabulous adviser, mentor, boss, program director, role model, and friend. I cannot thank her enough for the opportunities she's given me to learn new techniques, participate in a diverse range of projects, and travel for conferences. I am so grateful for all of the time, patience, and guidance she's given me during my time in her lab and in the BME program.

I also owe a great deal to the members of the Hinds lab past and present: Dr. Deirdre Anderson, Dr. Jeremy Glynn, Dr. Katie Truong, Dr. Patrick Jurney, Novella Bates, Taylor Lawson, Jennifer Johnson, Tiffany Burch, and Meghan Fallon. All of these people are brilliant scientists, and many of them have become trusted friends. I particularly want to acknowledge Deirdre, who has been a constant during my time in the lab and who has been consistently available for questions, training, and long afternoon conversations about everything from statistics to professionalism and career development.

I am incredibly grateful for my dissertation advisory committee: Dr. George Giraud, Dr. Anthony Barnes, and Dr. Owen McCarty. They have been a constant source of knowledge, wisdom, and guidance both individually and during our DAC meetings over the last three years. I also want to thank Dr. Wohaib Hasan who was briefly a committee member before departing OHSU, and Dr. Carolyn Ibsen, who joined the committee as an external reviewer for my defense.

I appreciate the help, guidance, and friendship of the members of the McCarty-Gruber-Aslan supergroup: Dr. Andras Gruber, Dr. Joe Aslan, Dr. Cristina Puy Garcia, Dr. Laura Healy, Dr. Annachiara Mitrugno, Dr. Jenya Zilberman-Rudenko, Dr. Rachel Rigg, Dr. Christina Lorentz, Dr. Norah Verbout, Anh Ngo, Stephanie Reitsma, Hari Hara Sudhan Lakshmanan, Jiaqing Pang, and Alex Melrose. Thank you for all of your assistance with all things relating to blood, platelets, and beefcake.

There are numerous others from across OHSU and OSU who I also need to thank: Dr. Kent Thornburg, Dr. Sam Louey, and the rest of the EDOD group for allowing

me to be a part of the guinea pig project, Sharon Kryger, Dr. Ali Keyhan, Dr. Howard Song, and Dr. Jai Raman for their roles in the surgical innovation internship in the summer of 2016, Dr. Stefanie Kaech Petrie and Dr. Crystal Chaw for all of their help with confocal microscopy and for running the most fabulous and functional core facility I've ever seen, Dr. Jackie Wirz for everything she does for graduate studies, Dr. Alison Hill for encouraging my love of R and statistics, Dr. Jack Ferracane for use of and assistance with his SEM, Chris Tasker and Rick Presley of the OSU MASC facility for their assistance with photolithography, Eric Salkeld for his motivational yelling and sick beats, Virginia Howard for being endlessly available for questions during my first three years, Catherine Hogan for her assistance with grants, and Erica Hankins-Regalo for her constant and able help as program coordinator, and her encouraging words while I was writing and preparing to defend this dissertation.

I am lucky to have had the love and support of numerous close friends who similarly made the dubious life choice to pursue their Ph.D.s. Their commiseration and kind words were always particularly helpful, especially during difficult periods. Thank you to (soon to be Dr.) Scotland Farley, Dr. Ilsa Kirby, Dr. Jean McMahon, Dr. Brent Woo, Dr. Zara Weinberg, and Dr. Laurel Oldach.

I would never have been able to get to or through graduate school without the love and support of my family. Thank you to my parents, Ruth and Dana Hagen, my brother Ben Hagen, and my grandmother Rita Buttolph. I particularly want to thank my partner, Antonia Heffelfinger, who has been with me from my (multiple) decisions to postpone graduate school, through this entire process, and on into the future. Her love and companionship and patience with busy weekends, late nights, and conference travel has meant the world to me and I could not have done this without her.

Thank you again to everyone listed above, and to the several people I'm sure I'm forgetting.

List of Abbreviations

CAD	Coronary artery disease
PAD	Peripheral artery disease
BMS	Bare metal stent
ePTFE	Expanded polytetrafluoroethylene
SMC	Smooth muscle cell
ECM	Extracellular matrix
EC	Endothelial cell
GAG	Glycosaminoglycan
eNOS	Endothelial nitric oxide synthase
VE-Cadherin	Vascular endothelial cadherin
PECAM-1	Platelet endothelial cell adhesion molecule-1
ICAM-1	Intercellular adhesion molecule-1
VCAM-1	Vascular cell adhesion molecule
JAM	Junctional adhesion molecule
vWF	Von Willebrand factor
NO	Nitric oxide
F	(clotting) Factor
TFPI	Tissue factor pathway inhibitor
PAI-1	Plasminogen activator inhibitor-1
HUVEC	Human umbilical vein endothelial cell
KLF-2	Krüppel-like factor-2
NF-κB	Nuclear factor κ-light-chain-enhancer of activated B cells
VEGFR2	Vascular endothelial growth factor receptor-2
GTPase	Guanosine triphosphatase
EPC	Endothelial progenitor cell
MAC	Myeloid angiogenic cell
ECFC	Endothelial colony forming cell
TNF	Tumor necrosis factor α
ASA	Acetylsalicylic acid (Aspirin)
DAPT	Dual antiplatelet therapy

CaEC	Carotid endothelial cell
PBS	Phosphate buffered saline
PS	Penicillin-streptomycin
EBM	Endothelial basal medium
FBS	Fetal bovine serum
ACD	Acid citrate dextrose
PDMS	Polydimethyl siloxane
UV	Ultraviolet
SI	Shape index
AR	Aspect ratio
qPCR	Quantitative real-time polymerase chain reaction
GAPDH	Glyceraldehyde 3-phosphate dehydrogenase
ID	Inner diameter
OD	Outer diameter
LTPA	Light transmission platelet aggregometry
PRP	Platelet rich plasma
PPP	Platelet poor plasma
BSA	Bovine serum albumin
SRM	Super-resolution microscopy
PVA	Poly(vinyl alcohol)
SEM	Scanning electron microscope
SD	Standard deviation
LME	Linear mixed effects
ANOVA	Analysis of variance
PED	Pipeline embolization device
FRED™	Flow redirection endoluminal device

Table of Contents

List of Tables

List of Figures

Abstract

Durable artificial small-diameter vascular grafts are a critical unmet need in a medical landscape where advanced cardiovascular diseases remain the leading causes of morbidity and mortality. As classical approaches based on maximizing biomaterial inertness have failed to overcome the thrombosis and hyperplasia that drive device failure, novel solutions inspired by the function of the native endothelium are necessary. Biomaterial devices designed for rapid *in vitro* or *in situ* endothelialization, and devices designed to mimic endothelial function are all active areas of study which will be addressed within this dissertation. Endothelial colony forming cells are an incompletely understood blood outgrowth product with tremendous potential for tissue engineering applications. This dissertation includes the novel characterization of the sensitivity of these cells to flow-independent morphological modulations, which will add to the understanding of their suitability for use in tissue engineered grafts. Additionally, using an established flowing whole-blood platform, the material thrombogenicity of novel *in situ* endothelializable grafts and biomolecule-modified cerebral flow diverters was quantified. Throughout this dissertation, novel analytical strategies were developed to optimize the utility of quantitative imaging modalities. This dissertation aims to improve the current understanding of both cell biology toward the development of artificial vascular graft technologies, and of assessments of material thrombogenicity, toward the development and preclinical testing of *in situ* endothelializable and biomimetic blood-contacting devices.

Chapter I: Background

1.1 Advanced atherosclerosis and its treatment

Cardiovascular diseases remain leading causes of morbidity and mortality in the United States. In particular, coronary artery disease (CAD) and peripheral artery disease (PAD) combined account for around 1.1 million hospitalizations and 110,000 fatalities annually in the US [1]. Atherosclerosis, a leading cause of CAD and PAD, is the gradual thickening and hardening of arterial walls. It is an irreversible condition initiated by endothelial inflammation and the resulting movement of macrophages into the subendothelial intima, and progresses as the macrophages develop into foam cells and consume circulating low density cholesterol, eventually forming fatty plaques [2]. In its advanced state, atherosclerosis can cause critical stenosis or embolic plaque rupture, both of which can be life threatening.

Because atherosclerosis is non-reversible, advanced cases are treated through either stenting or grafting. Stenting is an interventional approach in which balloon angioplasty is used to recanalize a stenosed vessel and a stent, traditionally a bare metal scaffold, is placed to maintain revascularization. In order to address the thrombotic risk caused by bare metal stent (BMS) use, newer generations of stents which are either composed of antiproliferative polymers or are drug-eluting have been developed, yet these still carry a significant risk of late-term thrombosis and restenosis [3]. In contrast, vascular

grafting is a surgical procedure employing either an autologous or artificial blood vessel to bridge a stenosed artery.

Arterial grafting is generally performed using patient autologous vasculature. For coronary artery bypass grafts, the internal mammary artery and saphenous vein are preferred. Artificial vascular grafts, including those made from dacron or expanded polytetrafluoroethylene (ePTFE) are options for larger-diameter peripheral applications, however autologous vessels are preferred even for these applications. A longitudinal study of patients receiving lower limb bypass grafts found far greater patency and limb salvage in the first three years after surgery in patients receiving autologous saphenous vein grafts relative to those with ePTFE grafts [4]. Importantly, a substantial portion of the graft-eligible patient population lacks suitable donor tissue due to limited availability or donor site morbidity [5], emphasizing the need for novel solutions.

The patency of artificial vascular grafts is generally limited by two mechanisms: biomaterial-induced thrombosis in the short term, and intimal hyperplasia in the longer term. This dissertation is primarily motivated by two key ideas: first that the establishment of a healthy, functional endothelium on an artificial graft can regulate or prevent thrombosis and hyperplasia, and second that a full understanding of the dynamics of thrombosis on a material is a key predictor of its *in vivo* performance. In order to fully understand both these failure mechanisms, and the importance of endothelialization and thrombus quantification on graft development, it is first necessary to review the underlying biology of the blood and vasculature that drive them.

1.2 Vascular biology

The mammalian vascular system is incredibly diverse, ranging from the aorta and the major arteries it gives rise to, to the specialized capillary networks supplying organs and tissues, to the components of the venous and lymphatic systems. The advent of transcriptomic and proteomic analyses of the vascular tree have brought attention to this diversity and the important variations in endothelial morphology and function that exist across different vascular beds [6]. While this variability is a critical feature of vascular biology, this dissertation will focus on the anatomy and physiology of the major arteries.

1.2.1 Components of the vasculature

The major arteries are composed of three histologically and functionally distinct layers which are separated by elastic lamina [7]. Outermost is the adventitia, which is composed primarily of collagen fibers and fibroblasts. Large vessels are supplied with an external vascular system known as the vaso vasorum, and are innervated by acetylcholinergic parasympathetic processes, which are also adventitial constituents [8]. The role of the adventitia is not solely structural. It has long been understood to host a resident population of macrophages, which may play some role in the signaling which leads to intimal hyperplasia [8]. This macrophage population was at one point hypothesized to play a critical role in atherogeneis, following a study which showed that the placement of a cuff over a major artery could trigger early signs of atherosclerosis, likely in part due to the disruption of flow through the vaso vasorum [9]. Recent work has identified a resident population of adventitial stem cells, which are thought to have the potential to differentiate into smooth muscle

or endothelial cells, and potentially themselves play a role in the development of intimal hyperplasia in response to vessel injury [10].

The adventitia borders the media, which is primarily composed of smooth muscle cells (SMCs) and elastic lamina. Larger vessels feature a greater degree of organization of these layers. Interestingly, while classical interpretations of intimal hyperplasia made the reasonable hypothesis that the SMCs invading the intima migrated from the media, recent evidence suggests that the adventitia is the likely source [11]. (A briefly popular idea that hyperplasia was driven primarily by circulating bone marrow derived cells has been largely disproven [12]).

Finally, the innermost, and by far the thinnest layer is the intima. In healthy vasculature, this is composed primarily of the single-cell thick endothelium, which forms the functional interface between flowing blood and the vascular tissue. Endothelial cells reside on an extracellular matrix (ECM) rich in collagens, laminin, and fibronectin, which sits atop another layer of elastic lamina separating it from the media. This is the layer into which SMCs migrate during pathological hyperplasia [13].

1.2.2 The endothelium

The endothelium is the functional interface between the two drastically different environments of the vascular tissue and flowing blood. The endothelial cells (ECs) which make up the endothelium are necessarily polar, and have three faces through which they interact with their local environment and carry out the homeostatic processes enabling blood and tissue to coexist. The basal surface of ECs is characterized by integrin dimers which firmly adhere the cells to their ECM and use their intracellular domains to form focal adhesion complexes where they associate with the cell's actin cytoskeleton. Second, the periphery of ECs is

characterized by junctional proteins which homotypically associate, enabling junction formation with neighboring ECs. Third, the luminal surface of ECs contains a glycoprotein and glycosaminoglycan (GAG)-rich glycocalyx, a collection of surface adhesion molecules enabling leukocyte movement into and between ECs, and membrane-bound elements which regulate coagulation, including endothelial nitric oxide synthase (eNOS) and thrombomodulin. Together these elements enable the endothelium to maintain barrier function, regulate local inflammation, and maintain a delicate balance between hemostasis and the prevention of thrombosis.

1.2.2.1 Endothelial barrier function

The endothelium must maintain strict control over the movement of fluids, cells, ions, and proteins between the vascular and interstitial compartments. This enables the appropriate delivery of blood components to tissues, while preventing local inflammation and edema. Barrier function is largely enabled through the formation of adherens junctions, apical associations between ECs dominated by vascular endothelial cadherin (VE-Cadherin), gap junctions which primarily enable fluid, ion, and small protein exchange between ECs, and tight junctions, basal complexes marked by members of the occludin and caluidn protein families. Gap junctions are composed primarily of members of the connexin family. Both adherins and tight junctions feature direct connections to the endothelial actin cytoskeleton: VE-Cadherin via catenins, α-actinin, and vinculin, and tight junction constituents via tight junction proteins 1-5, cingulin, and spectrin. The distribution of endothelial junctional complexes varies across the vasculature, from the fenestrated endothelium of the renal microvasculature, to the tight junction-dominated blood brain barrier and major arterial vasculature

[14,15]. A fourth component of the EC barrier which is not directly associated with the assemblies in adherens or tight junctions is platelet endothelial cell adhesion molecule 1 (PECAM-1), which, like VE-cadherin, binds adjacent ECs homotypically. Interestingly, disruption of PECAM-1 does not affect barrier function basally, but severely disrupts resistance to inflammatory insults [16]. This is likely due to its function as a mechanotransducers, which will be discussed later.

Another contributor to the barrier function of the endothelium is the luminal glycocalyx. This carbohydrate-rich layer forms an additional boundary between blood and tissue, and remains among the more enigmatic aspects of EC biology. Its backbone is understood to be composed primarily of EC-derived membrane associated proteoglycans and glycoproteins, and its outer reaches are occupied by a mixture of endothelial- and plasma-derived GAGs, glycoproteins, and other molecules. The outer glycocalyx is a dynamic environment, with a constant molecular exchange between it and the circulating plasma [17]. Enzymatic degradation of hyaluronan, a major GAG component of the glycocalyx, results in almost instantaneous myocardial edema, emphasizing the role of this layer in maintaining a fluid balance across the endothelium[1].

An early contributor to the identification of the glycocalyx was modelling of blood flow which suggested the existence of a slow-moving plasma, rather than an entirely solid additional layer, in between the endothelium and bulk blood flow in the microcirculation [18]. The ephemeral nature of the glycocalyx complicates efforts to quantify it. Estimates of its thickness, obtained either through *ex vivo*

[1] This conclusion is suspect because hyaluronan is also a component of the ECM, so this may have been a result of a loss of integrity of the basal lamina [179], however a similar study found that breakdown of heparan sulfate similarly increased endothelial permeability to albumin [180].

microscopy, or live tracking of microparticles in circulation, range from about 500 nm in muscular microcirculation [19], to 4.5 μm in the carotid arteries [20]. The glycocalyx is largely understood to be absent in most *in vitro* cultured endothelial cells [21]. Even *in vivo* in the presence of the flow and circulating plasma components which form a physiologically relevant glycocalyx, a full, hemodynamically effective layer takes several days to regenerate when ablated [22]. In spite of considerable evidence against the existence of a relevant glycocalyx *in vitro*, its absolute absence remains a point of considerable controversy in the field [23].

1.2.2.2 Endothelial immune function

Endothelial cells can modulate their barrier function, and encourage the movement of circulating leukocytes into the subendothelial space in response to inflammatory stimulation. ECs can secrete chemoattractants including MCP-1 capable of recruiting circulating leukocytes to the endothelium [24]. In order to pull a circulating immune cell out of the circulation, endothelial cells use a combination of molecules enabling transient weak connections followed by more robust attachments in order to drive leukocyte rolling followed by firm adhesion and eventually intravasation. The interaction of endothelial E-selectin and P-selectin transiently bind to leukocyte L-selectin and PSGL-1, enabling initial attachment and rolling, followed by stable arrest and junctional migration driven by leukocyte integrins α4β1, αL, and αM β2 to endothelial intercellular adhesion molecule-1 (ICAM-1), ICAM-2, and vascular cell adhesion molecule 1 (VCAM-1), and finally endothelial transmigration, which is effected by the same adhesion molecules as stable arrest, in concert with leukocyte DNAM-1, CD99, SIRP-α, and PECAM-1, with endothelial PECAM-1, CD99, PVR, CD47, and junctional

adhesion molecule-C (JAM-C), and JAM-A [25]. While this process is essential to enable a rapid response to infections, aberrant transendothelial localization of immune cells is a leading driver of early atherosclerosis.

1.2.2.3 Endothelial regulation of hemostasis and thrombosis

Another critical aspect of the endothelium's role as an interface with blood is its capability to regulate coagulation. One of the physical features making ECs readily identifiable via electron microscopy is Weible-Palade bodies, oblong organelles enabling the storage and rapid exocytosis of, among other factors, tubules of von Willebrand Factor (vWF). vWF is a shear-sensitive multimer with the capability to quickly bind both exposed ECM and circulating platelets in order to effect a rapid hemostatic response. ECs do constitutively secrete vWF under basal conditions, however have the capability to rapidly release the contents of stored vWF from Weible-Palade bodies quickly when stimulated [26–28]. Interestingly, as with many of the aspects of vascular biology which have been described here, the expression levels of the gene encoding vWF is highly variable across the vasculature [29].

Toward the prevention of thrombosis, healthy ECs also constitutively express factors which attenuate coagulation. Among the most important of these is nitric oxide (NO), which is produced by endothelial nitric oxide synthase (eNOS). eNOS, like other members of the nitric oxide synthase family, functions by reducing L-arginine with molecular oxygen and NADPH as co-substrates. NO has a number of beneficial roles in the vascular system including vasodilation, inhibition of platelet and leukocyte adhesion, and control of SMC proliferation. Secreted NO acts as a signaling molecule, dilating blood vessels by stimulating soluble guanylyl cyclase and increasing cGMP in SMCs. Increasing the

concentration of NO near the lumen prevents platelet aggregation and therefore thrombosis and, secondarily, hyperplasia by preventing the release of platelet derived growth factors which can trigger SMC proliferation. Similarly, NO can prevent inflammation by downregulating the expression of certain adhesion molecules by leukocytes necessary for endothelial adhesion [30].

Endothelial cells also synthesize and secrete prostacyclin, an arachidonic-acid metabolite signaling molecule which similarly acts as a vasodilator and inhibits platelet aggregation by binding to the platelet prostacyclin receptor and upregulating cAMP production within the platelet [31]. In addition to these platelet-directed mechanisms, the endothelium expresses factors which target specific portions of the plasma clotting cascade or act to potentiate clot fibrinolysis. These processes will be discussed in section 1.2.3.3 following a brief review of the global processes governing hemostasis and thrombosis.

1.2.3 Hemostasis and thrombosis

The ability of blood to form a hemostatic plug in order to rapidly respond to interruptions in the vasculature is critical to mammalian survival. However, inappropriate, uncontrolled, or wholly intravascular blood clotting can prevent blood flow, causing potentially deadly ischemia. The necessary process of maintaining vascular integrity is termed hemostasis, while dangerous intravascular clotting is known as thrombosis. The clotting system consists of several major players, including platelets, soluble clotting factors, and endothelial-derived proteins which regulate clot formation. Maintaining a balance which enables hemostasis while preventing thrombosis is a hallmark of a healthy endothelium. The pharmacological reestablishment of this balance in patients remains a major challenge in modern medicine.

1.2.3.1 Platelets

Platelets are small circulating anuclear cells. While in recent years it has become clear that their roles in normal biology are varied [32,33], this document is primarily interested in their role as thrombocytes. The rheology of the major arteries creates a two-phase flow of blood driving the outer margination of platelets [34]. Platelets detect interruptions in the vascular endothelium by quickly binding to either exposed components of the basement membrane extracellular matrix or vWF. Platelets bind the ECM, including laminin, fibronectin, or most potently collagen with glycoproteins (GP) α2β1 or VI, and they bind vWF [35] which itself binds matrix components or is constitutively present in the subendothelium with GPIbα, which is a critical link in high-shear areas. Platelets subsequently activate and release adenosine and thromboxane A2, which further activate nearby platelets via membrane GPCRs and enable the formation of a multicellular platelet aggregate facilitated primarily by integrin GPIIbβ3 enabling platelet-platelet binding [36]. Following the formation of this initial plug, platelets continue to be involved in an expanding platelet aggregate, and in potentiating portions of the plasma clotting cascade, described below.

1.2.3.2 The plasma clotting cascade

The formation of a fibrin clot by soluble clotting factors is initiated by the distinct but deeply interconnected intrinsic and extrinsic coagulation pathways. Classically, the extrinsic pathway is described as the activation of factor (F)VII into FVIIa by exposure to extravascular tissue factor, while the intrinsic pathway is initiated by the activation of FXII into FXIIa which initiates the waterfall cascade of FXI into FXIa activating FIX into FIXa. These pathways converge on the

common pathway: FX is activated to FXa, which cleaves prothrombin into thrombin, which finally cleaves fibrinogen into fibrin. Thrombin additionally potentiates its own cleavage by enabling the activation of FXI, FVIII (FVIIIa activates FX), and FV (FVa cleaves thrombin directly). The intrinsic pathway was so named because of its role was understood as amplifying the responses of the extrinsic pathway and of platelets. Once tissue factor has initiated a clotting response, the contribution of the intrinsic pathway's feedback mechanisms to FX activation is orders of magnitude greater than that of the extrinsic FVIIa-tissue factor extrinsic tenase complex [37,38].

More recently, the specific role of the contact pathway in thrombosis has come to be understood. Negatively charged substances, including free DNA, bacterial polyphosphates, and artificial biomaterial surfaces trigger the activation of FXII to FXIIa and prekallikrein to α-kallikrein in the presence of high molecular weight kininogen, which is cleaved by FXIIa giving rise to the inflammatory peptide bradykinin, and potentiating the intrinsic pathway described above [39]. Populations and individuals lacking normally functioning FXII, prekallikrein, or high molecular weight kininogen do not exhibit bleeding disorders, suggesting that these components may drive thrombosis over hemostasis, including in response to biomaterials [40].

1.2.3.3 Endothelial regulation of thrombosis

In addition to the platelet-directed regulatory effects of endothelial-derived NO and prostacyclin described in section 1.2.2.3, endothelial cells have the capability to regulate portions of the plasma clotting cascade. Several of these functions are carried out by the large membrane-bound protein thrombomodulin, which binds local thrombin with several antithrombotic effects [41]. First, the

thrombomodulin-thrombin interaction blocks the ability of thrombin to bind fibrinogen. Second, the complex potentiates the generation of activated protein C, which, among other things, inactivates FVIIIa and FVa [42,43].

ECs are also critical players in initiation and regulation of the extrinsic clotting cascade, and can regulate the fibrinolytic processes that break down clots. Under inflammatory conditions, ECs can be stimulated to express tissue factor. In their basal state ECs secrete tissue factor pathway inhibitor (TFPI), which acts by blocking the formation of the extrinsic tenase complex of TF-FVIIa [38]. Fibrinolysis, the digestion of fibrin in a clot, is accomplished by the enzyme plasmin. Endothelial cells potentiate fibrinolysis by secreting tissue plasminogen activator, which generates active plasmin by cleaving its soluble zymogen plasminogen [44]. Interestingly, ECs also secrete factors inhibiting this same pathway, including plasminogen activator inhibitor-1 (PAI-1), although recent work has shown that PAI-1 may have additional antithrombotic roles, specifically binding to and inactivating FXIa, particularly in the setting of sepsis [45].

1.3 Endothelial cells are mechanically sensitive

In the sections above, the critical roles of the endothelium in regulating hemostasis, thrombosis, vascular tone, and immunogenicity were discussed, with some mention of the consequences of endothelial dysfunction. While variability between individuals are important predictors of overall vascular health, there is also predictable variation in EC disease susceptibility within individuals driven by the sensitivity of ECs to their mechanical environments.

The first evidence of the heterogeneity in endothelial susceptibility that exists within an individual's vascular tree came in the discovery that there are consistent anatomical predictors of atherosclerosis. Specifically, atherosclerotic plaques form at sites of curvature or bifurcation in the arterial vasculature [46], with particular atherosclerotic risk seen in the inner curvature of the carotid artery, the outer curvature of the aortic arch, and the torturous processes of the coronary vasculature. There was initial disagreement about the cause of this regional susceptibility, with some groups arguing that local platelet accumulation drove early plaque formation, and others suggesting that plaques formed near regions of peak cyclic strain. Ultimately the causative culprit was identified as flow disturbances, manifesting as either low flow, impinged flow, or flow oscillating with the cardiac cycle [47].

1.3.1 EC morphology responds to flow

With the identification of a relationship between local hydrodynamics and atherosclerotic risk came the discovery of morphological changes at the level of the endothelial cell, specifically that ECs elongate in response to unidirectional fluid shear stress and align parallel to the direction of flow [48]. This was initially identified in histological analyses of major vessel segments which are understood to be exposed to non-reversing fluid shear stress [49]. Later *in vitro* confirmation showed that the exposure of a cultured confluent monolayer of endothelial cells to non-reversing shear drove alignment in a matter of hours [50], and that exposure to "chaotic" reversing shear caused ECs to maintain a rounded cobblestone morphology [51]. Around this period, specific quantitative metrics of EC morphology were developed around the study of ECs which had been experimentally exposed to non-reversing shear using a cone-plate apparatus:

angle deviance to measure alignment or orientation, and shape index and aspect ratio to describe shape or elongation [52].

In addition to the dramatic effects of flow seen on endothelial cells on the whole-cell level, substantial changes were seen in the actin cytoskeleton as well. Specifically, ECs cultured statically were seen to exhibit a peripheral band of filamentous (F)-actin along with random disorganized staining within the cytoplasm, whereas flow-aligned cells exhibited cytoplasmic actin stress fibers which aligned with the long axis of the cells and the direction of the flow to which they were exposed [53].

1.3.2 EC gene expression and function respond to flow

As the field of vascular biology has matured with the development of transcriptomics, efforts were made to identify specific genes showing responsiveness to flow. A large microarray study of human umbilical vein ECs (HUVECs) cultured either statically or under unidirectional laminar flow for 24 hours identified a number of flow responsive genes, but few whose expression was as profoundly affected by flow as Krüppel-like factor 2 (KLF-2) [54]. KLF-2, and the other Krüppel-like factors are transcriptional regulatory proteins named for their functional and structural similarity to Krüppel[2], first identified in *Drosophila* and so named because its deletion was found to eliminate the thoracic and anterior abdominal segments in embryos [55]. The relationship between KLF-2, flow, and anatomy was confirmed in an *in situ* hybridization study showing that KLF-2 is expressed in far lower levels at sites of curvature

[2] Krüppel is the German word for cripple

and bifurcation than in straight arteries. It was further demonstrated, by cuffing the murine carotid artery and thereby increasing local fluid shear stress, that increasing prolonged shear drives increased local KLF-2 expression [56].

While the mechanism of flow-induced KLF-2 expression is not fully understood, one thing that is clear is that flow has the dual effect of (1) potentiating KLF-2 expression, and (2) stabilizing KLF-2 mRNA. It is known that HMG-CoA reductase inhibitors (statins) also increase KLF-2 expression. However work comparing the effect of flow preconditioning with lovastatin treatment of HUVECs, paired with Actinomycin treatment to block transcription showed that, while both stimuli triggered KLF-2 transcription, only flow-derived KLF2 remained present following transcriptional blockade [57].

Numerous studies have linked KLF-2 with other genes identified as flow-responsive. In a wide-ranging study of many genes thought to respond to flow, siRNA knockdown of KLF-2, affected 15% of previously identified endothelial flow responsive elements, demonstrating their reliance on KLF-2 [58]. More targeted mechanistic work demonstrated that KLF-2 directly potentiates the production of eNOS by both specifically binding its promotor and by actively recruiting its co-activator. The same study also demonstrated the direct effect of KLF-2 on the downregulation of the inflammatory adhesion molecules VCAM-1 and E-selectin, consequently reducing T-cell rolling on and attachment to ECs [59]. Further attenuating effects of KLF-2 on inflammatory processes have been identified, including the ability of KLF-2 to downregulate transforming growth factor β (TGF-β) by direct inhibition of its cofactor, AP-1 [60].

While this document and the experiments described herein will focus primarily on KLF-2, it should be noted that other transcription factors, notably including NF-κB (nuclear factor κ-light-chain-enhancer of activated B cells) have

also been shown to be flow responsive. While KLF-2 is upregulated in response to the kinds of high, unidirectional fluid shear stress associated with straight non-branching portions of the arterial tree, the flow patterns stimulating NF-κB are the subject of some debate. NF-κB is certainly upregulated in settings of low or oscillating flow, however it has also been shown to exhibit a brief surge in expression in response to the onset of unidirectional flow [61]. One hypothesis, supported by recent and compelling data, is that NF-κB expression is stochastic across an EC population and likely a response to a mismatch between EC orientation and flow [62]. NF-κB is responsible for upregulating several pro-inflammatory elements, which supports the wider view that unidirectional flow and responses to it are athero- and immune-protective, while the inverse is true for stagnant, oscillatory, or low flow. Interestingly, a direct link has been identified between KLF-2 and NF-κB, with flow-induced KLF-2 directly inhibiting the function of NF-κB by preventing cofactor recruitment [59].

1.3.3 Mechanisms of EC mechanosensitivity

As described above, it is known that a constellation of changes to the gross morphology, cytoskeletal morphology, gene expression profile, and overall function of endothelial cells is effected by the mechanical stimulus of fluid shear stress. The mechanisms linking these changes to each other and to the mechanical stimulation apparently driving them remains unclear. The necessary polarity of ECs gives them three distinct faces: the apical (luminal) face interacting with blood flow, the junctional face interacting with neighboring ECs, and the basal face interacting with the extracellular matrix. Hypotheses exist identifying putative mechanosensors in each face, however to date none has been identified as the singular initiator of the EC flow response.

Given the direct contact between the EC luminal face and flowing blood it is reasonable to hypothesize that this part of the EC contains the elusive mechanosensor. Primary cilia exist as 3-5 μm-long microtubular protrusions in the endothelial cells of embryonic zebrafish, and are necessary for their early development [63], however their existence in the mammalian endothelium was initially controversial. Recent evidence has identified cilia in both the adult mouse aorta, and in HUVECs cultured *in vitro* [64,65]. Interestingly, in these mammalian systems cilia were shown to exist only in regions of low or disturbed flow [65], and the loss of cilia was seen as an early response to unidirectional shear stress [64], together suggesting that the presence of cilia is a response to atherogenic shear and likely cilia were not themselves acting as primary mechanosensors.

Also at the apical cell surface, and the subject of much greater controversy is the glycocalyx. Selective deletion of individual syndecans – the family of transmembrane proteoglycans linking the EC to the diffuse extracellular components of the glycocalyx – results in substantial loss of EC alignment in response to unidirectional flow [66]. While there is a persistent argument among some in the community for the glycocalyx as a critical mechanosensor [67], there are two pieces of evidence which suggest that this is unlikely. The first is that *in vivo* the glycocalyx substantially dampens the amount of fluid shear stress translated to the cell [68], suggesting that while the selective deletion of the syndecans may prevent the translation of shear stress to the EC cytoskeleton, the remaining structure may sufficiently disrupt the mechanical stimulus to simply prevent mechanotransduction to the actual mechanosensitive elements in the cell. The other is that ECs cultured *in vitro* in the short term lack a glycocalyx, yet are mechanosensitive [21].

Other apically-based hypotheses exist, including cavolae and ion channels [69], however any hypothesis based on direct mechanosensation by the endothelium's luminal surface fails to explain the efficacy of static micropatterning, which will be discussed in section 1.4. At the junctional face, there is evidence that PECAM-1, VE-cadherin, and vascular endothelial growth factor receptor-2 (VEGFR2) function together as a mechanosensory complex, with the greatest specific body of evidence indicating the necessity of PECAM-1 for effecting flow-driven changes in endothelial function [69]. siRNA knockdown of PECAM-1 in HUVECs eliminated upregulation of eNOS in response to unidirectional fluid shear stress [70]. Similarly, murine ECs demonstrated that VE-Cadherin activity was necessary for the establishment of flow-driven polarity by activation of the Rac1 guanosine triphosphatase (GTPase) [71], while another paper from the same group revealed that PECAM-1 knockout mice show neither a Rac1 response in regions of beneficial unidirectional flow nor an NF-κB response in regions of disturbed flow, suggesting the necessity of this junctional complex to all endothelial mechanotransduction [72]. Importantly, all of the studies reviewed here further demonstrated that the activity of activated PECAM-1 was dependent on the flow-driven phosphorylation of specific intracellular tyrosines, suggesting that, while PECAM-1 does mechanosense, it is not the initial responder to fluid shear stress.

Finally, there is evidence implicating elements at the basal surface of the endothelial cell: the integrins and their associated focal adhesion kinases. While integrins are themselves mechanosensitive [73], the shear forces which are felt by the basal attachment points of the EC are orders of magnitude below those at the luminal surface [74], suggesting that integrins are intermediaries and not initiators of flow-induced signaling cascades. Following PECAM-1 activation,

there is a PI3 kinase-mediated global activation of EC integrins, further suggesting that these components are downstream of junctional mechanotransduction [75]. Integrins do act as critical mediators of downstream effects of fluid shear stress both on cytoskeletal reorganization and on the potentiation of NF-κB signaling, with specific studies identifying the role of new integrin-ECM connections on the Cdc42-mediated translocation of the microtubule organizing center as part of the EC polarizing response to fluid shear stress [76], and on the transient inactivation of Rho signaling which enables reorganization of the actin cytoskeleton [77].

In summary, there are a multitude of potentially mechanosensitive elements within the EC, however there has yet to be a concrete identification of any one of these as the initial or lynchpin mechanosensor. Critically, a common thread in these explanations of endothelial mechanotransduction is involvement of the cytoskeleton, both as a potential conduit for physical strain, and through the Rho family GTPases which enable downstream signaling and changes in EC morphology. In the face of evidence about so many varied mechanisms which all have a demonstrated impact on the fate of endothelial cells, current interpretations of the state of the science posit that mechanotransduction is an aggregation of multiple mechanical inputs, rather than a single governing pathway [69], which may explain the differential or partial responses seen by ECs to certain stimuli including static micropatterning.

1.4 Micropatterning

Endothelial micropatterning refers to a variety of techniques which use the organization of basal cues to flow-independently modulate the morphology,

gene expression, and function of ECs. Micropatterning is generally carried out by either restricting EC growth to specific portions of a substrate by modifying surface chemistry, or by altering EC adhesion dynamics by modifying surface topography, thus forcing the organization of focal adhesions. All of these techniques have proven to be useful tools for understanding the basic biology of EC mechanotransduction, and some may be translatable to novel endothelializable vascular devices.

Spatial growth restriction micropatterning is carried out by biochemically modifying specific regions of a culture substrate to facilitate or prevent EC adhesion, generally by modulating hydrophobicity. The definition of culture areas can be accomplished using a variety of techniques, including microcontact printing, microfluidics, or direct inkjet printing of biomolecules onto a culture surface [78]. Early studies of biochemical growth restriction explored the ability of adhesive islands and lanes of varying sizes to affect bovine EC tendencies toward apoptosis, growth, or angiogenesis. This work showed that EC apoptotic rate was inversely proportional to the area of adhesive islands, supporting the idea that engagement of EC junctional complexes provides a pro-survival stimulus [79].

A more recent series of studies characterizing the responses of non-human primate carotid ECs to spatial growth restriction in the form of alternating lanes of collagen-I and albumin gave substantial support to the idea that micropatterning could serve as an analogue of fluid shear stress. The first of these studies looked at the morphology of micropatterned ECs and found that they aligned and elongated to an extent similar to those seen under unidirectional fluid shear stress *in vivo*. This same study demonstrated substantial alignment of both the actin and tubulin components of the EC cytoskeleton, although

interestingly noted a strengthening of the dense peripheral actin band, the dissolution of which is seen as an early response to fluid shear stress *in vivo* [80]. A second paper from the same researchers made the important discovery that micropatterned ECs showed immunoprotective changes in gene expression and overall function when micropatterned. Specifically, they found increases in KLF-2 gene expression, decreases in VCAM-1 gene expression, and reductions in the strength of the connection between ECs and monocytes, suggesting reduced adhesion molecule function. Importantly, they did note that the KLF-2 and VCAM-1 gene expression changes were weaker than those seen under unidirectional fluid shear stress, lending support to the idea that static micropatterning only engages a portion of the multitude of mechanosensors that the EC possesses [81].

While spatial growth restriction micropatterning has the advantages of relative methodological ease and a self-explanatory mechanism, and has facilitated important contributions to basic science, it has important drawbacks which preclude its translatability to endothelializable medical devices. Spatial growth restriction requires the placement of non-cellularized buffer regions in between patterned lanes in order to be effective. In a device, this has the obvious drawback of leaving a substantial portion of the device surface exposed to blood. Additionally, narrow endothelialized lanes do not allow for complete engagement of the EC junctional complex. In contrast, topographic micropatterning generally uses a biochemically consistent, but geometrically modified surface. The studies described here used anisotropic ridge-and-groove features with varying feature sizes and using varying base materials. For clarity and consistency, pattern spacing will be described using pitch, which is defined as the combined spacing

of one ridge and one groove (eg: distance from peak to peak) regardless of the terminology used in the primary publications.

Topographical micropatterning has been demonstrated to significantly align ECs in a pitch-dependent manner across a variety of studies. Human aortic ECs grown on polyurethane substrates with pattern pitches ranging from 400 nm to 4 µm exhibited significant reductions in average angle deviance on all patterns with pitches 800 nm or wider relative to planar substrates, suggesting increasing benefit with increasing pitch. The same study similarly showed increasing EC elongation with increasing pitch, however on 4 µm pitch showed a modest aspect ratio of only about 3, relative to aspect ratios of 3.7 for their fluid shear stress-exposed controls [82]. Very similar morphological results were found by a group studying a vastly different material. Toward the development of an endothelializable stent, a study of HUVECs on micropatterned cobalt-chromium found that ECs substantially aligned, but showed aspect ratios of about 2.8 on materials with depths of at least 600 nm and pitches ranging from 3 - 32 µm [83].

Studies of topographically micropatterned ECs find that anisotropic topography generally increases EC adhesion and directed migration on test surfaces, indicating that topography will aid in endothelializability [82–84]. Studies of the effects of topography on EC function are limited however. One study examining the effect of topography on human coronary ECs cultured on collagen-coated PDMS with 4 µm pitch and 2 µm depth found contradictory effects. Culture on gratings did significantly decrease the gene expressions of VCAM-1 and ICAM-1, however it also increased monocyte adhesion and decreased eNOS expression relative to ECs cultured on planar PDMS [85].A similar study examining the behavior of EA926 human ECs on silicon and titanium surfaces with pitches ranging from 1-100 µm and depths of 1.3 µm found

that VCAM-1 expression decreased with increasing pitch [86]. To date, the effect of anisotropic topography on directly flow-responsive genes including KLF-2 and NF-κB have not been studied.

1.5 Endothelial progenitor cells and ECFCs

Just over twenty years ago, the existence of circulating cells with the potential to differentiate into cells resembling mature ECs was discovered. Since that time there has been significant interest in these cells as a readily accessible autologous source for both cell therapy and tissue engineering. However, there has also been significant controversy over the origins, identity, and nomenclature of both the circulating progenitor cells and their cultured outgrowth products.

1.5.1 Endothelial progenitor cells contain multitudes

The existence of endothelial progenitor cells (EPCs) was first demonstrated in 1997 in the form of CD34+ VEGFR2+ constituents of the blood mononuclear cell fraction. These cells, when cultured in pro-endothelial growth media demonstrated a phenotype similar to mature ECs, and the potential to accelerate re-endothelialization in a rodent ischemia model [87]. The discovery of EPCs triggered obvious excitement among those interested in their potential as tools for cell therapy, tissue engineering, and explanations of *in vivo* vascular repair. However with further characterization, it became clear that the culture of blood mononuclear cells in endothelial growth medium gave rise to two populations of cells with distinctly different phenotypes, and potentially different origins. The first of these, originally termed early EPCs, and now known as

myeloid angiogenic cells (MACs), clearly originate from marrow, and do not have the capability to differentiate into ECs. MACs remain true to their hematopoietic lineage, although do provide paracrine support of angiogenesis. Late EPCs, now known as endothelial colony forming cells (ECFCs) by contrast have an uncertain origin and can differentiate into ECs [88,89].

The confusion over the origins of both of these cell types and their relation to each other has resulted in a literature containing often contradictory terminology for both. A recent consensus statement seeking to standardize nomenclature defines MACs as blood-derived cells which are CD45+, CD14+, CD31+, CD146-, CD34-, while ECFCs are blood-derived cells which are also CD31+ but CD105+, CD146+, CD45-, and CD14-. Phenotypically, MACs are defined as being capable of providing paracrine support to endothelial network formation, but not being capable of structural contributions to an endothelium, while ECFCs are defined as having the capability to become the structural elements of a blood vessel [89]. Much of the foundational literature about ECFCs and their potential for tissue engineering applications has referred to them as some variant of blood (B) outgrowth (O) endothelial (E) cells (C) (including EOC, OEC, BOEC, and others). In accordance with the updated standards, these cells will be referred to here as ECFCs, regardless of the terminology used in the cited studies. The updated nomenclature standards also recommend against the use of EPC, given that MACs are not technically endothelial progenitors.

The origins of ECFCs remain unclear. For many years it was understood that ECFCs, like MACs, were marrow-derived. This notion is largely the product of a 2000 paper studying the blood outgrowth products of patients who had received sex-mismatched bone marrow transplants. It showed that early outgrowth cells shared the recipient’s genotype, while late outgrowth products

shared the donor genotype [90]. While this result is compelling, it has yet to be recapitulated in healthy patients, with several attempts to culture EC-like cells directly from the marrow being unsuccessful [91]. The current understanding is that ECFCs likely arise from resident subendothelial progenitor populations, with transcriptomic analyses demonstrating that ECFCs share more similarities with ECs from the microvasculature than from any other vascular bed [92]. A persistent criticism of the ECFC literature which has yet to be fully disproven is the notion that ECFCs are sloughed-off mature endothelial cells. Early work used the expression of CD133 as a progenitor marker differentiating pre-ECFCs from mature ECs [93], however later work showed an exclusively hematopoietic fate for CD34+ CD133+ VEGFR2+ cells [94]. As researchers continue to search for a definitive marker which uniquely identifies ECFCs, their origin remains an enigma.

1.5.2 ECFCs in cell therapy and disease research

Regardless of their origin, ECFCs offer numerous potential mechanisms to further vascular biology and cardiovascular medicine. One of the core promises of ECFCs as a clinical tool is their use for personalized medicine. Several groups have studied patient ECFCs in order to gain a deeper understanding of the endothelial pathologies seen in diseases as varied as von Willebrand disease [95] to gestational diabetes [96]. While the persistently enigmatic nature of ECFC origin does hamper scientists' ability to draw mechanistic conclusions based on ECFC data alone, it does open the door for correlative studies on a minimally-invasively obtained source of ECs from varied patient populations [97].

The use of ECFCs and MACs for cell therapy has also been investigated dating back to the initial putative identification of circulating EPCs [87]. Numerous studies have demonstrated the ability of human cord blood-derived ECFCs to incorporate and accelerate the healing of ischemic murine hind limb [98,99] and rat cerebral ischemia [100]. An ongoing randomized clinical trial is testing the efficacy of patient autologous MACs for accelerating coronary healing following acute myocardial infarction, with results expected in December, 2019 [101].

1.5.3 ECFCs for tissue engineering

As discussed in section 1.1, the design of a durable small diameter vascular graft remains an unmet challenge. Among the potential solutions is *in vitro* endothelialization with patient autologous endothelial cells. This technique is limited by the invasiveness necessary to obtain patient vasculature from which to isolate ECs. ECFCs present a potential solution to this problem in the form of an EC source which is accessible via venipuncture. Substantial work has gone into evaluating the similarities between the form and function of ECFCs with attention toward their suitability for use in vascular grafts. In a 2014 review paper, Glynn and Hinds outline the three EC-like qualities of an ECFC which would be necessary to demonstrate suitability in a vascular graft: thromboprotection, prevention of intimal hyperplasia, and responsiveness to fluid shear stress [102].

Much of the work establishing ECFCs as a potential tool for vascular tissue engineering has taken advantage of a unique resource: case-matched mature carotid artery ECs and blood-derived ECFCs from *Papio anubis* baboons. In addition to case-matching in a relevant preclinical model, these studies have the added benefit of comparing to the kinds of major artery ECs whose function device-seeded ECFCs should approximate, rather than the often functionally

inequivalent HUVECs used in many studies. A detailed comparison of these cell types at baseline and when stimulated with the inflammatory cytokine tumor necrosis factor α (TNF) found that, in gene expression and surface antigen expression, carotid ECs and ECFCs behaved similarly. No substantial differences were seen in the baseline expressions of any of the pro-inflammatory adhesion molecules tested (E-selectin, ICAM-1, VCAM-1), although ECFCs did show an increase in TNF-stimulated ICAM-1 expression. No differences were seen in the expressions of the genes encoding thrombomodulin, tissue factor, or TFPI. Functionally, the results demonstrated that ECFCs have no difference in protein C activation, and a lower tendency toward FX activation than ECs when TNF-stimulated. Both cell types performed equivalently in an *ex vivo* arteriovenous shunt model of platelet deposition by whole, non-anticoagulated flowing blood [103]. These results overwhelmingly support the idea that ECFCs match EC function pertaining to immunogenicity (a driver of hyperplasia and thrombosis) and thromboprotection.

Multiple *in vitro* studies have examined the flow-responsiveness of ECFCs using the same *Papio anubis* model. A comparison of the same case-matched cells described above when cultured statically versus a under a physiologically relevant level of unidirectional fluid shear stress in parallel plate flow chambers found ECFC morphological changes mirroring those seen in carotid ECs. Both cell types exhibited dramatic reductions in both shape index and average angle deviance from the direction of flow. They also showed similar changes in the expressions of key genes, including upregulations of eNOS and thrombomodulin [104]. A similar study using a cone-and-plate shear apparatus to characterize the responses of ECFCs to steady unidirectional shear, oscillatory shear, and a multiple pulsatile shear regimes showed similar trends, although

often without the same levels of statistical significance. Overall, this second study confirmed definitively that ECFCs elongate in response to unidirectional steady or unidirectional pulsatile shear, but maintained a cobblestone morphology when cultured statically or under fully oscillatory shear. It further demonstrated a significant downregulation in the gene expression of eNOS and P-selectin in response to oscillatory compared to steady shear. Additionally, it showed trends toward increased ICAM-1 and E-selectin expression with exposure to oscillatory shear, which was recapitulated by a monocyte adhesion assay demonstrating that steady shear-exposed ECFCs retained many fewer monocytes than oscillatory-shear exposed ECFCs [105]. Taken together, these results demonstrate that ECFCs largely match ECs in their flow sensitivity.

A final study which combined the assessments of thromboprotection, hyperplasia-prevention, and shear sensitivity compared the performances of autologous ECFC-seeded vascular grafts preconditioned with oscillatory flow, steady flow, or no flow in an *ex vivo* assay of platelet accumulation and an *in vivo* aorto-iliac implant model with 28-day survival. In the *ex vivo* shunt, this study identified significantly greater platelet accumulation on ECFC-seeded grafts with oscillatory preconditioning than either static or steady flow preconditioning (which were nearly identical), and visible reductions in intimal hyperplasia in steady-flow pre-exposed grafts than static grafts. While this study did not directly compare graft performances to unmodified clinical standard ePTFE devices, the results they observed were significant improvements over previously published values [106].

While ECFC mechanical sensitivity and potential for use in tissue engineered vascular grafts have been well established by the work described above, it was not known prior to the start of this dissertation whether ECFCs

could be modified by static micropatterning as has been described for mature ECs. Only a single published study had described any attempt to statically micropattern ECFCs. In it, the authors compare the responses of the same carotid ECs and blood-derived ECFCs from *Papio anubis* described above, on spatial growth restriction micropatterns using alternating lanes of collagen-I to promote cell adhesion, and bovine serum albumin to block it. They found that within 24 hours ECFCs were crossing lane boundaries at a significantly higher rate than mature ECs, and that by 48 hours the pre-defined lanes were nearly unidentifiable. The use of fluorescently-labeled collagen for cell seeding revealed that the ECFCs were able to remodel their ECM in order to facilitate lane-crossing, suggesting that their increased matrix remodeling ability would prevent the efficacy of static micropatterning [107].

1.6 Assessing material thrombogenicity

Given the well-established understanding that one of the primary mechanisms by which blood-contacting devices fail is thrombosis, reliable assessments of material thrombogenicity are critical to predicting device performance *in vivo*. While *in vitro* endothelialization would offer protection from biomaterial-induced thrombosis if device coverage were complete, the necessarily exposed surfaces of devices designed to be *in situ* endothelializable or endothelial-mimetic must demonstrate an ability to resist rapid thrombosis driven by activation of the contact pathway. While assays of single-factor activation or static platelet adhesion on novel devices are informative, platforms exposing biomaterials to whole, flowing, non-anticoagulated blood will be most predictive of *in vivo* performance.

1.6.1 The non-human primate arteriovenous shunt

The nonhuman primate *ex vivo* shunt model in its current form is a platform allowing for the thrombogenicity testing of biomaterial devices in whole non-anticoagulated blood which is flowing at physiological arterial rates. The *ex vivo* shunt itself is extendable silastic tubing shunting blood flow from the femoral artery to the femoral vein of male juvenile *Papio anubis* baboons. This chronically implantable device allows for multiple non-terminal experiments to take place in each animal. A fraction of the animal's platelets are labeled with ^{111}In and experiments are run over a gamma camera, allowing real-time quantification of radioactive platelet deposition with 60-second resolution. Additionally, the animal receives an injection of ^{125}I-labeled homologous fibrinogen, which enables an aggregate measure of fibrin deposition following experiments. Blood flow is supplied by the animal, measured using an ultrasonic flow probe, and regulated using a manual clamp [108]. This "animal as pump" model allows for experiments to be carried out without any anticoagulation whatsoever.

This model was first reported on in a 1979 study in which baboon platelets were radiolabeled, and platelet and fibrinogen consumption and deposition on cannulae of varying thrombogenicities were measured [109]. In the time since, this model has contributed substantially to the current understanding of thrombosis management and biomaterial development. These critical discoveries include the establishment of acetylsalicylic acid (ASA, trade name aspirin) and clopidogrel (trade name Plavix) dual antiplatelet therapy (DAPT) [110], the demonstration of activated protein C as an antithrombotic [42], and the potential of flow-conditioned ECFC-seeded grafts [106]. While other groups have developed similar *ex vivo* shunt models for device testing in other animal models

[111], this model is unique for its combination of human-like coagulation biology, and ability to assess platelet deposition in real time rather than extrapolated from consumption.

1.7 Dissertation aims

This dissertation primarily aims to more fully understand the effects of micropatterning on the morphology and gene expression of ECs and ECFCs, toward its development as a tissue engineering tool. The secondary aim of this dissertation is optimizing the use of an *ex vivo* arteriovenous shunt model of device-initiated thrombosis, toward enhanced preclinical device testing.

Aim 1: Characterize the effect of spatial growth restriction micropatterning on ECFCs. By using an updated methodology, Aim 1 addresses the hypothesis that ECFCs, like ECs, can be flow-independently morphologically manipulated using spatial growth restriction micropatterning, and that micropattern-aligned and elongated ECFCs will show immunoprotective changes in gene expression as was previously seen in ECs. This is the first published demonstration that ECFC morphology can be flow-independently modified by micropatterning. Work pertaining to Aim 1 is presented in Chapter III, and published in *PLoS ONE.*[3]

Aim 2: Characterize the effect of topographical micropatterning on ECs and ECFCs across multiple pitches. Using custom-manufactured polyurethane substrates, this aim tests the hypothesis that culturing ECFCs on

[3] Hagen MW, Hinds MT. Static spatial growth restriction micropatterning of endothelial colony forming cells influences their morphology and gene expression. *PLoS ONE*. 2019; 14 (6): e0218197.

anisotropic topographies will drive alignment and elongation as has previously been demonstrated in ECs. This aim uses high-resolution confocal microscopy and novel image analysis techniques to provide a cell-by-cell quantification of EC and ECFC morphological metrics. These include whole-cell alignment, whole-cell elongation, and subcellular alignment of actin and tubulin fibers. Additionally, this study measures the gene expression of topographically micropatterned cells to test the hypothesis that those cells will exhibit immunoprotective changes in gene expression in response to topographic micropatterning. Work pertaining to Aim 2 is presented in Chapter IV.

Aim 3: Quantify the antithrombotic effectiveness of phosphorylcholine on a prototype cerebral flow diverter using an *ex vivo* arteriovenous shunt model of thrombosis. Using a well-established flowing whole-blood model of device thrombosis, this aim addresses the hypothesis that a phosphorylcholine surface modification will reduce platelet deposition on cerebral flow diverters in whole blood flowing at an arterial rate. Work pertaining to Aim 3 is presented in Chapter V, and published in the *Journal of Neurointerventional Surgery.*[4]

Aim 4: Use linear mixed effects modeling and a retrospective review of archive control data to optimize the analysis of *ex vivo* arteriovenous shunt data. This aim tests the hypothesis that linear mixed effects modeling with fractional polynomial interacting coefficients can improve the fit and meaningful interpretation of *ex vivo* shunt data. Additionally, a pilot hypothesis-generating retrospective analysis of archived control data is presented, which suggests a

[4] Hagen MW, Girdhar G, Wainwright J, Hinds MT. Thrombogenicity of flow diverters in an ex vivo shunt model: effect of phosphorylcholine surface modification. *Journal of neurointerventional surgery.* 2017; 9:1006-1011.

link between individual average aPTT and thrombus stability. Work pertaining to Aim 4 is presented in Chapter VI. Additionally, analyses described in the first portions of Chapter VI are included in publications in *Frontiers in Bioengineering and Biotechnology*[5] and *Acta Biomaterialia.*[6]

[5] Pohan G, Chevallier P, Anderson DEJ, Tse JW, Yao Y, Hagen MW, Mantovani D, Hinds MT, Yim EKF. Luminal plasma treatment for small diameter polyvinyl alcohol tubular scaffolds. *Frontiers in Bioengineering and Biotechnology* 2019; 7:117.

[6] Anderson DEJ, Truong KP, Hagen MW, Yim EKF, Hinds MT. Biomimetic modification of poly(vinyl alcohol): encouraging endothelialization and preventing thrombosis with antiplatelet monotherapy. *Acta Biomaterialia* 2019; 86: 291-299.

Chapter II: Common materials and methods

2.1 Ethics statement

All non-human primate work reported in this dissertation was approved by the Oregon National primate Research Center Institutional Animal Care and use Committee. Approved protocol numbers are provided in chapter methods sections. Male baboons (*papio Anubis)* were cared for and housed by the Oregon National Primate Research Center staff according to the National Institutes of Health “Guide to the Care and Use of laboratory Animals” by the Committee on Care & use of Laboratory Animal Resources, National Research Council (NIH Publications No. 8023, revised 1978). Detailed descriptions of the housing, care, and humane euthanasia of these primates has been published previously [106].

2.2 Primary cell isolation and culture

The procedures described below for the isolation of primary carotid endothelial cells (CaECs) and ECFCs were based on previously established protocols [103,108].

2.2.1 Carotid endothelial cell isolation

Primary CaECs were isolated from animals from which ECFCs were previously collected. Whole carotid arteries were rapidly excised from male juvenile *Papio anubis* baboons at the time of necropsy, and flushed with and stored in ice-cold Dulbecco’s phosphate buffered saline (PBS, 0.1M, Gibco) containing 2-4% penicillin-streptomycin

(PS, Gibco) for 1-4 hours. To release ECs from the vessel wall, arteries were clamped shut at bottom, and filled with a 37ºC solution of 600U/mL collagenase type II (Worthington Biochemical) dissolved in endothelial basal medium (EBM, Lonza) and incubated for five minutes. EC-containing collagenase solution was dripped directly into tissue culture wells which were precoated with 50 µg/mL collagen-I from rat tail (Corning) and filled with EGM-2 supplemented with 18% fetal bovine serum (FBS, Hyclone). Cultures were fed every other day with EGM-2 + 18% FBS for up to four weeks until EC colonies occupying at least half of the well were seen. These colonies were passaged using TrypLE, sorted using anti-CD31 magnetic dynabeads (Invitrogen), and expanded in T-150 flasks (Corning).

2.2.2 ECFC isolation

ECFCs were isolated from the blood of male juvenile *Papio aunbis* baboons. 50 mL of venous blood was drawn into a 7% acid citrate dextrose (ACD) solution. After no more than 45 minutes, blood was mixed 1:1 with Hank's Buffered Saline Solution (HBSS, Corning) and carefully layered on top of Histopaque-1077 (Sigma). The tubes were then centrifuged (800 G, 30 minutes, without braking) to separate the buffy coat containing mononuclear cells. This mononuclear cell suspension was isolated, washed and plated on tissue culture plastic pre-coated with 50µg/mL fibronectin (Sigma). Cultures were fed daily for the first seven days of culture, and every other day for up to four additional weeks with commercially available, growth factor supplemented endothelial growth medium supplemented with 18% FBS. When colonies of cobblestone-shaped cells appeared, they were isolated by manually scraping the non-colony-occupied portions of wells and passaging with TrypLE (Gibco). These cells were expanded in T-25 flasks as described below, and upon reaching confluence, were

passaged, sorted using anti-CD31 magnetic dynabeads (Invitrogen), and further expanded in T-150 flasks using the standard culture conditions described below.

2.2.3 Culture conditions

Between isolation and experiment, all cells were maintained in cryogenic storage. After thawing, cultured cells were maintained in commercially available endothelial growth medium supplemented with 8% FBS for a total of 10%. Unless otherwise specified, all cell expansions occurred in tissue culture flasks (Corning) pre-coated with collagen-I from rat tail (BD Biosciences). All cell culture experiments used endothelial growth media supplemented with 8% FBS for a total of 10 % FBS unless otherwise specified. During expansions and experiments, cells were kept in a sterile, humidified incubator at 37ºC and 5% CO_2. All cell passages were performed using TrypLE (Gibco).

2.3 Micropattern fabrication

2.3.1 Spatial growth restriction micropatterns

The protocol described below is a modification of a previously established protocol [112].

2.3.1.1 Submaster fabrication

Previously manufactured silicon wafers with 25 µm-wide ridges separated by 25 µm-wide grooves were used as masters [107]. Polydimethyl siloxane (PDMS) submasters were manufactured by mixing a 7:1 vol:vol ratio of 184-elastomer base with curing agent (Sylgard, Dow Corning) and briefly degassing before pouring over masters and further degassing for at least 30 min until bubbles were no longer visible.

Submasters were incubated at 80°C for two hours and left to further cure overnight before demolding. After demolding, patterned regions were cut into 2x1 cm stamps.

2.3.1.2 Culture substrate fabrication

All steps were performed at room temperature inside a sterile biosafety cabinet. PDMS submaster stamps were sterilized by dipping in a solution of 70 % ethanol in water, dried for at least 30 min, and exposed pattern-side-up to germicidal ultraviolet (UV) light (Nuaire) for at least 5 min. Clean dry submaster stamps were placed face-down onto non-tissue culture plasma treated polystyrene petri dishes. 50 µg/mL collagen-I from rat tail dissolved in 2N acetic acid was pulled through stamp channels using an aspirating pipet. The collagen was allowed to adsorb to the polystyrene for at least one hour before excess collagen was aspirated, micro-channels rinsed with PBS, and PDMS stamps removed. Substrates were further rinsed with PBS and then blocked with 0.2% Pluronic F108NF Prill Poloxamer 338 (BASF) in water for at least one hour. The substrates were rinsed and stored in PBS at room temperature for no more than one month before use. Control, non-patterned substrates were prepared using a 60 µL drop of collagen-I in place of PDMS stamps.

2.3.2 Topographic micropatterns

2.3.2.1 Master fabrication

Silicon masters with ridge-and-groove patterns were created with pitches of 3, 4, 6, 10, and 14µm using photolithography (pitch = distance from ridge peak to ridge peak). Silicon wafers (76 mm, Electron Microscopy Sciences) were cleaned, spin-coated with S1818 photoresist primer (Microposit), and S1818 photoresist (Microposit), and baked for 60 sec at 115°C. Patterns were cast using either direct write lithography with a

DWL66 direct write system (for pitches 3, 4, 6 µm; Heidelberg Instruments), or a mask aligner (for pitches 6, 10, 14 µm; KARL SUSS) with a custom-written photomask. Wafers were developed with MF-321 developer (Microposit) and fluorinated before use.

2.3.2.2 Submaster fabrication

PDMS submasters for topographical micropatterning were fabricated as described in section 2.3.1.1.

2.3.2.3 Culture substrate fabrication and cleaning

Polyurethane NOA81 (Norland Optical Products Inc.) was dispensed onto face-up PDMS submasters and degassed for 1-3 hours after which 18mm square coverslips (Fisher Scientific) were placed atop the submasters and further degassed for at least 16 hours. Culture substrates were cured by exposure to 2J of long-wave UV light in a UV crosslinker (Fisher Scientific). The cured substrates were moved from the crosslinker directly into a laminar flow biosafety cabinet where they were demolded, cleaned by repeated dipping in a solution of 70% ethanol in water, and dried overnight in a biosafety cabinet with open sash. The clean substrates were further sterilized by five minutes of exposure to germicidal UV light (Nuaire).

2.4 Immunofluorescence

2.4.1 Staining

At experiment endpoints, cells were washed with warm PBS (Gibco) and fixed in 3.7% paraformaldehyde for fifteen minutes and stored in PBS with Ca++ and Mg++ (Corning cellgro) at 4°C until further processing. Cells were permeabolized with Triton X-100 (0.1%) and incubated in FX signal enhancer (Invitrogen). Antibodies, stains, and

blocks were incubated at room temperature for the following times in the following order: Phalloidin (Invitrogen, 1:200, 1hr), 10% normal goat serum (ThermoFisher, 30 min), mouse IgG primary (specific primaries and dilutions identified in later chapters; 1hr), Alexa-488 anti mouse IgG H+L secondary (Invitrogen, gloat polyclonal, lot 41786A, 1:500, 30 min), DAPI (Invitrogen, 1:40000, 5 min). Stained samples were mounted under coverslips (18mm x 18mm, 1.5, Fisher Scientific) with ProLong Gold Antifade (Invitrogen), and sealed and adhered to frosted microscope slides (Fisher Scientific) with speed-setting top coat nail polish (L'Oreal Paris).

2.4.2 Confocal microscopy

Detailed microscopy information is provided in the relevant later chapters. All confocal imaging in this dissertation used a Zeiss LSM 880 inverted confocal microscope system with motorized stage and Airyscan detector.

2.5 Quantification of morphology

Quantifications of morphology were performed using either live phase contrast microscopy images, or confocal imaging as described in later chapters. All quantifications of morphology used FIJI (SciJava), an expansion of Image J (NIH) open-source image analysis software [113].

2.5.1 Cell shape index

The procedure used for the determination of shape index is based on previously published protocols [80]. Blinded observers used the FIJI polygon selection tool to trace cell perimeters made visible by either phase contrast, VE-cadherin statining, or gaps in Phalloidin- tubulin double-staining. Cell area and perimeter were recorded by FIJI and

shape index (SI) was calculated using the formula $SI = \frac{4\pi(SA)}{P^2}$. Where specified, FIJI also fit an ellipse to traced cells, measured cell major and minor axis lengths, and calculated cell aspect ratio (AR) as the quotient of cell major axis length by minor axis length.

2.5.2 Whole cell alignment

Where specified, the cell traces for cell shape index were also used to determine the angle deviance between cell major axes and micropatterns. Using the fit ellipse described above, the FIJI measurement tool recorded the major axis angle of each cell. The angle deviance from patterned angle was calculated as the absolute value of the difference between the major axis angle and the pattern angle. Directionality of cell orientation was not addressed in this dissertation, therefore reported angle deviances range from 0-90°. Angle deviances for planar conditions were calculated using the angle of the patterned regions on the same sample.

2.5.3 Cytoskeletal alignment

Cytoskeletal alignment was determined on a cell-by-cell basis using a custom script written in FIJI. Airy-processed z-stacks containing either actin or tubulin single channels were segmented using the ROIs generated from the manual traces described above, virtually autofocused using the Find Focused Slices plugin to select a single slice, background subtracted using a rolling radius of 50 px, and autothresholded using the MidGrey local autothreshold tool with a radius of 15 px. The fibers in these thresholded images were automatically traced using the analyze particles tool, which selected all fibers with an area of at least 2 μm^2 and shape index of below 0.3. The major axis angle and length of the fit ellipse for each traced fiber was output for each fiber. Fiber angle deviance is calculated as described above. For the purposes of statistics, normalized

average angle deviance is calculated per cell by summing the product of each angle and fiber length and dividing this by the sum of fiber lengths.

A second script which calculates aggregate cytoskeletal alignment across a z-stack was also written. That script functions by first splitting the stack into 200 px^2 X-Y regions, and then performing the virtual autofocusing, auto local thresholding, and particle analysis as descried above. Because this aggregate approach arbitrarily determined image ROIs, fiber angle deviance was not length-normalized when calculating means. Both of the scripts described here can be found in Appendix B.

2.6 Quantification of gene expression

Protocols for cell lysis prior to RNA isolation varied between projects and are described in detail in later chapters. Following lysis, RNA was extracted from cells using an RNEasy Mini-prep kit (Qiagen) according to manufacturer instructions. RNA yield was determined using Nanodrop (Thermo scientific) and then normalized before proceeding to reverse transcription. RNA was treated with DNAse I (Fermentas) and RNA reverse transcribed to cDNA using SuperScript III Reverse Transcriptase (Life Technologies) with random primers according to manufacturer protocol.

Quantitative real-time polymerase chain reaction (qPCR) was performed using Platinum SYBR Green qPCR SuperMix-UDG, ROX reference dye (Invitrogen), and a commercially available thermocycler (specified in later chapters). Regardless of platform, qPCR was run using a custom program: 50°C for 2 min, 95°C for 2 min, 42 cycles of 95°C for 15s followed by 60°C for 30s. Gene expression was determined using previously validated primers [81,108]. Primer sequences are shown in table 2.1. Following runs, a well-by-well quality check was performed using melt curves and variation between technical replicates. Samples were excluded if melt curves varied from

those predicted, or if technical replicate cycle threshold standard deviation exceeded 1. Changes in gene expression were calculated using the ΔΔCT method, with Glyceraldehyde 3-phosphate dehydrogenase (GAPDH) serving as housekeeping gene for the calculation of ΔCT, and non-patterned CaECs as the reference group for calculation of ΔΔCT. All statistics were calculated using ΔCT. For the purposes of statistics, each culture substrate is considered a biological replicate.

Table 2.1: Primer sequences for qPCR.

Previously validated primers for use in all gene expression studies

Gene	Forward	Reverse
GAPDH	CCTCAACGACCACTTTGTCA	TTACTCCTTGGAGGCCATGT
VCAM-1	GGGAAGATGGTCGTGATCCTT	TGAGACGGAGTCACCAATCTG
vWF	CCTATTGGAATTGGAGATCGCTA	CTTCGATTCGCTGGAGCTTC
KLF-2	CACCGGGTCTACACTAGAGG	AAATGCCGCAGACAGTACAA
eNOS	ATCTCCGCCTCGCTCATG	AGCCATACAGGATTGTCGCCT
E-Selectin	GAAGGATGGACGCTCAATGG	AGTGGGAGCTTCACAGGTAG

2.7 *Ex vivo* arteriovenous shunt

2.7.1 Shunt placement

A silicone shunt was surgically implanted between the femoral artery and femoral vein. For this procedure, anesthesia was induced by ketamine (10-20 mg/kg intramuscularly) and Telazol (3-5 mg/kg intramuscularly) and maintained with 1-3% isoflurane delivered at 1-2 L/min in oxygen. Each leg is independently shunted, with at least five days between surgery and shunt studies.

2.7.2 Shunt studies

Autologous platelets were radiolabeled with ^{111}In and re-infused weekly as described previously [106]. Homologous fibrinogen was radiolabeled with ^{125}I and injected daily, prior to each study [114]. A complete blood count (CBC) was performed daily to track the animal's platelet count and calculate platelet deposition from ^{111}In signal. For the studies, the femoral arteriovenous shunt loop was extended with silicone tubing (Technical Products, Inc., 760 mm long, 3.18 mm ID, 6.35 mm OD). This tubing was connected to either test graft devices wrapped in heat-shrink tubing, or to test flow diverter devices deployed in a separate connected length of silicone tubing. Devices were centered over a gamma scintillation camera (model varies, see later chapters) which quantified ^{111}In deposition in one- or three-minute frames over each 60-minute study. The rate of blood flow through the shunt loop was monitored with an ultrasonic flow probe (Transonic Systems, Inc.) proximal to the test device and maintained at 0.1 L/min (shear rate of 265s^{-1}) using a clamp distal to the device. A photograph of the experimental setup can been seen in Figure 5.1.

Real-time platelet deposition was calculated within a 10 cm box centered on the device and normalized to the animal's platelet count. In cases of shunt occlusion before the end of the 60-minute trial, the platelet deposition value at time of occlusion was duplicated for the remaining time slots.

2.7.3 Light transmission platelet aggregometry

During studies including the use of the antiplatelet drugs acetylsalicylic acid (ASA, also known by trade name aspirin) or clopidogrel (also known by trade name Plavix), the platelet response to known agonists was evaluated using light transmission platelet aggregometry (LTPA). For at least two shunt studies in each antiplatelet group

(no antiplatelet, ASA alone, DAPT), baboon arterial blood was drawn from the arteriovenous shunt (9:1v/v into 3.8% sodium citrate). Platelet rich plasma (PRP) and platelet poor plasma (PPP) were isolated via consecutive centrifugations. Following a CBC on raw PRP, a working solution containing 2×10^5 platelets/µL was prepared by diluting PRP in PPP. Platelet aggregometry was performed using a Model 440 Dual Aggregometer (Chrono-Log Corporation) connected to a Model 707 chart recorder (Chrono-Log). Remaining PPP was used as an absorbance reference. Light transmission was recorded for at least 30 s prior to agonist addition. The ASA effect was assayed by adding arachidonic acid (Bio/Data Corp) to a final plasma concentration of 613 µmol/L, while clopidogrel activity was assayed with 80 µmol/L adenosine diphosphate (ADP, Sigma Chemical Co.). Light transmission was recorded for at least four minutes after agonist addition. For the purposes of quantification, percent aggregation was calculated at 90s and 180s after agonist addition. On days when no platelet response was expected based on antiplatelet use, venous blood from an untreated baboon was used as an agonist positive control.

Chapter III: Static spatial growth restriction micropatterning of endothelial colony forming cells influences their morphology and gene expression[7]

3.1 Abstract:

Background: Endothelialization of small diameter synthetic vascular grafts is a potential solution to the thrombosis and intimal hyperplasia that plague current devices. Endothelial colony forming cells, which are blood-derived and similar to mature endothelial cells, are a potential cell source. Anisotropic spatial growth restriction micropatterning has been previously shown to affect the morphology and function of mature endothelial cells in a manner similar to unidirectional fluid shear stress. To date, endothelial colony forming cells have not been successfully micropatterned. This study addresses the hypothesis that micropatterning of endothelial colony forming cells will induce morphological elongation, cytoskeletal alignment, and changes in immunogenic and thrombogenic–related gene expression.

Methods: Spatially growth restrictive test surfaces with 25 μm-wide lanes alternating between collagen-I and a blocking polymer were created using microfluidics. Case-matched endothelial colony forming cells and control mature carotid endothelial cells were statically cultured on either micropatterned or non-patterned surfaces. Cell

[7] This work was originally published in *PLoS ONE.* Hagen MW, Hinds MT. Static spatial growth restriction micropatterning of endothelial colony forming cells influences their morphology and gene expression. *PLoS ONE*. 2019; 14 (6): e0218197.

elongation was quantified using shape index. Using confocal microscopy, cytoskeletal alignment was visualized and density and apoptotic rate were determined. Gene expression was measured using quantitative PCR to measure KLF-2, eNOS, VCAM-1, and vWF.

Results: Endothelial colony forming cells were successfully micropatterned for up to 50 hours. Micropatterned cells displayed elongation and actin alignment. Micropatterning increased the packing densities of both cell types, but did not affect apoptotic rate, which was lower in endothelial colony forming cells. KLF-2 gene expression was increased in micropatterned relative to non-patterned endothelial colony forming cells after 50 hours. No significant differences were seen in the other genes tested.

Conclusions: Endothelial colony forming cells can be durably micropatterned using spatial growth restriction. Micropatterning has a significant effect on the gross and subcellular morphologies of both cell types. Further study is required to fully understand the effect of micropatterning on endothelial colony forming cell gene expression.

3.2 Introduction

Durable artificial small-diameter synthetic vascular grafts for the treatment of vascular occlusions represent a critical unmet need in modern medicine. Autologous grafting is the current clinical standard for arterial bypass procedures, however limited availability and donor site complications make a substantial portion of the potential patient population ineligible for autologous vessel harvesting [5]. Given that currently available synthetic biomaterials including ePTFE show limited patency at diameters less than 6 mm, this leaves many patients without viable alternatives [115,116]. One potential solution to this problem is the use of biomaterials endothelialized *in vitro* prior to implantation. The pre-implant establishment of a functional endothelium is capable of limiting the thrombosis and neointimal hyperplasia which limit patency and lead to graft failure.

One potential autologous source of endothelium is the harvesting of ECFCs from a venous blood draw. ECFCs are outgrowth products of circulating endothelial progenitors which can be readily prepared in the laboratory by culturing the mononuclear cell-containing buffy coat of mammalian blood with pro-endothelial growth factors including VEGF [87,89]. The minimally-invasive accessibility of EPCs and the endothelial-like nature of fully differentiated ECFCs make them a promising candidate for tissue engineering applications. Several groups, including our own, have performed proof-of-concept studies showing that mature primary EC [117,118] and ECFC [106,119] pre-seeding improve the performance of artificial vascular grafts, suggesting that ECFCs could serve as a cell source for an *in vitro* endothelialization approach.

The primary strength of ECFCs as a tissue engineering tool is their similarity in form and function to mature ECs. As the functional interface between flowing blood and the vascular wall, healthy ECs are responsible for the maintenance of hemostasis as

well as the prevention of thrombosis and the management of inflammation. The health of EC subpopulations within an individual is substantially influenced by the mechanical environment in which the cells reside. Early studies of atherosclerosis revealed that plaques are most likely to form at sites where the arterial wall is exposed to non-uniform and oscillatory fluid shear stress, while regions where ECs are exposed to unidirectional non-reversing shear stress are largely spared of atherosclerotic lesions [46]. On a cellular level, both ECs and ECFCs exposed to unidirectional fluid shear stress are seen to elongate in the direction of fluid flow, while those exposed to disturbed flow maintain the rounded, cobblestone shape typical of both cell types in static culture [105,120]. Experiments have revealed a number of beneficial functional consequences of unidirectional fluid shear on ECs *in vitro* and *in vivo* and ECFCs *in vitro*, detectable through changes in gene expression. For example, the downregulation of adhesion molecules such as ICAM-1 and VCAM-1, which are known to promote early atherogenic inflammation is seen in ECs [121] but not in ECFCs [105], while upregulations of antithrombotic factors including eNOS and TFPI are seen in both ECFCs and ECs [104]. Unidirectional fluid shear stress also drives an upregulation in KLF-2, a transcription factor believed to be a primary driver of the beneficial fluid shear response seen in the endothelium in ECs [54], however to our knowledge this response has yet to be studied in ECFCs. Notably, computational modeling reveals that the fluid flow within the end-to-side anastomoses most commonly used in vascular bypass procedures is highly non-uniform and oscillatory [122,123]. Thus, grafts pre-endothelialized with either cell type are immediately upon implantation subject to detrimental fluid shear stress limiting their potential clinical benefit.

Importantly, it has been shown that mature EC morphology and function are influenced in static tissue culture through anisotropic substrate micropatterning (reviewed in [78]). Our group and others have extensively used spatial growth restriction

micropatterning to confine various cell types to predefined lanes, thus controlling their shape and migration [80,112,124]. It has been shown that primary mature ECs exhibit both robust cytoskeletal alignment [80,125] and anti-inflammatory changes in gene expression, including downregulations of VCAM-1 and increases in KLF-2 expression [81]. Similarly, many groups have demonstrated their ability to manipulate EC morphology using topographic micropatterning with pitches ranging from 0.5-4 μm [78,84]. Given the substantial influence of fluid shear stress on EC functionality, and the non-uniform oscillatory flow profile of the end-to-side anastomoses in bypass grafting, micropatterning of vascular graft biomaterials has the potential to induce a non-thrombogenic endothelium.

While ECFCs have been shown to have a fluid shear stress response similar to ECs [105] as discussed above, past attempts to micropattern them through spatial growth restriction using alternating lanes of collagen-I and bovine serum albumin (BSA) have proven to be technically infeasible due to ECFCs' comparatively more robust matrix remodeling abilities [107]. In this study, we demonstrate the use of a food grade block copolymer to prevent ECFC spreading between lanes. We use this technique to test our hypotheses that, similar to mature ECs, micropatterned ECFCs in static culture will display a more elongated morphology and altered gene expression relative to non-patterned ECFCs. Specifically, we expect to see relative upregulations of KLF-2 and eNOS, and downregulations of prothrombotic and adhesion molecules in micropatterned ECFCs relative to non-patterned ECFCs.

3.3 Materials & Methods

3.3.1 Primary cell isolation and culture

All animal work necessary for the isolation of primary cells for this study was approved by the Oregon National Primate Research Center Institutional Care and use Committee (IP00000049). A detailed ethics statement can be found in section 2.1. Detailed descriptions of the housing, care, and humane euthanasia of these primates has been published previously [106].

This study made use of case-matched primary CaECs and ECFCs from two juvenile male *papio Anubis* baboons. Detailed descriptions of primary cell isolations can be found in section 2.2. Cells used in this study were isolated and maintained in complete endothelial growth medium (EGM-2, Lonza) supplemented with FBS as described in Chapter II.

3.3.2Micropatterning experiments

The preparation of spatially growth restrictive substrates is described in section 2.3.1.

Animal-matched ECs and ECFCs were seeded onto micropatterned substrates at $4.55x10^3$ cells / cm^2 and allowed to attach for one hour. Non-attached cells were then washed away and cultures were fed. Cultures were maintained without additional feeding for either 24 or 50 hours before processing. Where noted, cells were challenged using 100 U/mL tumor necrosis factor α (TNF, R&D Systems) via a 1/3 feed for two hours prior to experimental end points. Non-TNF treated samples were given a 1/3 feed of unmodified media at the same time point.

3.3.3 Quantifying morphology

Cultures were imaged live after 22 or 48 hours (immediately prior to TNF stimulation) using a phase-contrast enabled 20X objective on a Nikon Eclipse TE 2000-U microscope. Two images per culture were captured and given to a blinded volunteer who manually traced 5-10 cells per image from which SI was calculated as described in section 2.5. One biological replicate in the 50 hour micropatterned EC group was excluded due to poor patterning likely resulting from a defective PDMS stamp used in substrate preparation.

3.3.4 Immunofluorescence and super-resolution microscopy

Cells were fixed and stained as described in section 2.4 using a primary antibody against VE-Cadherin (Santa Cruz Biotechnology, monoclonal, clone F-8, lot 1605, 1:100). Low-magnification immunofluorescence images were collected using a 10X PlanApo objective NA = 0.45. Z-stacks are presented in figures as maximum intensity Z-projections. Super-resolution microscopy (SRM) imaging was accomplished using a 20X PlanApo objective NA = 0.8 and Fast Airyscan detector array. SRM images were collected as single-slices in order to observe cytoskeletal elements at a resolution of $7nm^2$ / pixel. Automatic airy processing was performed using Zen Black (Zeiss), and post-processing of all images was performed using FIJI (SciJava) [113].

3.3.5 Quantifying cell density and rates of apoptosis

Cell density and apoptotic rate were quantified using an unbiased counting method and systematic random sampling. Four samples per combination of cell type (EC, ECFC), micropattern, and culture time (24 hour, 50 hour) were fixed and stained as

described above. Three high-resolution low-magnification 10X confocal 850 µm x 850 µm images per sample were collected as described above. These images were imported into FIJI and a random grid with 10,000 μm^2 gridcells was generated over the image using FIJI's grid tool. Starting in the top left of the image, counting frames were defined as the top left cell in each 2x2 group, such that 16 counting frames per image were selected. Within each counting frame, cell nuclei were counted as either healthy or pyknotic (dense and/or fractured in appearance). All frames were counted by a single blinded individual. In order to ensure the accuracy of the density estimate, only nuclei which were either entirely contained in the counting frame or were partially touching the bottom or left edges of the counting frame were counted. Total cell density is defined as healthy + pyknotic nuclei, while percent apoptotic cells is defined as the ratio of pyknotic to total counted nuclei. To enable an accurate comparison between micropatterned and non-patterned cell densities, counted micropattern densities were doubled to account for the fact that only half of the surface area was available for cell attachment. For the purposes of statistical analysis, each culture trial was considered one biological replicate.

3.3.6 Quantifying gene expression

Non-patterned cells were manually scraped off of culture substrates using a glass aspirating tip. Cells were passaged from micropatterned or non-patterned control substrates using TrypLE, resuspended in Buffer RLT (Qiagen) with 1% β-mercaptoethanol, and RNA extracted. On a per-trial basis, RNA was normalized to between 25-35 ng before reverse transcription. RNA isolation, reverse transcription, and qPCR are described in detail in section 2.6. qPCR was carried out using either the 7500 Fast Real Time PCR system or the QuantStudio 3 (Applied Biosystems, both). -ΔΔCT values are reported in figures and in text.

3.3.7 Statistics

Results are reported as mean ± standard deviation. All statistics were calculated using R (R foundation for statistical computing, version 3.5.1) [126] , and R packages Infer (version 0.3.0) [127], and multcomp [128]. Comparisons of cell density and apoptotic rate were performed using multi-way ANOVAs with coefficients for micropatterning, culture time, cell type, and interactions as appropriate. Where interactions were involved, specific between-groups differences were calculated using the general linear hypothesis test based on manually constructed linear combinations, and multiple-comparison p-values corrected using the Holm method. Because each factor contained only two levels, post hoc testing was not necessary when no statistically significant interactions were involved. The appropriateness of parametric methods was confirmed by ensuring balanced sample sizes, and examining model quantile-quantile plots and fitted versus residual value plots.

Because of unbalanced sample sizes and the non-normal distributions of shape index and qPCR data, these comparative statistical tests were performed using two-sample, one-tailed, 10,000 replicate permutation tests [129]. These nonparametric one-tailed tests were set up to test the specific hypotheses addressed here, specifically, that micropatterning reduces shape index, VCAM-1, and vWF gene expression, and increases KLF-2 and eNOS gene expression. For all results displayed, each culture dish is considered a biological replicate. Results were considered statistically significant when $p < 0.05$.

3.4 Results

3.4.1 Polymer-based method effectively spatially restricts ECFC growth into micropatterned lanes

First the ability of the modified micropatterning procedure to effectively spatially restrict ECFC growth on tissue culture plastic was assessed (Fig 3.1). Live phase-contrast light microscopy revealed well-defined lanes of ECFCs on patterned substrates (Fig 3.1D) with minimal crossover occurring at both 22 and 48 hours, suggesting that the modified procedure did effectively spatially growth-restrict ECFCs, to an extent similar to that seen in micropatterned ECs (Fig 3.1B)

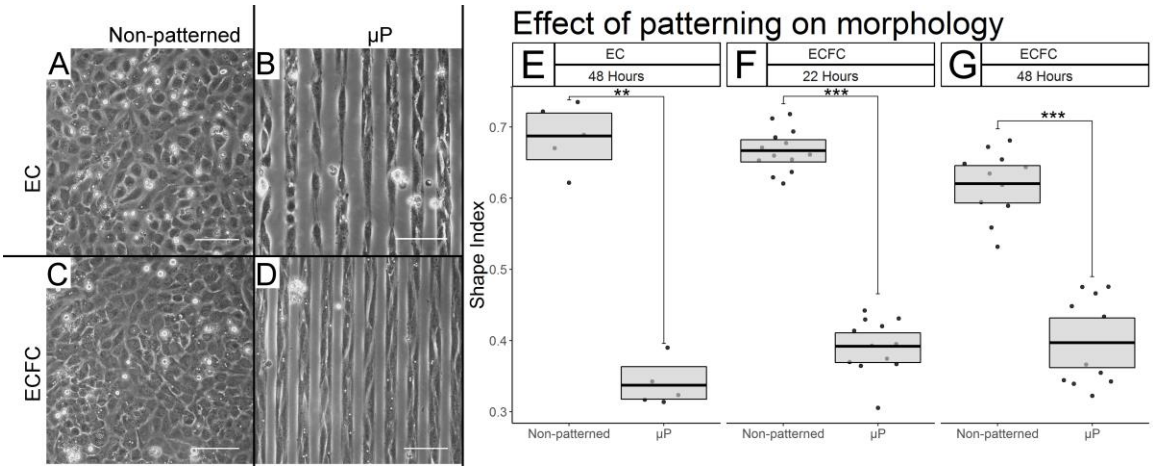

Fig 3.1: Spatial growth restriction micropatterning effectively growth restricts ECFCs and affects their gross morphology

Representative phase contrast light microscopy after 48 hours of culture at 20X (A-D) reveals effective growth restriction in ECs (B vs. A), and ECFCs (D vs. C) Scale bars = 100 μm. (E-G) Shape index quantification of EC and ECFC elongation. Box limits represent bootstrapped 95% confidence intervals, and crossbars represent means. Each point represents the mean SI of the 5-10 cells traced from each biological replicate. We find statistically significant micropatterning effects in ECs after 50 hours (E, $p = 0.0052$), and in ECFCs after 24 (F, $p < 0.0001$) and 50 hours (G, $p < 0.0001$).

3.4.2 Spatial growth restriction micropatterning has a substantial effect on ECFC elongation

After the efficacy of growth restriction was confirmed, the effect of micropatterning on the shape of individual ECFCs was assessed using shape index (SI), a measure of roundness, calculated as a ratio of surface area to perimeter such that SI = 0 represents a straight line and SI = 1 a perfect circle. After 22 hours, a dramatic reduction in SI was observed in micropatterned (μp) relative to non-patterned ECFCs from 0.667 ± 0.148 to 0.393 ± 0.132 (Fig 3.1F, $p < 0.0001$, N = 13 (non-patterned), 12 (μp)). This difference in shape index was maintained after 50 hours of culture time (Fig 3.1G, $p < 0.0001$, non-patterned = 0.626 ± 0.155, μp = 0.362 ± 0.132, N = 11 each). The SI of micropatterned and non-patterned ECs was also calculated as a reference point after 50 hours for reference and showed a nearly identical degree of elongation (Fig 3.1E, $p = 0.0052$, non-patterned = 0.683 ± 0.154, μp = 0.337 ± 0.111, N = 5 each).

3.4.3 Micropatterning drives alignment of the ECFC actin cytoskeleton

The effect of micropatterning on the subcellular architecture of ECFCs was characterized after 24 hours of culture time. Super-resolution imaging of the actin cytoskeleton of non-patterned ECFCs showed random organization of actin fibers (Fig 3.2A), whereas micropatterned ECFC actin fibers were aligned (Fig 3.2B). A similar degree of relative alignment was seen in micropatterned ECs relative to non-patterned ECs (Figs 3.2C and 3.2D). Non-patterned ECs and ECFCs had a uniform distribution of actin fibers throughout the cytoplasm, whereas both cell types displayed a concentration of actin at their peripheries when micropatterned. Interestingly, although all cultures were

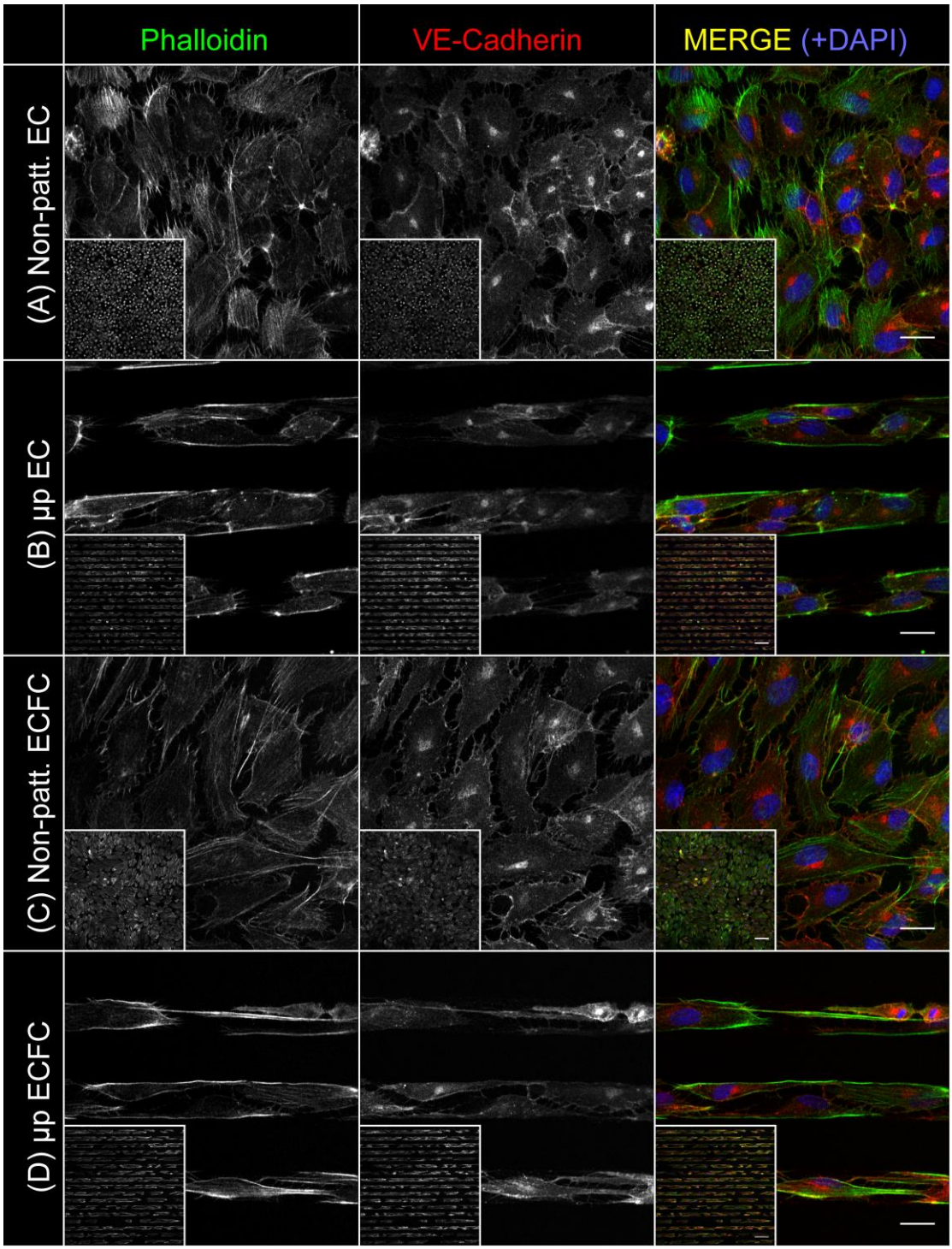
Phalloidin
VE-Cadherin
MERGE (+DAPI)
(A) Non-patt. EC
(B) µp EC
(C) Non-patt. ECFC
(D) µp ECFC

Fig 3.2: Micropatterned cells show subcellular alignment and peripheral aggregation of actin.

ECFCs and ECs were stained and imaged using laser scanning confocal microscopy with a super-resolution airyscan detector in order to assess actin distribution and alignment after 24 hours of culture. Representative images of non-patterned ECFCs (A), micropatterned ECFCs (B), non-patterned ECs (C), and micropatterned ECs (D) after 24 hours in culture are shown. Each image series shows phalloidin (actin), VE-Cadherin, and a pseudocolor merge with phalloidin in green, VE-Cadherin in red, and a DAPI nuclear stain in blue. Main panel scale bars are 20 µm. Inset panels are 10X maximum Z-projections, with scale bars of 100 µm.

seeded to confluence, some interruptions in the VE-Cadherin cell-cell contacts were visible in all conditions examined.

3.4.4 Micropatterning increases EC and ECFC density, but has no effect on apoptotic rate

EC and ECFC density and apoptotic rate were quantified by counting nuclei in stained cultures (Fig 3.3A). Micropatterning significantly increased the densities of both cell types (Fig 3.3B, ANOVA $F_{1,24} = 20.21$, $p = 0.0002$). Cell type also significantly affected density (ANOVA $F_{1,24} = 14.68$, $p = 0.0008$), as did culture time (ANOVA $F_{1,24} = 34.13$, $p = 5.03 \times 10^{-6}$), however these factors significantly interacted (ANOVA $F_{1,24} = 16.22$, $p = 0.0005$). After 24 hours of culture time, non-patterned ECs were more densely packed than non-patterned ECFCs (EC 839 ± 51 cells / mm^2, ECFC 530 ± 80 cells / mm^2; $p = 0.0024$), and micropatterned ECs were likewise more densely packed than micropatterned ECFCs (EC 553 ± 130 cells / mm^2, ECFC 373 ± 66 cells / mm^2; $p = 0.011$), while after 50 hours of culture time there was no significant difference between non-patterned ECs and ECFCs (EC 992 ± 68 cells / mm^2, ECFC 979 ± 29 cells / mm^2, $p = 1$), or micropatterned ECs and ECFCs (EC 554 ± 39, ECFC 570 ± 51 cells / mm^2, $p =$

1). The density of ECs did not change significantly between 24 and 50 hours of culture time regardless of micropatterning (p = 1 non-patterned, p = 0.689 µp, see means above), while the density of ECFCs increased significantly under both conditions (p = 0.0009 non-patterned, p = 0.0002 µp, see means above).

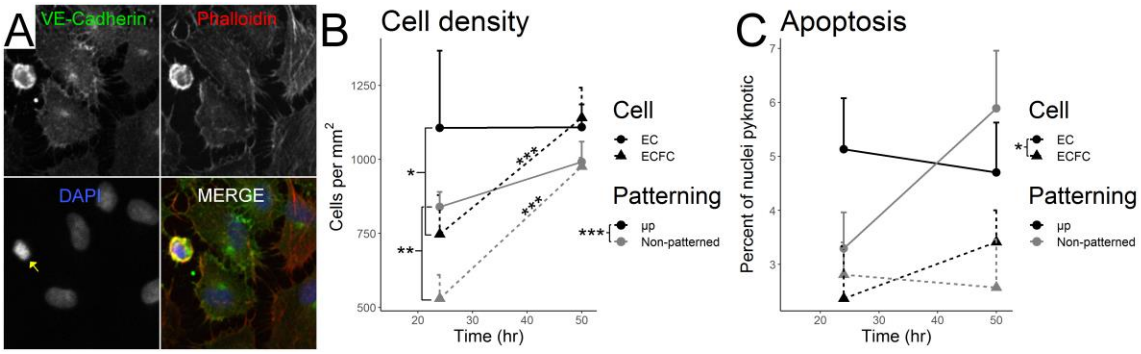

Fig 3.3: Micropatterning significantly increases cell density.
EC apoptotic rate is higher than ECFC, regardless of micropatterning. Stained EC and ECFC nuclei were counted in order to quantify cell density and apoptotic rate. (A) Representative micrograph of a pyknotic nucleus (yellow arrow, DAPI channel) surrounded by healthy cells in a non-patterned EC sample after 50 hours of culture. (B) Micropatterning significantly increases cell density across other culture conditions (p = 0.0002). Post-hoc testing showed significantly greater EC than ECFC density at 24 hours in both non-patterned (p = 0.0024) and micropatterned cells (p = 0.011), however no significant cell-type differences existed after 50 hours (p = 1, both). As noted by stars above trend lines, ECFC density significantly increased between 24 and 50 hours of culture time in both non-patterned (p = 0.0009) and micropatterned (p = 0.0002) cultures, while EC density did not (p = 1 non-patterned, p = 0.689 µp). (C) ECs showed a significantly greater rate of apoptosis than ECFCs across culture conditions (p = 0.0151), however micropatterning (p = 0.732) and culture time (p = 0.336) had no significant effects on apoptotic rate.

A greater portion of ECs were apoptotic compared to ECFCs across culture conditions (Fig 3.3C, ANOVA $F_{1,28}$ = 6.71, p = 0.0151), while micropatterning and culture time had no significant effects (micropatterning $F_{1,28}$ = 0.12, p = 0.732; culture time $F_{1,28}$

= 0.958, p = 0.336) with no interactions (at 24 hours: non-patterned ECs 3.29 ± 1.7% apoptotic, µp ECs 5.13 ± 2.6%, non-patterned ECFCs 2.81 ± 1.7%, µp ECFCs 2.37 ± 1.1 %. At 50 hours: non-patterned ECs 5.89 ± 2.8% apoptotic, µp ECs 4.7 ± 3.3%, non-patterned ECFCs 2.57 ± 1.3%, µp ECFCs 3.41 ± 2.2%.).

3.4.5 Micropatterning has a modest effect on ECFC transcriptional regulation over time

After demonstrating the effectiveness of spatial growth restriction on the gross and subcellular morphology of ECFCs, qPCR was used to determine its effect on KLF-2, which is recognized as a master regulator of the EC response to unidirectional FSS *in vivo*. After 24 hours, ECFCs showed no discernible micropatterning effect on KLF-2 expression (Fig 3.4B, p = 0.550, N = 25 non-patterned, 11 µp), however a statistically significant effect did appear after 50 hours of culture time (Fig 3.4D, p = 0.0328, N = 12 non-patterned, 10 µp), suggesting that micropatterning did encourage an increase in KLF-2 expression at the later time point. Interestingly, no significant effect of micropatterning was seen on EC expression of KLF-2 at either time point (Fig 3.4A,C, for 24 h: p = 0.327; N = 21 non-patterned, 15 µp; for 50h: p = 0.211; N = 12 non-patterned, 11 µp).

3.4.6 eNOS gene expression is not significantly affected by micropatterning

Given the importance of nitric oxide as a vasodilator and antiplatelet agent, the effect of micropatterning on the expression of the eNOS gene was also measured. No statistically significant effect of micropatterning was seen at either time point in ECFCs (Fig 3.5B,D. For 24h: p = 0.1423; N = 17 non-patterned, 10 µp. For 50h: p = 0.1169; N =

11 non-patterned, 6 µp). or ECs (Fig 3.5A,C: For 24h: p = 0.1199; N = 20 non-patterned, 13 µp. For 50 h: p = 0.0986; N = 9 each).

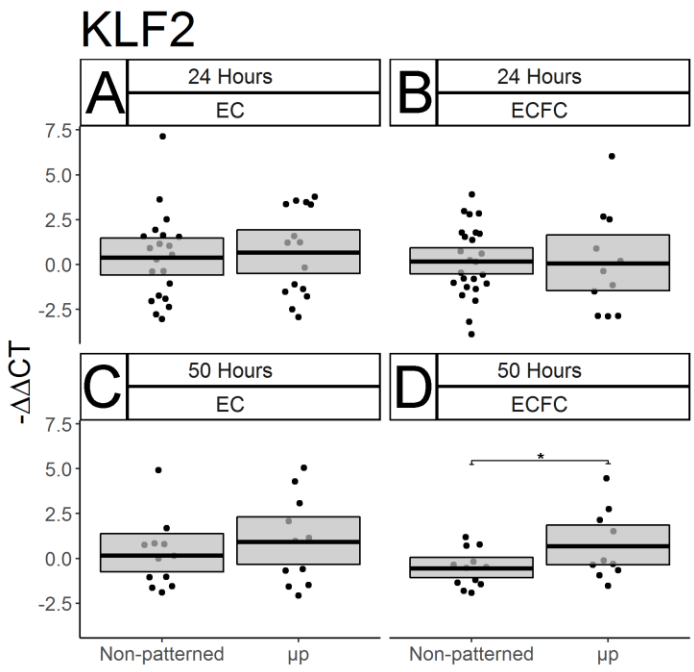

Fig 3.4: Micropatterning has a time-dependent effect on ECFC transcriptional regulation.

The expression of the transcriptional regulator KLF-2 was measured in ECs and ECFCs after 24 and 50 hours using qPCR. Results are displayed as –ΔΔCT. Box limits represent bootstrapped 95% confidence intervals. Each point represents one biological replicate. No effect of micropatterning on EC KLF-2 expression was seen after 24 or 50 hours (A, C). Nor was any change seen in ECFCs after only 24 hours (B, p = 0.550), however a significant increase in KLF-2 expression was seen in ECFCs after 50 hours (D, p = 0.0328).

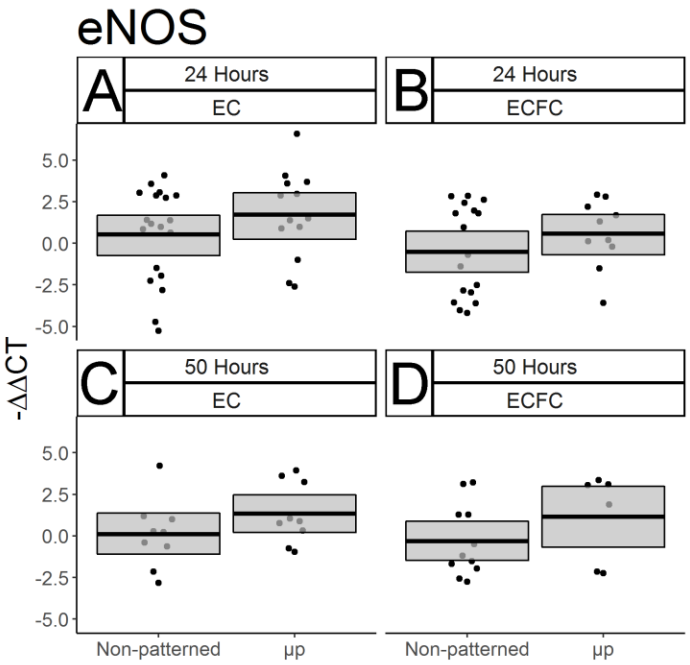

Fig 3.5: ECFC eNOS gene expression after micropatterning.
qPCR was used to measure EC and ECFC gene expression of eNOS with and without micropatterning after 24 and 50 hours of culture. Results are displayed as –ΔΔCT. Box limits represent bootstrapped 95% confidence interval. Each point represents one biological replicate. In both cell types, and at both time points measured, no statistically significant differences in eNOS expression were seen in response to micropatterning. (A) ECs after 24 hours. (B) ECFCs after 24 hours. (C) ECs after 50 hours, (D) ECFCs after 50 hours.

3.4.7 Micropatterning did not significantly impact pro-inflammatory and pro-thrombotic gene expression by ECFCs

The effect of spatial growth restriction micropatterning on pro-inflammatory and pro-thrombotic gene expression by mature ECs and ECFCs was also characterized. In order to amplify the baseline gene expression of VCAM-1, cells were treated with 100 U/mL TNF prior to collection and RNA isolation. Substantial increases of VCAM-1

expression in TNF-treated non-patterned ECs relative to untreated non-patterned ECs after 22 hours of culture and two hours of cytokine treatment (Fig 3.6A, $p < 0.0001$, N = 16 non-treated, 18 TNF treated), and after 48 hours of culture and two hours of cytokine treatment (Fig 3.6B, $p = 0.0004$, N = 14 non-treated, 7 TNF treated) were observed. This increase was likewise seen in ECFCs after 22 hours of culture and two hours of TNF treatment (Fig 3.6B $p < 0.0001$, N = 14 non-treated, 16 treated) and after 48 hours of culture and two hours of TNF treatment (Fig 3.6D, $p = 0.0003$, N = 14 non-treated, 7 treated). No effect of micropatterning was seen on VCAM-1 expression in either cell type or time point (Fig 3.6A-D, $p > 0.2$, N between 5-18 throughout). Expression of the gene encoding vWF, a molecule secreted by ECs *in vivo* which, among other things, recruits platelets to a nascent clot was also measured. No noticeable micropatterning-driven differences were seen after the first 24 hours of culture (Fig 3.7A, $p > 0.1$, N between 9-18, both), or after 50 total hours of culture (Fig 3.7B, $p > 0.1$, N between 5-11, both). Interestingly, there was evidence of a cell type effect after 24 hours, with non-patterned ECFCs expressing more of the gene than ECs (Fig 3.7A vs. B), however the extent of this difference decreased after 50 hours of culture (Fig 3.7C vs. D). Because this difference was not among the hypotheses we designed the study to test in the original experimental design, this difference was not tested statistically.

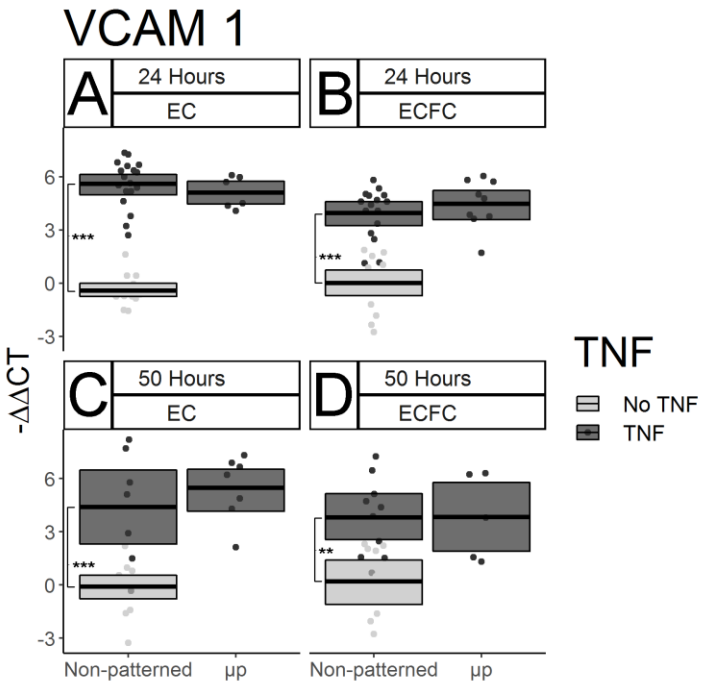

Fig 3.6: Micropatterning has no discernible effect on inflammatory molecule gene expression in ECs or ECFCs.

VCAM-1 gene expression was measured by qPCR in ECs and ECFCs after 24 and 50 hours of culture. Data are displayed as –ΔΔCT. TNF was added for the final two hours of culture. Box limits represent bootstrapped 95% confidence intervals and crossbars represent means. Each point represents one biological replicate. Light gray boxes and points represent gene expression for non-patterned, non-TNF treated cells in each cell type and time point. TNF efficacy at stimulating increased VCAM-1 gene expression was confirmed in each cell type at both time points. (A) ECs after 24 hours ($p < 0.0001$). (B) ECFCs after 24 hours ($p < 0.0001$). (C) ECs after 50 hours ($p < 0.0001$). (D) ECFCs after 50 hours ($p = 0.0003$). No micropatterning-dependent difference in TNF stimulated VCAM-1 expression was seen in either cell type at either time point.

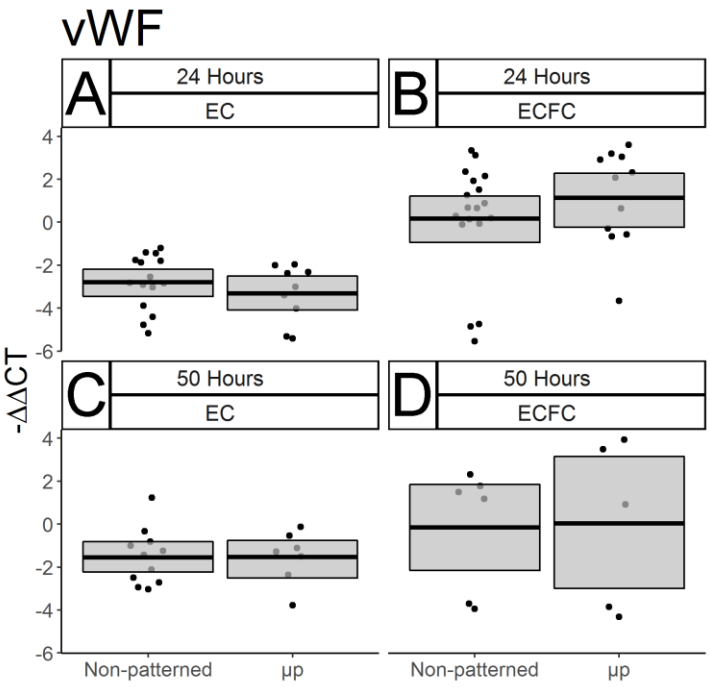

Fig 3.7: Micropatterning has no discernible effect on the expression of the prothrombotic von Willebrand factor in ECs or ECFCs.

vWF gene expression was measured by qPCR in ECs and ECFCs after 24 and 50 hours of culture. Results are displayed as –ΔΔCT. Box limits represent bootstrapped 95% confidence intervals, and crossbars represent means. Each point represents one biological replicate. No statistically significant micropatterning-driven differences were seen in any of the conditions tested: (A) ECs after 24 hours, (B) ECFCs after 24 hours, (C) ECs after 50 hours, (D) ECFCs after 50 hours. Notably, an increase in vWF expression was seen in ECFCs over ECs after 24 hours (A vs. B).

3.5 Discussion

To our knowledge, this study represents the first successful demonstration that ECFC morphology and gene expression can be manipulated in static culture. While the ECFC literature contains conflicting reports on the degree of similarity between ECFCs and mature ECs [89], in our non-human primate model, ECFCs are remarkably similar to ECs in morphology and function [102,104,106,130]. Our earlier studies revealed similar expression levels of the genes and cell surface proteins that regulate monocyte adhesion, tight junction formation, and platelet activation between ECs and ECFCs both basally and following TNF stimulation [103]. We furthermore previously showed similar performances of EC and ECFC-seeded vascular grafts in our *ex vivo* shunt model of platelet and fibrin accumulation [103]. However, ECs and ECFCs do have a few notable differences: ECFCs have a much lower basal level of eNOS gene expression [103], and are capable of higher rates of proliferation and extracellular matrix remodeling in culture than ECs [107,130]. We have hypothesized that this latter difference is the primary reason that a prior attempt to micropattern ECFCs was not successful: the use of BSA to block ECFC expansion between patterned lanes was not sufficient to overcome the enhanced proliferation and remodeling ability of these cells [107]. Through the use of an increased concentration of Pluronic, a previously validated [112] food-grade hydrophobic polymer, we have created the conditions for durably elongated ECFCs under static culture conditions for longer periods of time.

In further characterizing the effect of micropatterning on the morphology of our ECFCs, we have seen highly significant and consistent cell elongation, as represented by the decreased shape indices shown in Fig 3.1. These results were both internally consistent with the case-matched ECs we observed in this study, and with the SI values of mature statically micropatterned ECs and *in vivo* flow-elongated ECs reported on

previously [80]. Confocal microscopy was used to demonstrate that the degree of alignment in the actin cytoskeletons of our ECs and ECFCs was similar. Imaging of the actin cytoskeleton further revealed the high concentration of the actin cytoskeleton into dense peripheral bands, as seen previously in micropatterned ECs [80].

We also quantified the density and apoptotic rates of ECs and ECFCs with and without micropatterning at multiple time points. As shown in Fig 3.3, we found that both ECs and ECFCs were more densely packed when seeded onto micropatterned rather than non-patterned surfaces. This arguably contradicts an early study of mature EC growth restriction which found that proliferation decreases with the width of the ECM substrate on which cells are allowed to grow [79]. However, these earlier studies measured tritiated thymidine uptake, an indicator of active proliferation, whereas we measured static density. Interestingly, we found cell-type specific effects of both density and apoptotic rate. Regardless of micropatterning, ECFC density increased between 24 and 50 hours, while no significant changes were seen in EC density over the same period. Additionally, ECs showed a consistently greater rate of apoptosis over ECFCs regardless of micropatterning or culture time, suggesting that ECFCs have both a greater proliferative potential and resilience against culture conditions than ECs.

In addition to demonstrating the efficacy of our spatial growth restriction technique on the modulation of ECFC morphology, density, and survival, we used qPCR to approximate the function of micropatterned ECFCs by measuring the expression of key genes. We showed that after two days of micropatterned culture, the expression of KLF-2, a master regulator of EC responses to fluid shear stress *in vivo* [56], was significantly elevated in ECFCs relative to non-patterned ECFCs, suggesting that ECFC gene expression, as well as morphology, can be manipulated statically through spatial growth restriction micropatterning. However we did not see any significant effect of

micropatterning on the expression of eNOS, an antithrombotic factor which is basally under-expressed in ECFCs [130].

While the results of our gene expression study do show some support of our hypothesis that static micropatterning will drive resistance to immunogenic and thrombogenic stimuli in the form of increased KLF-2 expression, we observed notable differences between the current study and previous work [81]. Previously, there were significant decreases in basal VCAM-1 in micropatterned versus non-patterned ECs at 24 hours; however here we saw no discernible effect of micropatterning on TNF stimulated VCAM-1 expression. Additionally, in the previous work there had been an approximate doubling in KLF-2 expression in micropatterned ECs after 48 hours, while we saw only a very slight, and statistically non-significant increase in KLF-2 in micropatterned ECs after 50 hours here. There are three important factors which may explain these discrepancies: animal variability, TNF dosage and timing, and culture media serum content. Our previous study examined ECs isolated from a single primate, while this study used animal-matched cells from two different individuals, neither of which was included in the original study. Additionally, our previous study measured basal VCAM-1 expression [81], while we chose to stimulate VCAM-1 with a two-hour TNF treatment. This treatment is shorter than that used in our earlier flow cytometry characterizations of ECFC function [103], and was chosen based upon the results of pilot TNF time trials (data not shown). Additionally, serum content differed between these two studies. Previously, micropatterned cultures were fed with media containing only 2% serum, while we here used supplemented media totaling 10% serum. The earlier starvation conditions were motivated by a desire to slow cell division in order to keep ECs from expanding and growing over the BSA block dividing the patterned lanes. Because of the increased blocking efficacy of our polymeric blocking agent, and our desire to examine micropatterned cells at later time points, we deemed starvation

unnecessary. However, because serum starvation arrests the cell cycle, it has an additional effect of amplifying observable changes to levels of gene transcription [131]. Thus, all changes in gene expression observed here may be lower in magnitude than what would be seen under the starvation conditions used previously. Given that we observed larger micropatterning effects in KLF-2 in ECFCs than ECs in this study, we would hypothesize that starvation conditions could replicate the prior findings, and demonstrate a greater level of micropattern-driven KLF-2 expression in ECFCs than ECs.

We found no significant micropatterning-driven changes in the expression of the gene encoding von Willebrand factor (Fig 3.7). While we considered measuring vWF expression in TNF stimulated cells, the short cytokine insult period we chose to maximize VCAM-1 expression was not sufficient to produce a robust vWF response in our pilot studies (data not shown). It is possible that a vWF response could be seen coupled with a longer TNF treatment. Previous studies of the impact of fluid shear on vWF gene expression have been inconclusive. Early microarray experiments looking for flow-sensitive genes in ECs found that human umbilical vein ECs show a roughly 2-fold increase in vWF gene expression after seven days of fluid shear stress [54]. However a more recent study comparing human umbilical artery ECs, umbilical vein ECs, and ECFCs found no effect on vWF after 5 hours of fluid shear stress [132]. Interestingly, this study shows an increase in vWF expression in ECFCs compared to mature ECs after 24 hours of culture (Fig 3.7A vs. 3.7B, not evaluated statistically). While this finding might suggest an increase in basal thrombogenicity in ECFCs relative to ECs, it is important to note that our mature ECs are collected from carotid arteries, which have previously been shown to be areas of low vWF expression and production relative to other parts of the mammalian vascular tree [29,133]. Therefore, without a more anatomically diverse and representative pool of mature ECs to use as a comparison group, these results may not

be indicative of an ECFC-specific enrichment in vWF expression compared to all mature ECs.

Static micropatterning can be broadly divided into techniques based on spatial growth restriction, and those based on topography. Spatial growth restriction, as shown here, is accomplished through the iterative adsorption of extracellular matrix molecules (which promote adhesion) and hydrophobic proteins or polymers (which block cell attachment) into lanes on the order of 10-30 μm (one cell width) wide using soft lithography techniques such as microcontact printing [124] or microfluidics (as here) [80]. In contrast, topographical micropatterning generates culture substrates containing ridges and grooves with subcellular pitches on the order of 0.4 – 10 μm [84]. The results of this spatial growth restriction study support the hypothesis that ECFC micropatterning could be a beneficial feature of tissue engineered artificial vascular grafts. We chose to use a spatial growth restriction method of micropatterning for this study because of its relative methodological ease, low material cost, and its relation to our earlier body of work [80,81,107,112]. This method is a valuable tool for basic science, however it has some important limitations which would hinder its translation to clinical applications. Spatial growth restriction requires the maintenance of non-endothelialized spacer regions between lanes which would expose the underlying biomaterial and defeat the purpose of an endothelialized vascular device. Second, this technique requires the establishment of a biochemically heterogeneous surface, which would be difficult to manufacture and maintain under prolonged contact with blood and tissue. Finally, the inter-lane divisions in the current approach prevent the full engagement of EC and ECFC cadherins which allow the formation of tight junctions and trigger the contact inhibition of cell division. Thus, to translate this work to tissue engineered artificial vascular grafts, future work should focus on whole graft patterning of ECFCs, similar to what other groups have accomplished with ECs [82,84,85,134]. This approach would drive the elongation of

ECFCs in a confluent monolayer, which could result in greater durability under blood flow and a more physiologically relevant functional response.

This study also did not examine several features critical to the *in vivo* performance of ECFCs in vascular devices, including underlying pathology, substrate mechanical compliance and material thrombogenicity. We chose to study ECFCs from young, healthy primates, however there is evidence that EPCs and ECFCs function differently in patients with certain cardiovascular diseases [135]. Additionally, as described above, we chose to study spatial growth restriction on rigid polystyrene because of its relatively low cost and reproducibility. However, recent evidence suggests that matrix stiffness is associated with increased thrombogenic risk at the cellular level, necessitating attention to material mechanical properties when considering the design of novel vascular devices [136]. Substrate stiffness may have been a cause of the disruption seen to some of the VE-Cadherin junctions in Fig 4.2. Additionally, it is well known that collagen-I, which was used to promote EC and ECFC attachment in this study, is inherently thrombogenic and therefore not suitable for integration into blood-contacting devices [137]. Ongoing research into novel biomaterials with tunable mechanical properties capable of integrating less thrombogenic pro-endothelial peptide fragments such as GFPGER is addressing these issues [138]. This study provides evidence that anisotropic basal micropatterning could assist in the incorporation of ECFCs onto these and similar materials.

3.6 Conclusions

Small-diameter artificial vascular grafts remain a critical unmet need. As interest in ECFCs as a potential tool for tissue engineered grafts grows, this study supports the use of this cell type for *in vitro* device endothelialization, particularly on micropatterned

devices. These results demonstrate that ECFCs can be morphologically manipulated in the absence of fluid shear stress using spatial growth restriction micropatterning. Micropatterned ECFCs showed robust and lasting changes in gross and subcellular morphology analogous to that shown previously and repeated here with mature ECs. While the gene expression results shown here were largely unaffected by micropatterning, it should be noted that this study supports the use of ECFCs as equivalent to mature ECs in regulating neointima formation through the expression of adhesion molecules.

Chapter IV: Topographic micropatterning drives alignment but not elongation or immunoprotective gene expression changes in blood-derived endothelial colony forming cells[8]

4.1 Abstract:

Artificial small-diameter vascular grafts remain an unmet need in modern medicine. Tissue engineering techniques including in vitro endothelialization may offer potential solutions to the thrombosis and intimal hyperplasia that plague currently available synthetic devices. A potential minimally invasive source of patient autologous endothelium is ECFCs, endothelial-like outgrowth products of circulating progenitors. As anisotropic luminal topographic micropatterning gains popularity as a blood contacting device modification with the potential to flow-independently enhance the attachment, migration, gene expression, and function of mature endothelial cells, its efficacy with ECFCs remains unstudied. Here, case-matched carotid endothelial cells (CaEC) and blood-derived ECFCs are statically cultured on polyurethane substrates with micropatterned pitches (distance from peak to peak) ranging from 3 – 14 μm. On all pattern pitches tested, both CaECs and ECFCs showed significant and robust alignment to the angle of the micropatterns. Using a novel cell-by-cell image analysis algorithm, it was found that actin fibers similarly and significantly aligned to the angle of

[8] This work is in preparation for a simultaneous submission to *Biomaterials* as a primary article by Hagen, MW, and Hinds, MT.

micropatterned features on all pitches tested. Microtubules analyzed through the same novel approach showed significant alignment on most pitches examined, with a greater variation in fiber angle overall. Interestingly, only CaECs showed significant cellular elongation, and notably to a lower degree than previously seen both in vivo due to flow and with spatial growth restriction. Neither cell type displayed any significant micropattern-driven changes in the expression of KLF-2 or the downstream adhesion molecules it regulates. These results suggest that elongation, not alignment, may be the morphological factor which drives protective changes in EC and ECFC function.

4.2 Introduction:

Small diameter artificial vascular grafts remain an unmet need for substantial portions of graft-eligible patient populations for whom clinical standard autologous grafts are not an accessible option [5]. Currently available synthetic grafts lose patency through two primary mechanisms: biomaterial activation of the contact pathway, and gradual luminal narrowing driven by thickening of neointimal ingrowth into the graft. Both of these failure mechanisms are exacerbated by the regions of disturbed blood flow which are created at the end-to-side anastomoses required to deploy a vascular graft [122]. The processes underlying thrombosis and hyperplasia could be regulated by the pre-implant establishment of a functional endothelial layer through in vitro endothelialization [139].

In recent years, topographical micropatterning of luminal surfaces has emerged as a popular modification in the development of novel stents and tissue engineered vascular grafts. Anisotropic topography has been applied to biomaterial surfaces as diverse as polyurethane [84], polydimethyl siloxane [85], poly(vinyl alcohol) [134], cobalt chromium [83], titanium [86], and others in order to improve endothelial cell adhesion, direct migration, and modulate endothelial morphology and gene expression. Endothelial micropatterning describes a variety of techniques which use either spatial growth restriction or anisotropic topography to flow-independently control the alignment, elongation, migration, gene expression, and immunogenic function of endothelial cells (reviewed in [78]).

Micropatterning techniques differ significantly in methodology, mechanism of action, and effect. Spatial growth restriction micropatterning works by forcing ECs into an aligned, elongated morphology in lanes approximating the target width of the patterned cells (typically 10-30 μm), preventing contact with cells in adjacent lanes, and thereby precluding the production of a confluent endothelium. Several studies of ECs cultured

under spatial growth restriction have found whole-cell alignment and elongation comparable to ECs subjected to unidirectional fluid shear stress in vivo [79–81,140]. Quantification of EC gene expression in these systems reveals significant protective changes in the expression of key genes critical for the prevention of inflammatory responses, including upregulating the central flow-sensitive transcription factor KLF-2, and downregulating the adhesion molecule VCAM-1 [81,140]. In contrast, topographic micropatterning functions by using anisotropic features on a subcellular size scale which organize the integrins and associated focal adhesions in a fashion which drives alignment of the actin cytoskeleton and whole cell, maintaining cell-cell contacts and enabling the formation of a contiguous endothelium [141]. Studies of topographic micropatterning have consistently found, across a range of subcellular pitches on the order of 1-10 μm (features of 0.5-5 μm), substantial alignment of ECs, with some elongation, but less than that seen in vivo or in spatial growth restriction systems [82–84,142,143]. Studies of in vitro responses of ECs to anisotropic topography have largely focused on their morphology and migration, however the minority which have examined gene expression have found contradictory results. To date, no study of the effect of topography on KLF-2 expression has been published.

Despite the promise of luminal micropatterning, in vitro graft endothelialization using patient autologous endothelial cells is problematic because of the invasiveness and risk of vascular biopsy from an already hemodynamically compromised individual. However, ECFCs, the outgrowth products of circulating endothelial progenitors, are a potential solution [102,130]. ECFCs have many similarities to mature endothelial cells in morphology, gene expression, and function [103]. They have been widely studied as a tissue engineering tool, and have been demonstrated in animal models to increase graft patency when applied to a device pre-implant [106].

While ECFCs have demonstrated a similar mechanical sensitivity to fluid shear stress as mature endothelial cells [104,105], the effect of micropatterning on ECFCs has been understudied to date. Exploration of ECFC micropatterning largely stalled after one study found that the increased size and matrix remodeling ability of ECFCs relative to ECs made them difficult to pattern using spatial growth restriction with bovine serum albumin as a lane blocker [107]. It was recently demonstrated that that through a modified protocol spatial growth restriction micropatterning of ECFCs is possible, and drives elongation, whole-cell alignment, cytoskeletal alignment, and increased KLF-2 gene expression, similar to what was previously seen in micropatterned ECs [140]. To date, the effects of anisotropic topography on ECFCs has not been studied.

Here for the first time we characterize the effects of anisotropic topographies of varying pitches on the overall morphology of case-matched carotid ECs and blood-derived ECFCs. We specifically quantify the degree of whole-cell alignment and elongation, and further quantify the alignment of two major cytoskeletal components: actin and tubulin. We further measured the impact on the expression of key genes involved in immunogenic responses to fluid shear stress. We find that, as reported elsewhere, anisotropic topography drives substantial cytoskeletal and whole-cell alignment and partial elongation in carotid ECs, while it drives alignment without elongation in ECFCs. We also found, in contrast with earlier studies of spatial growth restriction micropatterning, no effect of topography on the expression of key genes.

4.3 Materials and methods:

4.3.1 Cell isolation and culture

All animal work necessary for the isolation of primary cells for this study was approved by the Oregon National Primate Research Center Institutional Care and use Committee (IP00000049). A detailed ethics statement can be found in section 2.1. Detailed descriptions of the housing, care, and humane euthanasia of these primates has been published previously [106].

This study made use of case-matched primary CaECs and ECFCs from three juvenile male *papio Anubis* baboons. Detailed descriptions of primary cell isolation and maintenance in culture can be found in section 2.2. Cells used in this study were isolated and maintained in complete endothelial medium (VascuLife VEGF kit, Lifeline Cell Technology), supplemented with FBS as described in Chapter II.

4.3.2 Micropattern preparation

The fabrication of silicon masters, PDMS submasters, and polyurethane culture substrates is described in section 2.3.2.

Polyurethane substrates for morphology studies contained either 3, 4, and 6 µm pitch patterns and planar regions or 10 and 14 µm pitch patterns and planar regions. Substrates for gene expression studies were either entirely planar or entirely 6 µm pitch.

4.3.2.1 Culture substrate validation by SEM

Polyurethane substrates were sputter coated with gold palladium alloy at 48 mA for 30 sec in 50mTorr Ar (Desk II, Denton Vacuum) before being moved to a scanning electron microscope (SEM FEI quanta 200) and imaged at 15 keV. In order to assess

feature depth, a sample of completed polyurethane-coated coverslips were cross-sectioned using a gem carbide scriber (Will Scientific) and scalpel blade to cut across a patterned region, and mounted cut-side-up for imaging. All measurements of feature sizes were made using FIJI (SciJava).

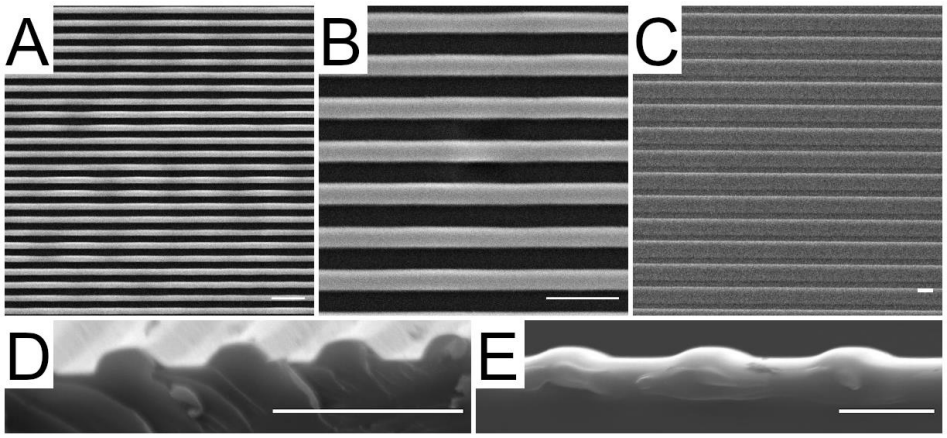

Figure 4.1: Representative images of culture substrates.
Scanning electron micrographs of culture substrates. (A) 4 µm, (B) 6 µm side view to illustrate feature height, (C) 10 µm, (D) 14 µm. Scale bars: 10 µm.

4.3.3 Micropatterning experiments

For all micropatterning studies, cured and cleaned polyurethane substrates were rinsed in PBS and coated with rat tail collagen I (50µg/mL, Corning) for at least 60 minutes, and seeded with either CaECs or ECFCs at 4.2x104 cells / cm2. Cells were cultured for either 24 or 48 hours before lysis for RNA extraction or fixation for immunofluorescence staining.

4.3.3.1Morphology studies

4.3.3.1.1 Immunofluorescence staining

A detailed staining protocol is provided in section 2.4. This study made use of primary antibodies against VE-Cadherin (Santa Cruz Biotechnology, monoclonal, clone F-8, lot 1605, 1:100) and β-tubulin (Sigma-Aldrich, monoclonal, clone TUB 2.1, lot 058M4879V, 1:500).

4.3.3.1.2 Confocal microscopy

All imaging was performed using a Zeiss LSM 880 inverted confocal microscope system. Images for quantitative morphology were collected as z-stacks with a step size of 1.31 µm using a 10X PlanApo objective NA = 0.8 and a Fast Airyscan detector array. High-resolution images were collected as z-stacks with a step size of 160 nm using a 63X PlanApo oil immersion objective NA = 1.4 and Fast Airyscan detector array. Automatic 2D airy processing was performed using Zen Black software (Zeiss) outputting 424 µm x 424 µm images with a pixel size of 101 nm x 101 nm for quantitative morphology, or 135 µm x 135 µm images with pixel size of 35 nm x 35 nm for high resolution imaging. Three images per pattern pitch per replicate were collected for quantitative morphology. For manual measurements of whole-cell morphology, and publication presentation, maximum intensity projections were produced using Zen Black software (Zeiss). Post-processing for publication was performed using FIJI (SciJava) [113].

4.3.3.1.3 Measurement of whole-cell and cytoskeletal morphology

Maximum intensity projections were given to blinded observers, who were instructed to look only at the red and green channels of all images (polyurethane can

auto fluoresce under UV light, potentially revealing pattern pitches in the DAPI channel). Using FIJI (SciJava), observers used the grid tool to throw a randomly placed grid with area per point of 15000 μm^2, and used the polygon selection tool to trace 10-16 cells per image lying on grid intersections. Section 2.5 describes the formulae used for the determination of shape index, whole cell angle deviance, and actin and tubulin angle deviance. The custom scripts developed for the automated measurement of cytoskeletal fiber angle deviance can be found in Appendix B.

4.3.3.2Gene expression studies

Gene expression studies were carried out by culturing cells as described above for 24 hours on polyurethane substrates which were either entirely planar or entirely micropatterned at 6 μm pitch. After the culture period, seeded micropatterns were moved to fresh well plates (to exclude cells which had adhered to the well plate instead of the experimental surface), rinsed with PBS (Gibco), and immediately lysed with buffer RLT (Qiagen) containing 1% β-mercaptoethanol. Following extraction, RNA was normalized to 100 ng. qPCR was carried out as described in section 2.6 using a rotor gene Q theromcycler (Qiagen). Results are reported as fold change.

4.3.4 Statistics

All studies were conducted using cells from three animals. Cells from each animal were used in two trials each, and each trial was conducted in at least duplicate, with actual replication number determined by the number of cells available at passage (N = 7-38 per unique combination of culture time, cell type, and pattern pitch for morphology studies, and N = 7-21 per unique combination of cell type and pattern pitch for gene expression). Morphology and gene expression analyses were performed such that each substrate counted as a single biological replicate. Results are reported as

mean ± SD. All statistics were calculated using R (R foundation for statistical computing, version 3.6.1 [126]). For summary statistics and hypothesis testing of cytoskeletal alignment data, mean ± SD of the by-cell normalized averages is reported. All morphology data were analyzed using linear mixed effects modeling (package nlme [144]). Fixed effects were calculated for pattern pitch (as a categorical variable), animal ID, and culture time. Random effects were calculated for sample biological ID. Where appropriate, post-hoc Tukey tests were used to identify specific differences between pattern pitches using package multcomp [128]. Gene expression data were analyzed using two-way ANOVA against patterning (planar vs. 6 μm) and cell type. Correlations between whole cell, actin, and tubulin angle deviance were calculated using linear regressions. In all cases, the suitability of parametric modeling was confirmed by examining residual vs. fitted values and normal quantile-quantile plots of fitted models.

4.4 Results:

4.4.1 Whole cell morphology

Qualitative examination of micrographs of CaECs stained for VE-Cadherin show a noticeable alignment and subtle elongation when cells are cultured on anisotropic topographies relative to those cultured on planar surfaces (Figure 4.2A, A1.1A). In contrast, the difference between ECFCs cultured with or without substrate micropatterning is difficult to discern visually (Figure 4.2B, A1.1B).

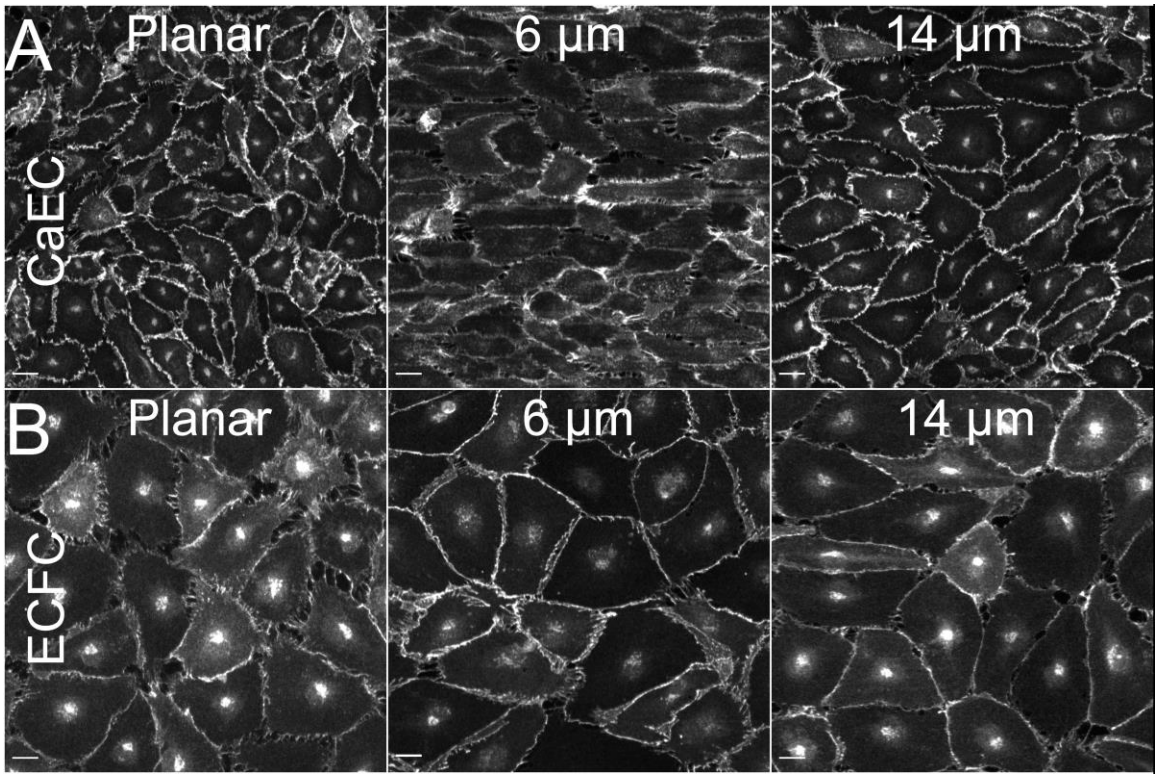

Figure 4.2: Whole cell alignment and elongation.
Topographical micropatterning drives significant alignment in CaECs and ECFCs, but elongation only in CaECs. VE-Cadherin staining in CaECs (A) and ECFCs (B) on (left to right) planar substrates, and micropatterned substrates with 6 µm and 14 µm pattern pitches after 24 hours. Scale bars 20 µm. All micrographs are oriented so that pattern features are horizontal.

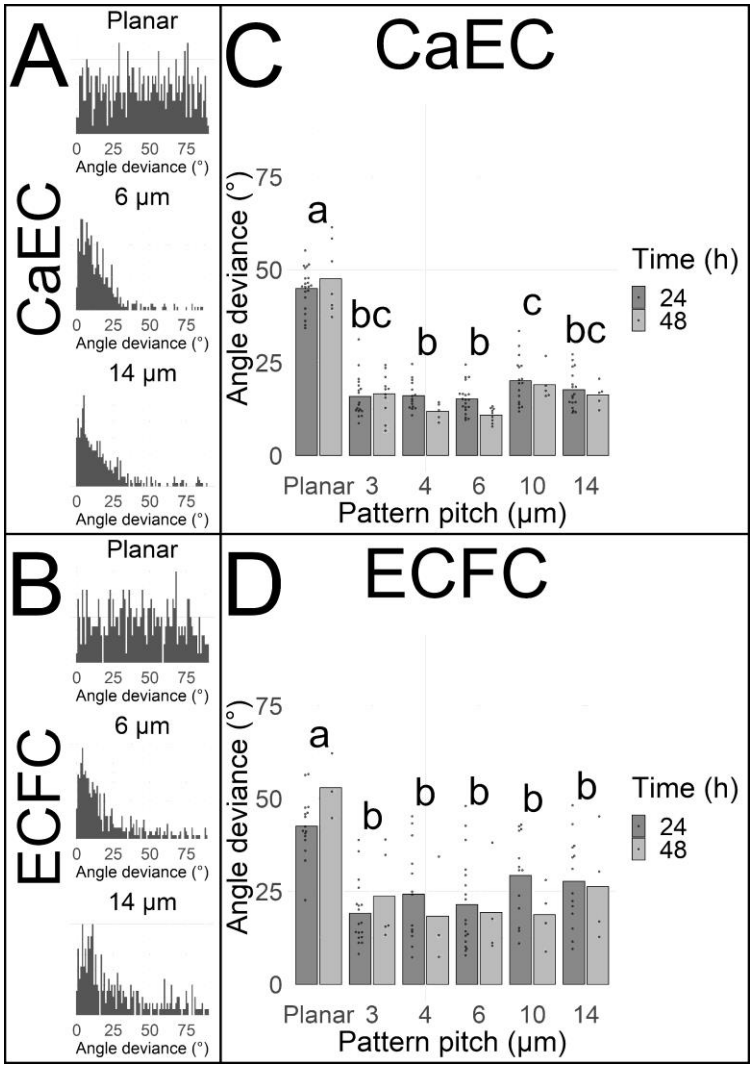

Figure 4.3: Quantification of whole cell alignment.

CaECs and ECFCs showed significant alignment to micropatterns in all pitches tested. (A-B) Histograms summarizing the distribution of angle deviances in CaECs (A) and ECFCs (B) on each pattern pitch. (C-D) quantification of whole-cell alignment in CaECs (C) and ECFCs (D) showing mean (bars) and biological replicate mean (dots) whole cell angle deviance from pattern. Pitch groups sharing letters are not statistically different according to post-hoc Tukey test.

4.4.1.1 Quantification of whole cell alignment

The alignment of whole cells was determined by measuring the angle deviance between traced cell major axes and the angle of micropatterned features. Both CaECs and ECFCs cultured on planar surfaces showed a random distribution of orientations at both time points tested, with mean angle deviances of 45±6° and 43±5°, respectively, at 24 hours, and 48±10° and 53±9°, respectively, at 48 hours (Figure 4.3A,C). In both cell types at both time points tested the distribution of cell alignment skewed left on all of the topographies (Figure 4.3A,B), with CaECs on 6 µm pitch patterns showing average deviances of 15±4° after 24 hours and 11±2° after 48 hours. ECFCs on 6 µm pitch patterns showed a similar although less robust reduction in deviance to 21±12° after 24 hours and 19±13° after 48 hours. Significant effects of pattern pitch but not culture time were found across all conditions tested (Figure 4.3C, CaEC LME pattern pitch $p = 0.0001$, time $p = 0.28$, Figure 4.3D, ECFC, LME pattern pitch $p < 0.0001$, time $p = 0.59$). For both cell types, post-hoc Tukey tests showed that cells cultured on all pattern pitches differed statistically from those cultured on planar substrates.

4.4.1.2 Quantification of cell elongation

The elongation of whole cells was determined by calculating the shape index of manually traced cells. CaECs cultured on planar substrates showed a cobblestone morphology with average SI of 0.63±0.06 at 24 hours and 0.61±0.03 at 48 hours. These cells showed statistically significant, although only moderate elongation when cultured on anisotropic topographies, with average shape indices of 0.52±0.07 after 24 hours and 0.54±0.04 after 48 hours on 6 µm pitch substrates (Figure 4.4A,C, LME pattern pitch $p < 0.0001$, time $p = 0.14$). Post-hoc Tukey test confirms that all micropatterned CaEC SIs were statistically different from planar.

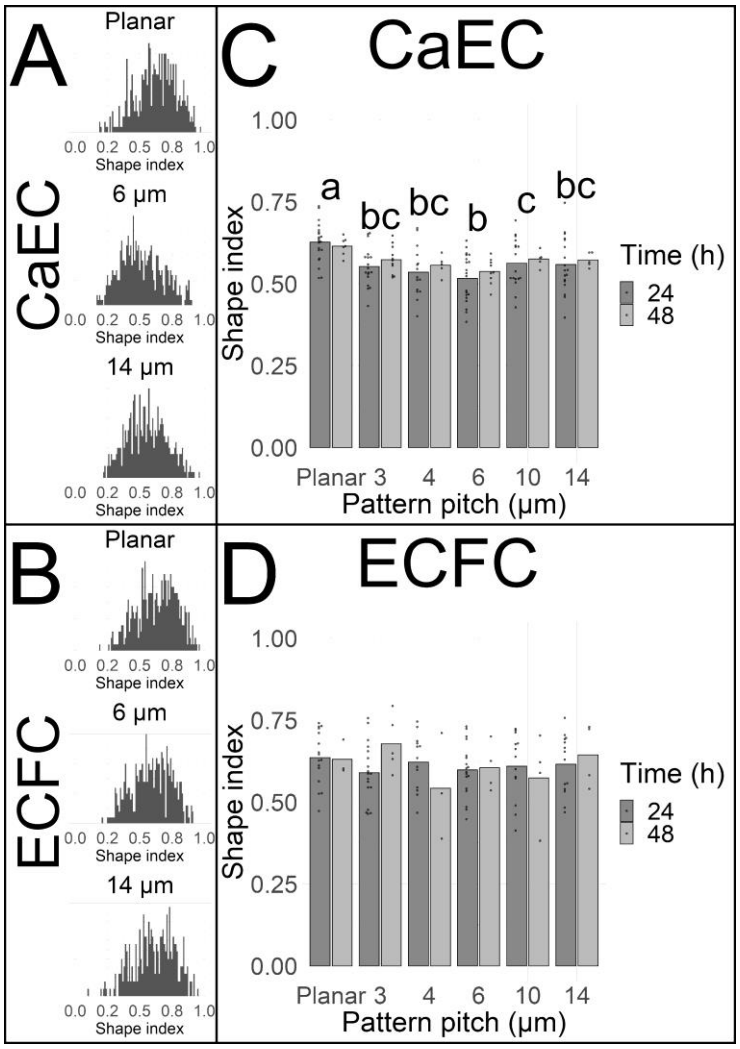

Figure 4.4: Quantification of whole cell elongation.

CaECs showed moderate, but statistically significant elongation in response to micropatterning across all pitches tested, while ECFCs showed no significant differences. (A-B) Histograms summarizing the distribution of shape indices on CaECs (A) and ECFCs (B). (C-D) quantification of whole-cell elongation in CaECs (C) and ECFCs (D) showing mean (bars) and biological replicate average (dots) whole cell shape index. Pitch groups sharing letters are not significantly different according to post-hoc Tukey test ($p > 0.05$). Tukey test was not performed for ECFCs (D) because LME showed no significant micropatterning effect.

ECFCs cultured on planar substrates showed similarly rounded morphologies, with average SIs of 0.64±0.08 after 24 hours and 0.63±0.05 after 48 hours. However in contrast to CaECs, ECFCs showed no significant elongation when cultured on micropatterned surfaces, with average 6 μm pitch SIs of 0.60±0.08 after 24 hours and 0.61±0.07 after 48 hours (Figure 4.4B,D, LME pattern pitch $p = 0.43$, time $p = 0.66$).

4.4.2 Cytoskeletal actin alignment

Qualitative examination of both CaECs and ECFCs stained for actin showed notable alignment when cells were cultured on topographically micropatterned surfaces. The formation of visibly dense actin stress fibers was most prominent in cells cultured on patterns with pitches of 10 or 14 μm (Figure 4.5A,B, A1.3A,B) relative to cells cultured on planar, 3 μm, 4 μm, or 6 μm pitch substrates.

The distribution of actin fiber orientation was random when both CaECs and ECFCs were cultured on planar substrates, with CaEC fibers showing average normalized deviances of 47±11° after 24 hours and 46±13° after 48 hours, and ECFC fibers showing 53±7° after 24 hours and 45±9° after 48 hours. CaEC actin fibers largely aligned when micropatterned, showing average deviances of 19±18° after 24 hours on 6 μm substrates and 19±10° after 48 hours (Figure 4.5C LME pitch $p < 0.0001$, time $p = 0.26$), with post-hoc testing confirming that all micropatterned CaEC actin is significantly more aligned than planar. The actin fibers in ECFCs were also significantly aligned, although to a lesser degree, with average normalized angle deviances of 29±15° after 24 hours and 20±19° after 48 hours of culture on micropatterned substrates with a 6 μm pitch (Figure 4.5D LME pitch $p < 0.0001$, time $p = 0.011$). As with CaECs, post hoc testing showed that all micropatterned ECFC actin is significantly more aligned than planar.

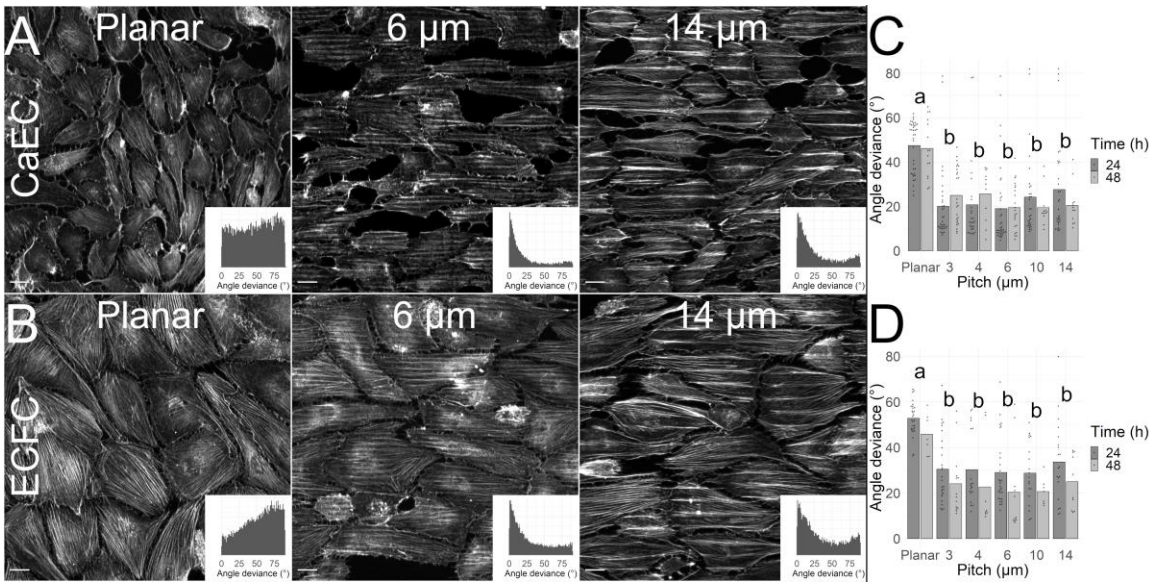

Figure 4.5: Actin alignment.

Topographical micropatterning drives alignment of the actin cytoskeleton. (A-B) Phalloidin stained CaECs (A) and ECFCs (B) on (left to right) planar, 6 µm pitch patterned, 14 µm pitch patterned substrates after 24 hours. Scale bars are 20 µm. All images are oriented so that patterned angle is horizontal. Inset panels show raw distribution of angle deviances. (C-D) quantification of actin alignment in CaECs (C) and ECFCs (D) showing overall mean (bars) and biological replicate mean normalized by-cell averages (dots). Pitch groups sharing letters are not statistically different by post-hoc Tukey test ($p > 0.05$).

4.4.3 Cytoskeletal tubulin alignment

Imaging of tubulin fibers showed considerable alignment in both cell types when cells were cultured on topographically micropatterned surfaces (Figure 4.6A,B, A1.4A,B). As with actin, the distribution of tubulin fiber orientation was random when cells were cultured on planar surfaces, with CaECs showing average normalized angle deviances of 41±10° after 24 hours and 46±11° after 48 hours and ECFCs similarly showing 46±6° after both 24 and 48 hours. CaEC tubulin fibers were statistically significantly aligned when micropatterned, although to a smaller degree than seen with actin, with CaECs on

6 µm patterned substrates showing average normalized angle deviances of 26±18° after 24 hours and 27±10° after 48 hours (Figure 4.6C, LME pattern pitch $p < 0.0001$, time $p = 0.47$) with post hoc Tukey tests showing that that all patterned tubulin fibers were statistically different from planar, except for 4 µm. ECFC tubulin fibers were also significantly aligned, with those on 6 µm patterns exhibiting average normalized angle deviances of 32±15° after 24 hours and 29±15° after 48 hours (Figure 4.6D, LME pattern pitch $p < 0.0001$, time $p = 0.056$) and post hoc Tukey tests showing statistical differences between planar and all patterned pitches except for 14 µm.

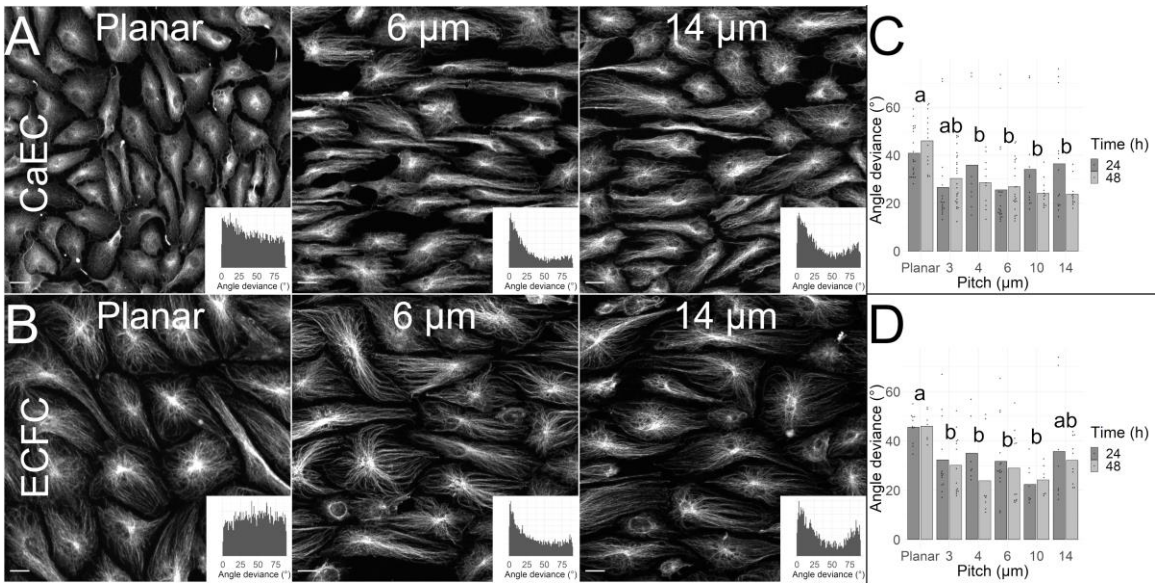

Figure 4.6: Tubulin alignment.

Topographical micropatterning drives alignment of the microtubule cytoskeleton. (A-B) β-tubulin staining of CaECs (A) and ECFCs (B) on (left to right) planar, 6 µm pitch patterned, and 14 µm pitch patterned substrates after 24 hours. Scale bars are 20 µm. All micrographs are oriented so that features are horizontal. Inset panels show raw distribution of measured tubulin fibers. (C-D) quantification of tubulin alignment in CaECs (C) and ECFCs (D) showing mean (bars) and biological replicate mean (dots) normalized by-cell angle deviances. Pitch groups sharing letters are not statistically different by post-hoc Tukey test ($p > 0.05$).

4.4.4 Relationship between morphological metrics

Examination of high-resolution imaging of CaECs and ECFCs which are co-stained for actin and tubulin show that the fibers do not typically co-align when cultured on planar substrates, however they appear to align to similar degrees when cultured on anisotropic topographies (Figure 4.7A-D). There were no significant relationships between whole cell alignment and elongation on CaECs or ECFCs cultured on planar substrates (Figure 4.8A; R^2 = 0.001, 0.002 respectively; p = 0.75, 0.14 respectively). There were significant, but weak relationships between SI and whole cell alignment among micropatterned CaECs and ECFCs however (Figure 4.8A; R^2 = 0.067, 0.101 respectively; $p < 0.0001$ both). When examining the relationship between whole-cell alignment and actin alignment, a consistently weak but significant relationship was found across the cell types and patterning conditions tested (Figure 4.8C; planar CaECs R^2 = 0.102, patterned CaECs R^2 = 0.010, planar ECFCs R^2 = 0.121, patterned ECFCs R^2 = 0.165, $p < 0.0001$ all). Interestingly, there was no significant relationship between tubulin and whole-cell alignment, expect with micropatterned ECFCs, where the relationship remains weak (Figure 4.8D; patterned ECFCs R^2 = 0.045, $p < 0.0001$, all others $R^2 <$ 0.001, $p > 0.39$). There was however a strong relationship between the average actin and tubulin angle deviances across conditions (Figure 4.8B; planar CaEC R^2 = 0.77, patterned CaEC R^2 = 0.700, planar ECFC R^2 = 0.810, patterned ECFC R2 = 0.783, $p <$ 0.0001 all).

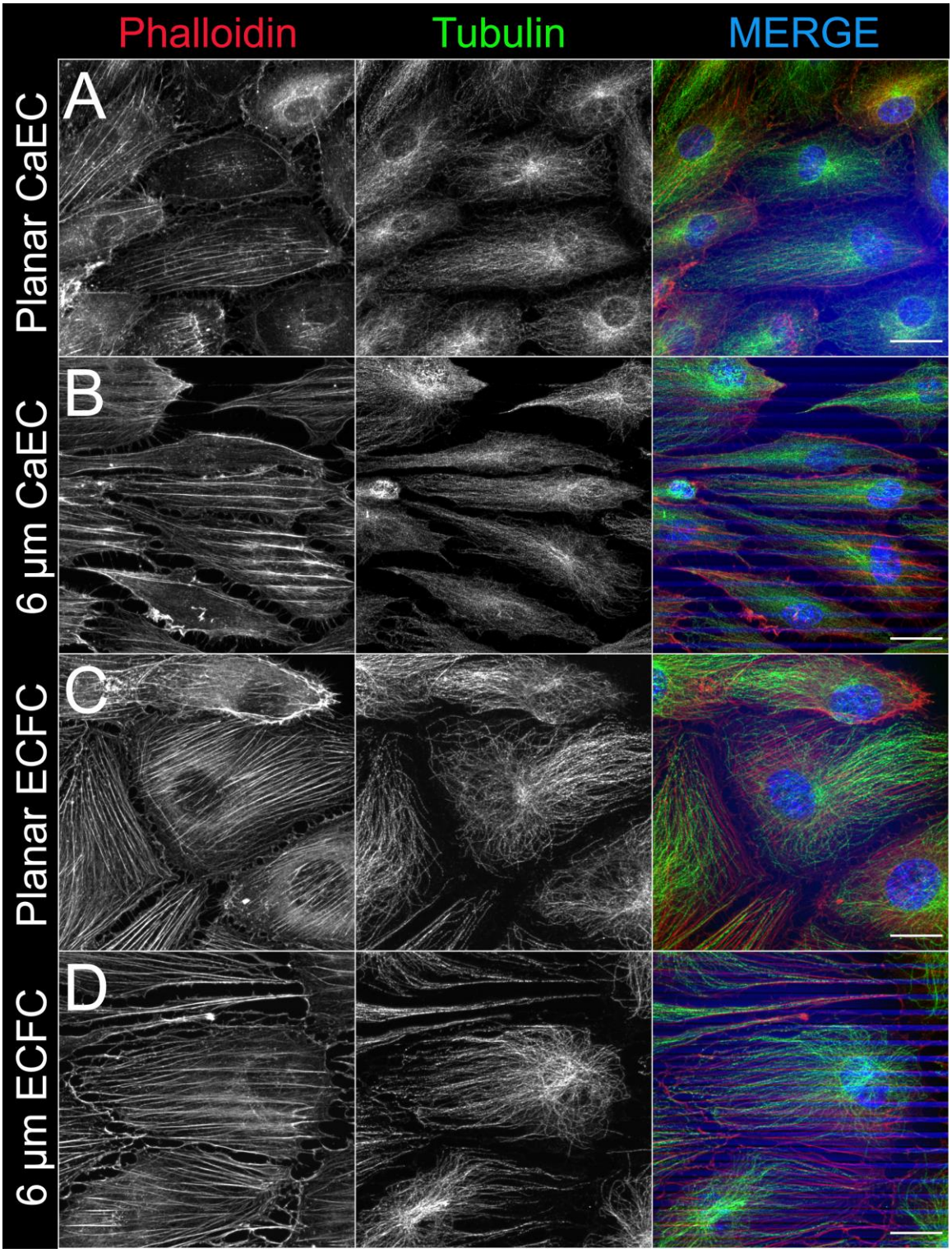
Phalloidin
Tubulin
MERGE
A
Planar CaEC
B
6 µm CaEC
C
Planar ECFC
D
6 µm ECFC

Figure 4.7: high-magnification representative imaging of cytoskeletal components.

Representative 63X magnification imaging to show relationship between cytoskeletal actin and tubulin. Left: Phalloidin staining of actin; Center: anti-β-Tubulin staining, Right: Merge with actin in red, tubulin in green, and DAPI-stained cell nuclei in blue. Note that polyurethane micropatterns tend to autofluoresce in the blue channel. (A) Planar CaEC. (B) 6 µm micropatterned CaECs. (C) Planar ECFCs. (D) 6 µm micropatterned ECFCs. Scale bars are 20 µm.

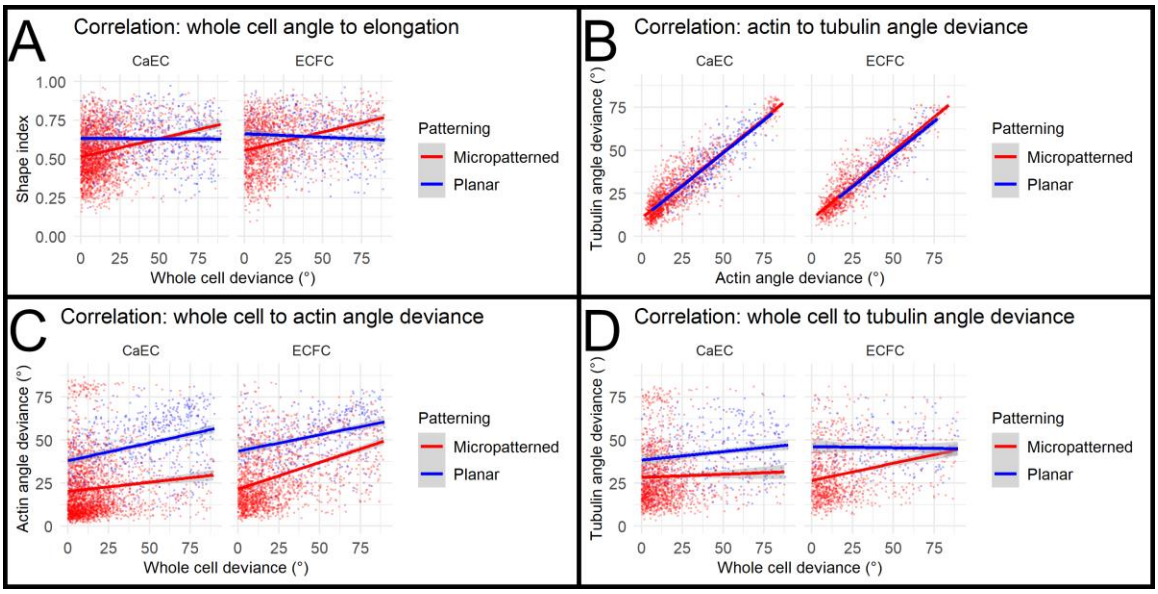

Figure 4.8: relationship between morphological metrics.

There are weak relationships between whole-cell measures of morphology and a strong relationship between actin and microtubule alignment. All panels: red: micropatterned, blue: planar; left CeECs, right ECFCs. (A) relationship between whole-cell alignment and elongation. (B) Relationship between actin and tubulin. (C) Relationship between actin and whole-cell alignment. (D) relationship between tubulin and whole-cell alignment.

4.4.5 Gene expression

The expression of key genes was assessed using real time quantitative PCR. There was no effect of either cell type or culture substrate on the expression of the transcription factor KLF-2 (Figure 4.9A; ANOVA cell type p = 0.87, patterning p = 0.89).

The adhesion molecule VCAM-1 similarly showed no response to micropatterning, however did show a remarkably lower level of expression in ECFCs than mature CaECs (Figure 4.9B; ANOVA cell type $p < 0.0001$, patterning $p = 0.94$). The adhesion molecule E-Selectin likewise showed relatively lower expression in ECFCs than CaECs, but also no effect of micropatterning (Figure 4.9C; ANOVA cell type $p = 0.005$, patterning $p = 0.69$).

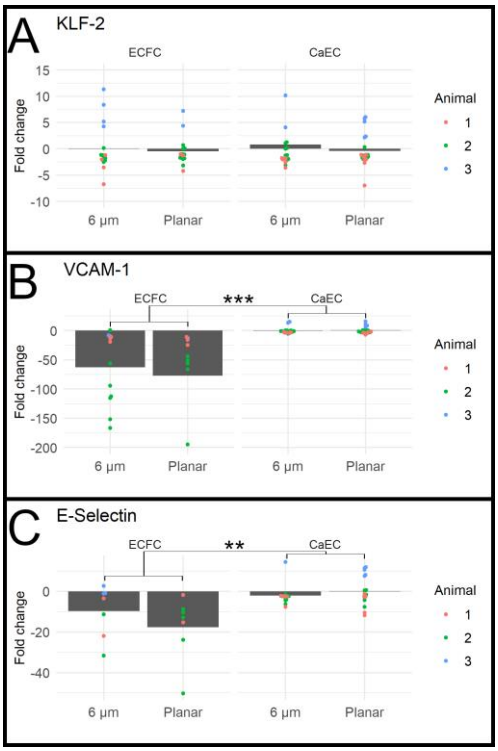

Figure 4.9: Impact of cell type and substrate micropatterning on expression of key genes.

Micropatterning did not affect the expressions of key flow-regulated genes. All values are fold change relative to planar CaECs. (A) KLF-2 gene expression showed no significant effect of micropatterning or cell type. (B) VCAM-1 gene expression showed no significant effect of micropatterning, however ECFCs showed a statistically significant lower baseline expression level than CaECs. (C) E-Selectin gene expression likewise had no significant response to micropatterning, however did show a significant basal decrease in expression relative to CaECs.

4.5 Discussion:

This study tested two hypotheses: first that the morphology of blood-derived ECFCs can be modified by anisotropic topography as had previously been shown for mature ECs, and second that the gene expression profile of both ECs and ECFCs can be modified by static topographical micropatterning as has previously been shown with growth restriction micropatterning. This work did confirm the effectiveness of topography as a tool for driving alignment on whole-cell and cytoskeletal scales for both cell types, yet we found only limited elongation of CaECs, no significant elongation of ECFCs, and no impact of topographic micropatterning on inflammatory gene expression in either cell type.

4.5.1 Anisotropic topography significantly aligns both the cell bodies and cytoskeletal components of CaECs and ECFCs

The most robust effects of anisotropic topography found in this study were on the whole-cell alignment of both CaECs and ECFCs. All of the pattern pitches tested induced significant and substantial reductions in the average angle of deviance between the patterns and cells relative to cells cultured on planar surfaces for both cell types at both time points (Figure 4.3C,D). This result confirms for the first time the hypothesis that ECFC morphology can be modulated using basal topography, and confirms earlier work demonstrating the alignment of mature ECs on patterned polyurethane surfaces [82,84,141].

The design of this study was based largely on work showing that mature ECs exhibit progressively greater alignment on topographic patterns with pitches increasing from 0.4 μm to 4 μm [82]. Here, CaECs and ECFCs were studied on pattern pitches

ranging from 3 to 14 μm. These pitches were selected in part to identify the pattern pitch with greatest effect on morphology for each cell type. Interestingly, there was no discernible difference between the alignments seen across these pattern pitches, suggesting that all pitches in this range are similarly effective as modulators of EC and ECFC alignment.

In addition to assessing whole-cell morphology, the alignment of the specific cytoskeletal components actin and tubulin were assessed using a novel computational approach. The approach used here allowed the cell-by-cell analysis of actin and tubulin alignment by incorporating the blinded manual cell tracings as regions of interest. This had two distinct benefits over an aggregate approach: the ability to normalize by fiber length, and the ability to compare the behavior of cytoskeletal elements with whole-cell elements of morphology. The development of this quantitative strategy was inspired by earlier methods which used radon transformations of images following Laplacian edge detection to estimate the average orientation of fibrillar elements [80,81,107], and those using the very well established automated image thresholding and particle tracing to count and analyze visibly discrete elements, which are built into most modern image analysis software [113,145]. The image quality and resolution offered by the Airyscan platform used here made a method based in particle analysis feasible. The arguable drawback of the cell-by-cell approach is the elimination of the non-traced regions of imaged cultures from analyses of cytoskeletal alignment. In order to validate the cell-by-cell analysis, a similar algorithm which measured fiber angles across entire images without cell-by-cell subsetting was developed in parallel. This method found aggregate results which reflected those found in the cell-by-cell method and can be found in Figures A1.5 and A1.6.

The dynamic reorganization of actin fibers has been widely characterized in ECs exposed to unidirectional fluid shear stress [146,147], and the alignment of both fibers

has been demonstrated in spatially growth restricted ECs [80]. Both cytoskeletal components demonstrated significant alignment in most patterns tested (Figures 4.5, 4.6). As was seen on the whole-cell scale, no statistically significant differences were identified between pitches, however mean trends suggest that both actin and tubulin may show greater alignment on 6 and 10 μm pattern pitches than the other pitch patterns tested here.

4.5.2 Topographic micropatterning does not elongate ECFCs

In addition to quantifying the alignment of ECs and ECFCs to topographical micropatterns, the effect of patterning on cell elongation was also assessed. Increased elongation, as quantified by an increased cell aspect ratio or decreased shape index, is a hallmark of exposure to unidirectional fluid shear stress in mature ECs *in vivo*, *in vitro*, and of ECFCs in vitro [104,105,148]. Furthermore, substantial elongation of both cell types has been demonstrated with spatial growth restriction micropatterning [81,140]. A statistically significant effect of topography on CaEC elongation was identified here (Figure 4.4C). However, no changes on shape index were seen in ECFCs, (Figure 4.4D). This result highlights a first major difference between the effects of topographic micropatterning and spatial growth restriction micropatterning.

While micropatterning-driven CaEC elongation was demonstrated here, it is notable that the degree of elongation observed was far weaker than that seen with either spatial growth restriction or shear-induced elongation. Earlier studies of growth restriction showed CaEC SIs of below 0.4 after 24-48 hours [80,140], while here CaECs exhibited mean SIs between 0.52 and 0.57 (equivalent to aspect ratios between 2.7-3.3, Figure A1.2). Importantly, this is in agreement with previously published accounts of

mature EC topographic micropatterning. One study statically culturing human aortic ECs on polyurethane micropatterns similar to those used here for an unspecified period of time found an aspect ratio of about 3.3 with a 4 μm pitch [82], while another study of culturing HUVECs on cobalt-chromium substrates consistently found aspect ratios of just under 3.0 after 12 hours of serum-free culture on pitches of 3, 10, and 20 μm [83]. Endothelial elongation under unidirectional flow in major arteries in vivo induces shape indices of between 0.34 and 0.36 [52]. Taken together, this analysis of topographically patterned cell morphology suggests that anisotropic topography can substantially align both ECs and ECFCs at the whole-cell and cytoskeletal levels, however its effect on elongation is weak.

4.5.3 Topographic micropatterning has no effect on immunogenic gene expression

One of the primary benefits of unidirectional fluid shear stress on overall endothelial physiology in vivo is thought to be its downstream effects attenuating immunogenicity and thrombogenicity. This benefit, largely regulated by the transcription factor KLF-2 [56] has been shown to exist in spatially growth restricted ECs [81] and ECFCs [140]. To date to our knowledge, the effect of topographical micropatterning on KLF-2 expression has not been characterized. Earlier studies have quantified the effect of topography on several of the downstream adhesion molecules and functions KLF-2 regulates, with contradictory results. One study examining EA926 human ECs on rigid silicon and titanium surfaces found steadily decreasing VCAM-1 gene expression as pattern pitch was increased from 1-100 μm [86]. Another study examining human coronary ECs on collagen-coated PDMS similarly found that micropatterned ECs

exhibited reduced VCAM-1 and ICAM-1 expression than cells on planar surfaces, but that they displayed increased monocyte attachment [85].

Given the ultimate goal of designing micropatterned devices which could withstand the harmful effects of disturbed perianastomotic fluid shear stress, it was deemed pertinent to, for the first time, examine the effects of topographic micropatterning on KLF-2, in addition to its downstream targets. Surprisingly, no effect of anisotropic topography was identified on the expression of KLF-2, VCAM-1, or E-Selectin (Figure 4.9). Supplementary experiments using low-serum media confirmed that micropatterning effects were not masked by cell cycle variations [131] (data not shown). This result marks the second major difference between spatial growth restriction and topographical micropatterning.

There were notable and statistically significant decreases in both VCAM-1 and E-Selectin seen in ECFCs relative to their case-matched CaECs basally (Figure 4.6B,C). This finding is novel, however does not necessarily contradict earlier work which found non-significant trends toward decreased expression levels of both genes in ECFCs compared to CaECs also taken from *Papio anubis* baboons [103]. Also notable is the wider variance in expression levels seen in ECFCs relative to CaECs here, perhaps a result of their progenitor state.

4.5.4 Changes in gene regulation may depend on cell elongation rather than alignment

The goal of micropatterning technology is to flow-independently replicate the beneficial effects of the unidirectional fluid shear stress that ECs experience in vivo. It is therefore useful to consider the responses of endothelial cells to three distinct stimuli: unidirectional fluid shear stress, spatial growth restriction micropatterning, and

topographical micropatterning. In static culture in vitro and in regions of disturbed flow in vivo, ECs exhibit a rounded, cobblestone shape, random alignment, and a disorganized actin cytoskeleton with a dense peripheral band. Upon exposure to unidirectional fluid shear stress, ECs align parallel to flow, elongate, and form visible cytoplasmic actin stress fibers [53]. In response to static spatial growth restriction micropatterning, ECs align and elongate to an extent similar to that seen under flow. Their actin cytoskeleton does align, however the dense peripheral band remains and stress fibers are not visible [80]. Finally, as seen here and in similar studies [82,84], ECs statically cultured on topographical micropatterns align to the patterns, show only moderate elongation, and do display the formation of actin stress fibers, which form along topographical pattern ridges.

The in vivo mechanism of fluid shear stress mechanotransduction remains poorly understood. The current understanding identifies a variety of putative mechanotransducers, however cannot identify any one of these as the initial or lynchpin connection between fluid shear stress and KLF-2 upregulation [69]. Two potential sites of mechanotransduction with relevance to micropatterning are the junctional PECAM-1, VEGFR2, VE-Cadherin complex and basal integrins. In spatial growth restriction micropatterning, which creates lanes approximately one cell wide, the engagement of junctional constituents is obviously limited [80]. It is possible, though unlikely, that this limitation is partially responsible for the immunoprotective effects of spatial growth restriction. Multiple studies establishing the centrality of PECAM-1 to the flow-driven eNOS response showed that PECAM-1 knockdown or knockout result in increased basal eNOS activity, and a reversal of the fluid shear stress-eNOS relationship [70,149], suggesting that the role of PECAM-1 could be inhibitory. If this were the case, then the disruption of EC junctional complex formation in spatial growth restriction

micropatterning could partially explain the efficacy of that approach at decreasing atherogenicity.

A more likely site of micropatterning-driven mechanotransduction is in the relationship between basal integrins and the cytoskeleton, via focal adhesion kinases and the Rho-A pathway. While it is known that integrins can mechanotransduce, the fluid shear stress felt by the basal surface of the endothelial cell is orders of magnitude lower than that experienced at the luminal surface, making more likely the hypothesis that stress is translated to integrins through the cytoskeleton [74,75]. Earlier work characterizing the subcellular organization of HUVECs in the first hours after seeding onto polyurethane substrates revealed rapid localization of integrin-associated focal adhesion kinases to pattern ridges along with alignment of the actin cytoskeleton [141]. We had hypothesized that these organizing effects would be sufficient to trigger the downstream signaling cascades which affect KLF-2 expression, however our results do not support this. Rather it may be the case that the specific stresses resulting from an overall elongation of cell shape are required to trigger changes in gene expression.

In order to gain a fuller understanding of the relationship between elements of endothelial morphology which are affected by flow and patterning, a novel cell-by-cell image analysis system was used. Interestingly, there was not strong evidence for connections between elongation and alignment, or between the alignment of whole cells and their cytoskeletal components. There was however strong evidence toward a relationship between the actin and tubulin components within each cell (Figure 4.8). The apparent relationship between actin and tubulin alignment in the micropatterned cells studied here is notable because microtubule polymerization has previously been found to be necessary for micropatterning-driven endothelial elongation and changes in KLF-2 gene expression [80,81]. That strong tubulin alignment, and a strong actin-tubulin relationship were seen in this study suggests the relationship between morphology and

gene expression has more to do with the distribution of stresses within the cell than the specific organization of the tubulin cytoskeleton.

The present findings that CaECs show only limited elongation in response to topographical micropatterning, that ECFCs show no elongation to topographical micropatterning, and that neither cell type shows a gene expression response to topographical micropatterning highlight the lack of attention given to the distinction between endothelial alignment and elongation in much of the micropatterning literature. While many studies do dutifully quantify and report endothelial aspect ratio, inverse aspect ratio, or shape index [80–83,143,150], others use less robust methods of quantification. A number of published reports combine alignment and elongation, reporting a percentage of cells “elongated and aligned”. For example, two studies quantifying early and late responses of ECs to patterning on polyurethane surfaces used the reasonable alignment cutoff of ± 10° from patterned angle, and the surprisingly low elongation cutoff of aspect ratio greater than or equal to 1.3, a condition notably met by 90% of the cells cultured on planar surfaces in this study (Figure A1.1) [84,141]. Many others rely on either qualitative descriptions of representative imaging, or worse yet report “percent elongated” with no detailed methods describing their quantification [142,151,152]. As it becomes clearer that the morphological correlate to KLF-2 expression and immuno- and thromboprotection in ECs and ECFCs may be alignment with elongation, greater care should be taken in future publications to quantify elongation.

4.5.5 Study limitations and next steps

While under the static conditions studied here, topographical micropatterning did not attenuate immunogenic signaling, these results do not preclude the notion that microtopography could be a beneficial feature in a tissue engineered vascular graft. This

study looked only at topographical patterns with a depth of 1 µm. Earlier studies of endothelial topographical micropatterning have shown that feature depth could be a predictor of morphological and functional efficacy. One study examining cobalt-chromium micropatterning toward the design of an *in situ* endothelializable stent found that HUVECs responded by aligning and (slightly) elongating on surfaces with feature depths greater than 0.6 µm, but showed minimal changes on feature depths of less than 40 nm [83]. The 1 µm pattern depths used in this study are equal to or slightly greater than those used in many published reports of topographical endothelial micropatterning [82–84,141,142]. However, several other studies have examined slightly greater depths. For instance, Vandrangi and colleagues examined the elongation of human EA926 ECs on rigid substrates with groove depths of 1.3 µm and found cell aspect ratios exceeding 5 on 1 µm pitch titanium substrates [86]. Several studies have manufactured patterns with 2 µm depths, however did not quantify endothelial elongation [85,153]. Notably however, one of these did find decreased VCAM-1 expression in micropatterned human coronary artery ECs [85]. While these results suggest that deeper pattern ridge depths may drive greater elongation or functional effects, these studies also used different endothelial subtypes and materials with different stiffness than those reported on here, thus a systematic study of topographical pattern depth may be called for.

This study also looked only at endothelial responses in static culture. While the absence of flow is arguably itself an injury model, driving the cobblestone morphologies and low KLF-2 expression seen in atheroprone regions in vivo, it would also be informative to study the combined effects of topography and flow. Future studies should quantify the shape index and gene expression of topographically micropatterned ECs and ECFCs under both unidirectional and reversing fluid shear stress regimes, in order to address whether the gross and cytoskeletal alignment seen in response to topographical patterning can either prime cells to respond more readily to beneficial

unidirectional fluid shear, or ameliorate the uniquely harmful effects of oscillatory shear. A number of studies examining the competitive effects of micropatterning and unidirectional perpendicular shear stress have demonstrated that mature ECs maintain their patterned alignment in spite of exposure to perpendicular shear [82,154]. To date the only study to examine the effects of oscillatory shear stress on micropatterned ECs found that parallel oscillating shear triggered increased eNOS phosphorylation, while static patterned ECs and those exposed to perpendicular oscillating shear maintained equivalent levels of phosphorylation, suggesting that oscillating shear parallel to a pre-aligned cell's axis is beneficial. However, this study only examined cell behavior for the first 3-4 hours of shear because of limited adhesion on their 5 μm-wide fibronectin / pluronics patterns [155]. Further study of the competitive and possibly synergistic effects of flow and micropatterning on both ECs and ECFCs is warranted.

Finally, it should be noted that microtopography has other demonstrated beneficial effects on endothelial cells, including increased adhesion and migration, both of which would be vital features in an *in vitro* or *in situ* endothelializable graft. ECs from multiple vascular beds have been found to migrate at a significantly higher rate when cultured on anisotropically patterned polyurethane with pitches of 1.2 μm or 4 μm relative to planar or isotropically patterned polyurethane. Furthermore, cells on the wider-pitched surfaces migrated in the direction of patterning, while migration was random on planar substrates [84]. However, a similar study of human aortic ECs on planar versus 4 μm pitch polyurethane found that when exposed to perpendicular flow, the direction of migration was random, suggesting that the benefit of patterning on directional migration might be limited in certain settings with disturbed flow [82].

4.5.6 Conclusions:

This study demonstrated for the first time that ECFCs, like mature ECs, exhibit both gross and cytoskeletal alignment in response to anisotropic topographical micropatterning with pitches between 3-14 μm. It also demonstrated a critical and previously unidentified difference between CaECs and ECFCs: that the former shows a weak but present elongating response to topography, while the latter shows no overall elongation. Finally, this study was the first to examine the effects of topographic patterning on the expression of key genes by ECFCs involved in immunogenic regulation, and demonstrated that no such effect exists. Taken together, these results suggest that endothelial elongation, rather than simple alignment, maybe necessary to trigger immunoprotective changes in gene expression.

Chapter V: Thrombogenicity of flow diverters in an *ex vivo* shunt model: effect of phosphorylcholine surface modification[9]

5.1 Abstract

Background and Purpose: Flow diverters offer a promising treatment for cerebral aneurysms. However they have associated thromboembolic risks, mandating chronic dual antiplatelet therapy (DAPT). Shield Technology™ is a phosphorylcholine surface modification of the Pipeline™ Embolization Device (PED) flow diverter which has shown significant reductions in material thrombogenicity *in vitro*. The current study compares the thrombogenicity of PED, PED with Shield Technology™ (PED+Shield), and the Flow-Redirection Endoluminal Device (FRED™) – with and without single and dual antiplatelet therapy – under physiological flow.

Methods: An established non-human primate *ex vivo* arteriovenous shunt model of stent thrombosis was used. PED, PED+Shield, and FRED™ were tested without antiplatelet therapy, with ASA monotherapy, and with DAPT. Radiolabeled platelet deposition was quantified over one hour for each device and total fibrin deposition was also quantified.

Results: Cumulative statistical analysis revealed significantly lower platelet deposition on PED compared to FRED™. The same statistical model revealed

[9] This research was originally published in *Journal of neurointerventional surgery*. Hagen MW, Girdhar G, Wainwright J, Hinds MT. Thrombogenicity of flow diverters in an ex vivo shunt model: effect of phosphorylcholine surface modification. *Journal of neurointerventional surgery.* 2017; 9:1006-1011. © The authors.

significant decreases in platelet deposition driven by the use of either ASA, clopidogrel, or Shield Technology™. Direct comparisons of device performances within antiplatelet conditions showed consistent significant decreases in platelet accumulation on PED+Shield relative to FRED™. PED+Shield showed significant reductions in platelet deposition compared to unmodified PED without antiplatelet therapy and with DAPT. PED accumulated minimal fibrin with and without Shield Technology™.

Conclusions: In this pre-clinical model, we have shown that Shield Technology™ phosphorylcholine modification reduces the platelet-specific thrombogenicity of a flow diverter under physiologically relevant flow with and without DAPT. We have further identified increased fibrin-driven thrombogenicity associated with FRED™ relative to PED.

5.2 Introduction

Coiling and stent assisted coiling have been the gold standard for the endovascular treatment of cerebral aneurysms [156]. Flow diversion devices represent a recent and significant paradigm shift in the treatment of these vascular anomalies [157,158]. Unlike intrasaccular devices, flow diverters consist of a highly porous metal stent deployed in the parent artery covering the aneurysm neck in order to divert blood flow away from the aneurysm - thereby driving the gradual thrombosis and healing of the aneurysm sac over time. Due to the approximately 30% metal coverage of the vessel wall, these devices also provide a scaffold for endothelialization across the aneurysm neck [157]. Currently the only flow diversion device with FDA approval is the Pipeline™ Embolization Device (PED). However other devices including the Flow-Redirection Endoluminal Device (FRED™) are available in Europe and in US clinical trials. Numerous clinical studies and case reports have demonstrated the effectiveness of PED[159–161] and FRED™ [162,163], respectively, in aneurysm treatment. In this study, we compared a dual layered flow diverter (FRED™) with single layer diverters (PED and PED with Shield Technology™) to understand the contribution of flow mediated thrombogenicity.

There is thromboembolic risk associated with the use of coiling [164], stent assisted coiling [165], and flow diverters [166,167]. The use of endoluminal devices including flow diverters mandates perioperative systemic heparinization and dual antiplatelet therapy (DAPT: acetylsalicylic acid (ASA) with clopidogrel) before, and for at least three months following device deployment, with some patients requiring at least one antiplatelet therapy for life. In addition to generally increasing the risk of bleeding, this level of anticoagulation limits the effective acute use of flow diverters for ruptured aneurysms [157]. Another limitation is that clopidogrel metabolism is dependent on the

activity of the cytochrome P450 CYP2C19. Common polymorphisms affecting CYP2C19 activity result in widely variable effects of clopidogrel on platelet activity across populations, potentially reducing antiplatelet effect in some cases [168].

To improve hemocompatibility there is an interest in the development of thromboresistant flow diverters. Phosphorylcholine is a major component of the erythrocyte outer cell membrane and has demonstrated efficacy in resisting platelet adhesion [169] and intimal hyperplasia [170] on arterial grafts. Medtronic, Inc. has developed a novel phosphorylcholine surface modification known as Shield Technology™ that is 3 nm thick and is covalently bound to the PED braid. *In vitro* studies of PED with Shield Technology™ have shown dramatic reductions in material thrombogenicity as indicated by reduced thrombin generation under static conditions [171]. However, the thrombogenicity of Shield Technology™ under physiological flow conditions in the absence of systemic anticoagulants and in the presence of antiplatelet therapies remains unknown.

The current study uses a well-established non-human primate *ex vivo* arteriovenous shunt model [172] to quantify the relative thrombogenicity of three flow diversion devices: PED, PED with Shield Technology™ (PED+Shield), and FRED™. Devices were tested without antiplatelet therapy, with ASA alone, and with DAPT (ASA with clopidogrel). Thrombogenicity was assessed by quantification of radiolabeled platelets over time and total fibrin deposition on devices.

5.3 Materials & methods:

5.3.1 Devices

All devices tested were sterilized final products. The following flow diversion devices were tested: (a) Pipeline™ Flex Embolization Device (PED, N=9, 5 mm × 35 mm, Medtronic); (b) Pipeline™ Flex Embolization Device with Shield Technology™ (PED+Shield, N=9, 5 mm × 35 mm, Medtronic); (c) Flow-Redirection Endoluminal Device (FRED™, N=8, 5 mm × 36 mm, Microvention). Devices were deployed in silastic medical grade tubing (3.98 mm ID, Technical Products, Inc.).

5.3.2 Arteriovenous shunt studies

Survival studies were conducted using a single male juvenile baboon (*Papio anubis*). A detailed ethics statement can be found in section 2.1. All experiments described here were approved by our Institutional Animal Care and Use Committee according to guidelines of the NIH “Guide for the Care and Use of Laboratory Animals” prepared by the Committee on Care & Use of Laboratory Animals of the Institute of Laboratory Animal Resources, National Research Council (International Standard Book, Number 0-309-05377-3, 1996).

Arteriovenous shunt placement and studies were carried out as described in section 2.7 with test flow diverter devices deployed within lengths of silicone tubing, as illustrated in Figure 5.1. Real-time quantification of platelet deposition is illustrated in Figure 5.3. With the exception of FRED™ with DAPT (which was run in duplicate), all unique drug and device combinations were run in triplicate.

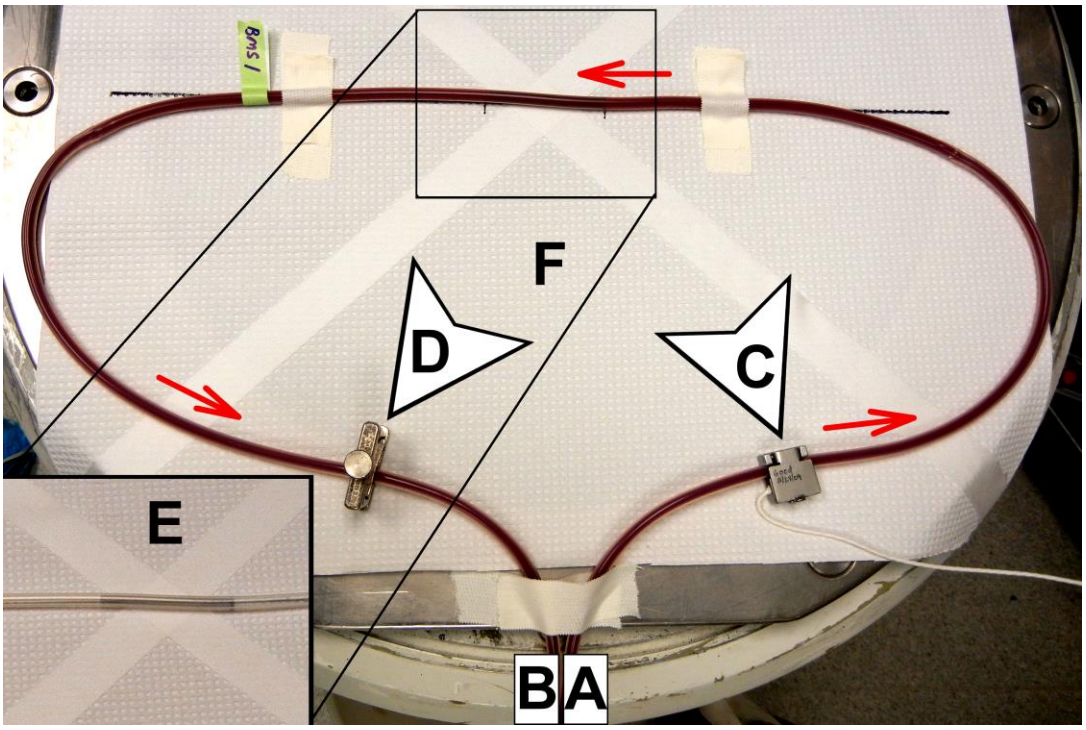

Figure 5.1: *Ex vivo* shunt loop setup

Representative photograph of arteriovenous ex vivo shunt loop during study. (A) Blood flows from the baboon femoral artery and through the shunt loop counter-clockwise illustrated by red arrows). (B) Blood is returned to the femoral vein. (C) Blood flow is monitored using an ultrasonic flow probe proximal to the test device. (D) Blood flow is regulated using a manual clamp distal to the test device. (E inset) Test device position within shunt loop. (F) The shunt loop sits above a gamma camera which records the deposition of 111In-labeled platelets on the test device.

5.3.3 Antiplatelet drug dosing and aggregometry response

Three conditions were tested in this study: DAPT (ASA with clopidogrel), ASA alone, and no antiplatelet. For ASA and DAPT trials, ASA (Bayer Healthcare, LLC) was given orally at 10 mg/kg at least four hours prior to the experiment start time. Clopidogrel (Torrent Pharmaceuticals, Ltd.) was given orally at 2 mg/kg twice before each DAPT study: the afternoon before and morning-of at least three hours before experiments

began. Prior studies performed in this model have proven this antiplatelet regimen effective over the duration studied here [110]. More than one month passed between ASA or DAPT trials and the resumption of antiplatelet-free trials, while at least seven days passed between DAPT and ASA monotherapy trials [110]. Evaluation of antiplatelet drug efficacy was carried out using LTPA, described in section 2.7.

5.3.4 Statistical methods

Statistical calculations were performed using R (R Core Team). Platelet deposition data were log-transformed prior to analysis to approximate the normal distribution for parametric testing. In order to incorporate all of the time series data, platelet deposition analyses were performed using repeated measures ANOVA (RMA). A cumulative statistical model took PED without antiplatelet therapy as its baseline and calculated coefficients defining the effects of (1) FRED™, (2) ASA and / or (3) clopidogrel, and (4) modification with Shield Technology™. Clopidogrel effects were determined using this statistical model and were not separately measured. Subset RMAs were generated for each antiplatelet group (no antiplatelet, ASA, DAPT). All p-values reported for platelet deposition were Bonferroni-corrected to compensate for using each datum in two models. Direct comparisons between conditions within subset analyses were performed using linear combination t-tests with an additional Bonferroni correction for multiple comparisons. Platelet aggregometry data were analyzed using a two-way RMA (on drug presence versus absence and aggregation time). Fibrin data were analyzed within antiplatelet drug groups using a one-way ANOVA on device. Direct comparisons of fibrin data were performed using the Dunnett test taking unmodified PED as a reference. All reported values are mean plus or minus one standard deviation (sd) at 60 min. Significance was defined as $p=0.05$ or less.

5.4 Results

5.4.1 Antiplatelet therapy was effective in study subject

Light transmission platelet aggregometry was used to confirm the inhibitory effects of ASA and clopidogrel on platelet receptors for AA and ADP, respectively. Aggregometric traces in the absence of ASA treatment showed a full response to AA (Figure 5.2A), while traces generated following either ASA monotherapy or DAPT yielded a total abolition of that response (Figure 5.2B). Quantification of percent aggregometry at 90s and 180s after AA addition revealed a significant difference between ASA groups (Figure 5.2C; $p=0.012$). Likewise, traces generated in the absence of clopidogrel showed a full response to 80 µM ADP (Figure 5.2D), while those generated following DAPT showed a total loss of the aggregative phase of the curve (Figure 5.2E). Quantification of percent aggregometry at 90s and 180s following ADP addition confirmed a significant difference between clopidogrel groups (Figure 5.2F; $p=0.002$). Thus the animal was a normal responder to both ASA and clopidogrel, and an appropriate experimental subject for this study.

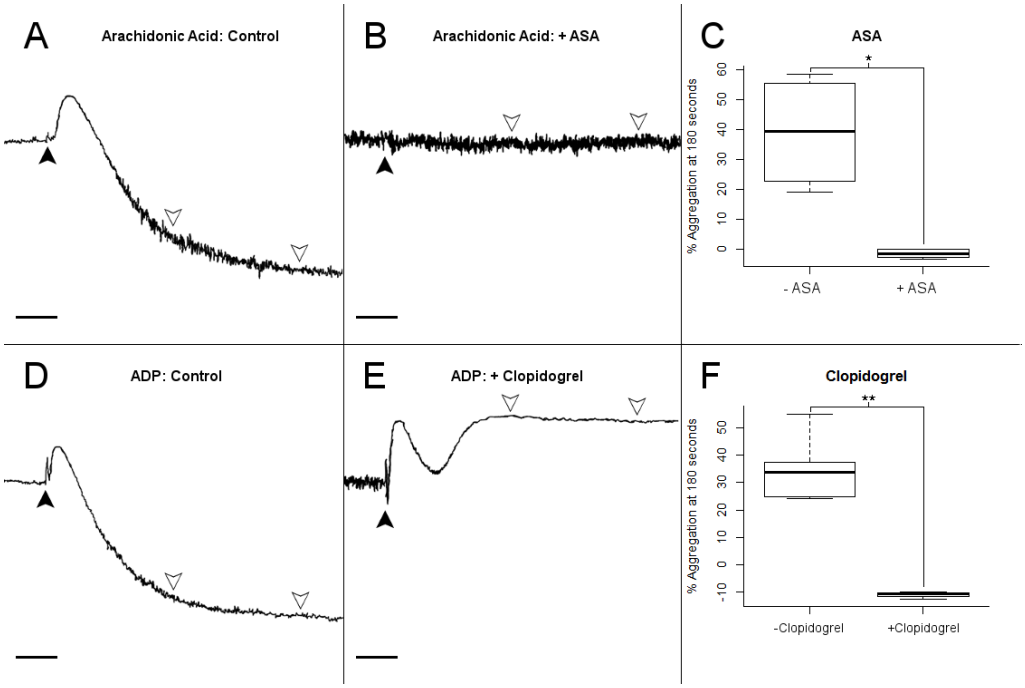

Figure 5.2: Platelet aggregometry

Light transmission platelet aggregometry was used to confirm the antiplatelet effects of ASA (A-C) and Clopidogrel (D-F). (A) In the absence of ASA, 613 µmol/L AA induces platelet aggregation, as shown by the drop in light absorption. (B) Following ASA therapy, AA induces no response in platelets. (C) 180 seconds after agonist addition ASA has a statistically significant effect on platelet aggregation in response to AA ($p = 0.012$ *). (D) In the absence of clopidogrel, ADP induces platelet aggregation. (E) Following clopidogrel therapy, the aggregative portion of the ADP response curve is abolished. (F) Clopidogrel has a statistically significant effect on platelet aggregation in response to ADP ($p = 0.002$ **). In panels A, B, D and E, black arrows mark the time of agonist addition to PRP. Open inverted arrows mark the 90 and 180 second timepoints used for quantification. Scale bars: 30 seconds.

5.4.2 Platelet deposition onto FRED™ devices is increased in the absence of clopidogrel

Without antiplatelet therapy, subset analysis shows an increase in platelet deposition on FRED™ relative to PED falling just short of statistical significance (Table 5.1, Figure 5.3D; p=0.084; PED: 5.8±2.1×10^9 platelets; FRED™: 9.31±3.9×10^9 platelets). Notably, the single total device occlusion in this study occurred in a FRED™ without antiplatelet trial at 57 minutes. With ASA monotherapy there was a significant increase in platelet deposition seen on FRED™ (Figure 5.3E; p=0.022; PED: 1.6±1.1×10^9 platelets; FRED™: 5.74±0.13×10^9 platelets). However, no platelet deposition difference was seen between PED and FRED™ under DAPT (Figure 5.3F; p=1.0; PED: 0.46±0.1×10^9 platelets; FRED™: 0.64±0.06×10^9 platelets). Thus, while statistical significance was only achieved in ASA trials, FRED™ trends toward greater platelet accumulation in the absence of clopidogrel.

5.4.3 Shield Technology™ decreased platelet deposition across drug conditions

Without antiplatelet therapy, subset analysis associates Shield Technology™ with a significant reduction in platelets deposited (Figure 5.3D; p=0.016; PED: 5.8±2.1×10^9 platelets; PED+Shield: 2.0±2.0×10^9 platelets). Under ASA monotherapy, the difference between PED with and without Shield Technology™ fell just short of significance (Figure 5.3E; p=0.084; PED: 1.6±1.1×10^9 platelets; PED+Shield: 0.52±0.26×10^9 platelets). However, under DAPT a significant reduction was attributable to Shield Technology™ (Figure 5.3F; p<0.001; PED: 0.46±0.1×10^9 platelets; PED+Shield: 0.15±0.08×10^9 platelets). The Shield Technology™ surface modification of PED provides a consistent reduction in platelet deposition across drug conditions,

however the magnitude of this effect is variable, as indicated by our failure to achieve statistical significance with ASA monotherapy.

Table 5.1: Summary of platelet deposition statistical analyses.

The comprehensive analysis calculates specific effect sizes for FRED, Shield Technology, ASA, and Clopidogrel using unmodified PED without antiplatelet therapy as a reference. Subset analyses are direct comparisons between devices (FRED, PED, PED+Sheild) within each antiplatelet therapy (no antiplatelet, ASA alone, DAPT). * denotes $p < 0.05$; *** denotes $p < 0.001$.

Comparison	Effect (platelets $\times 10^9$)	Test statistic	p-value	
Comprehensive analysis vs. PED alone				
FRED™	+2.01	F=34.99	1.4×10^{-5}	***
Shield Technology™	-2.44	F=17.32	8.1×10^{-4}	***
ASA	-1.87	F=23.95	1.9×10^{-5}	***
Clopidogrel	-2.41	F=33.62	4.8×10^{-4}	***
Subset: No antiplatelet				
FRED™ vs PED	2.32	t=2.20	0.084	
FRED™ vs PED+Shield	6.73	t=4.99	1.8×10^{-6}	***
PED vs PED+Shield	2.9	t=2.79	0.016	*
Subset: ASA alone				
FRED™ vs PED	2.92	t=2.68	0.022	*
FRED™ vs PED+Shield	7.04	t=4.88	3.2×10^{-6}	***
PED vs PED+Shield	2.41	t=2.20	0.084	
Subset: DAPT				
FRED™ vs PED	-1.01	t=-0.08	1.00	
FRED™ vs PED+Shield	1.46	t=4.59	1.4×10^{-5}	***
PED vs PED+Shield	2.07	t=4.89	3.0×10^{-6}	***

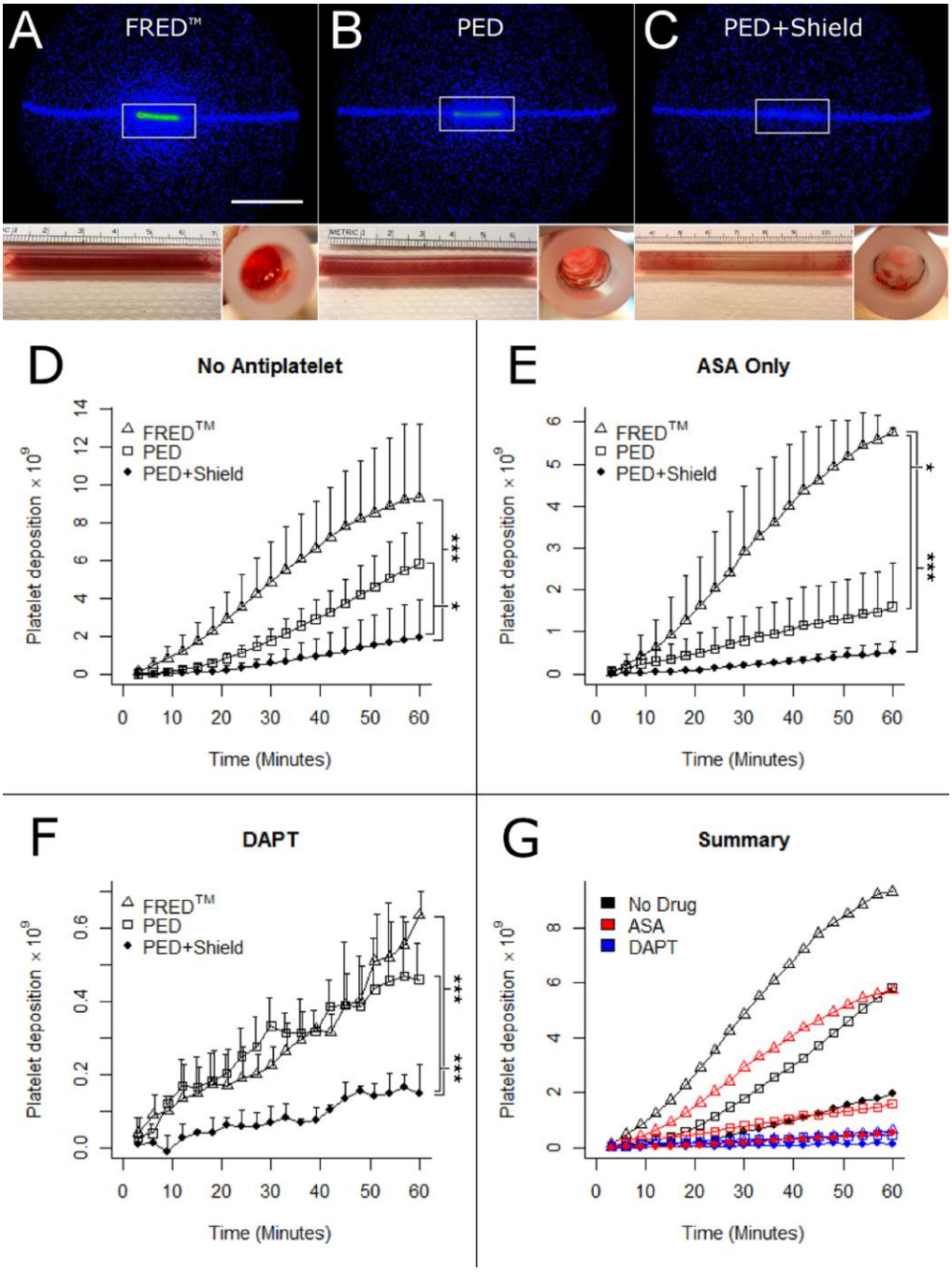
A
FRED™
B
PED
C
PED+Shield
D
No Antiplatelet
E
ASA Only
F
DAPT
G
Summary
FRED™
PED
PED+Shield
No Drug
ASA
DAPT
Platelet deposition × 10^9
Time (Minutes)
***
*

Figure 5.3: Representative scintillography and photographs with quantification of platelet deposition

(A-C) Representative scintillography and photographs from no-antiplatelet trials. (A) FRED™; (B) PED; (C) PED+Shield. Main panels: gamma camera output at 60 minutes. Scale bar: 10cm. White boxes show region used for signal quantification. Insets: photographs of devices inside silicone tubing at the conclusion of arteriovenous shunt studies. Insets: (left) longitudinal and (right) distal end-on photographs of devices at the end of shunt studies. (D-G) Summary of platelet deposition data from all trials. In panels D-F, symbols represent means and error bars represent +sd. (D) In the absence of antiplatelet therapy, PED+Shield devices showed a significant decrease in platelet deposition relative to PED ($p=0.016$*) and FRED™ ($p<0.001$***). (E) Following ASA monotherapy, FRED™ devices experienced significantly more platelet deposition than either PED ($p=0.022$*) or PED+Shield ($p<0.001$***). (F) Under dual antiplatelet therapy PED+Shield devices experienced significantly less platelet deposition than PED ($p<0.001$***) or FRED™ (p***<0.001) which were statistically indistinguishable ($p=1.0$). (G) Summary of all three antiplatelet therapy conditions. Error bars have been removed for visual clarity.

5.4.4 Cumulative analysis reveals significant thromboresistance by Shield Technology™

All platelet deposition data were analyzed together using bare PED without antiplatelet therapy, which had $5.8\pm2.1\times10^9$ platelets attached at 60 min as a reference. Specific effect sizes on platelet attachment were calculated for ASA, clopidogrel, FRED™, and Shield Technology™. ASA treatment was associated with a reduction of $1.87\pm1.2\times10^9$ platelets ($p<0.001$) while clopidogrel treatment and presence of Shield Technology™ on PED were associated with reductions of $2.41\pm1.3\times10^9$ and $2.44\pm1.2\times10^9$ platelets, respectively (both: $p<0.001$). In contrast, FRED™ was associated with an increase of $2.01\pm1.25\times10^9$ platelets ($p<0.001$). Thus, the use of ASA, clopidogrel, and Shield Technology™ individually each showed statistically significant thromboresistant effects compared to PED alone (Figure 5.4).

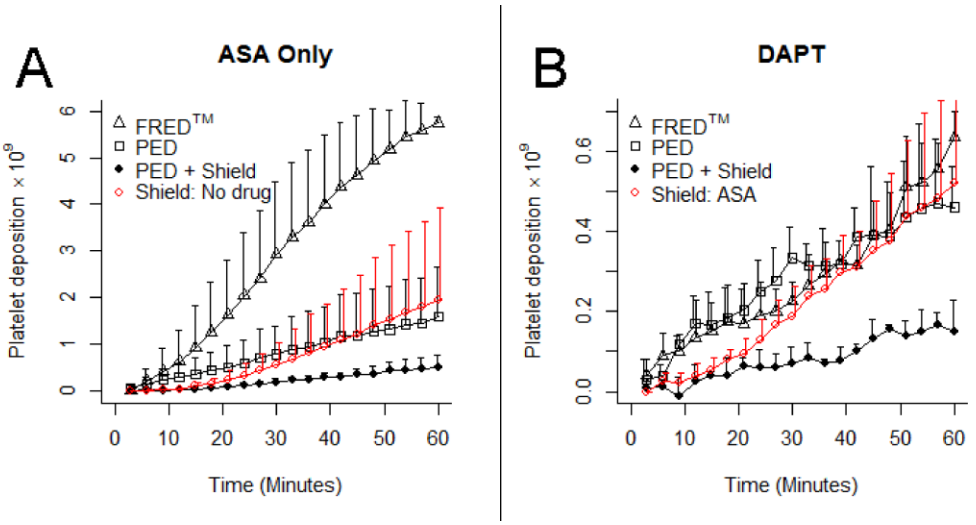

Figure 5.4: Specific effectiveness of Shield Technology™

Summary of Shield Technology™ performance with reduced antiplatelet therapy compared to other device classes. (A) Platelet deposition onto Shield devices without any antiplatelet therapy (red) is compared with all devices under ASA monotherapy (black). (B) Shield with ASA monotherapy (red) is compared with all devices under dual antiplatelet therapy (black). Shield Technology™, ASA, and clopidogrel were each associated with significant antiplatelet effects in our cumulative analysis of all platelet deposition trials.

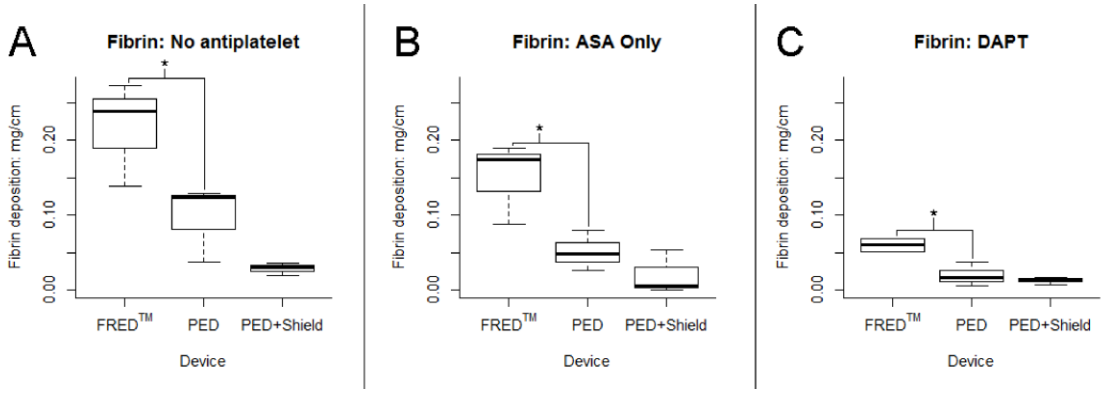

Figure 5.5: Fibrin deposition

Across all drug conditions tested, FRED™ devices showed significantly greater fibrin accumulation than PED. Shield Technology™ did not have a significant impact on fibrin deposition relative to unmodified PED. (A) In the absence of antiplatelet therapy, FRED™ showed significantly greater fibrin deposition than PED (p=0.045*). (B) Under ASA monotherapy, FRED™ showed significantly greater fibrin accumulation than PED (p=0.038*). (C) Likewise, under DAPT, FRED™ showed significantly greater fibrin accumulation than PED (p=0.023*).

5.4.5 FRED™ accrues significantly more fibrin than PED

Following platelet deposition studies, total fibrin deposition on each device was quantified. FRED™ use was associated with an increase in fibrin deposition across all antiplatelet conditions. Without antiplatelet drugs, the amount of fibrin on FRED™ is more than double that seen on PED (Figure 5.5A; p=0.045; PED: 0.097±0.051 mg/cm fibrin, FRED™: 2.17±0.069 mg/cm fibrin). Under ASA monotherapy a similarly significant difference is seen between FRED™ and PED (Figure 5.5B; p=0.038; PED: 0.051±0.027 mg/cm fibrin, FRED™: 0.15±0.055 mg/cm fibrin), with similar results seen under DAPT (Figure 5.5C; p=0.023; PED: 0.020±0.016 mg/cm fibrin, FRED™: 0.06±0.013 mg/cm fibrin). In summary, fibrin accumulation is a significantly and consistently higher on FRED™ than PED.

Shield Technology™ was associated with a small and statistically insignificant fibrin decrease relative to bare PED without antiplatelet therapy (Figure 5.5A; p=0.240; PED: 0.097±0.051 mg/cm fibrin, PED+Shield: 0.028±0.008 mg/cm fibrin). Under ASA monotherapy and DAPT, Shield Technology™ use was likewise associated with small and statistically insignificant decreases in total fibrin (Figure 5.5B, C; ASA: p=0.553; PED: 0.051±0.027 mg/cm fibrin, PED+Shield: 0.020±0.030 mg/cm fibrin; DAPT: p=0.700; PED: 0.020±0.016 mg/cm fibrin, PED+Shield: 0.013±0.005 mg/cm fibrin). Moderate fibrin decreases were seen with Shield Technology™ use, however none were statistically significant.

5.5 Discussion

5.5.1 The baboon arteriovenous shunt model of stent thrombosis

This study uses a well-established baboon *ex vivo* arteriovenous shunt model of stent thrombosis. While previous *in vitro* work has succeeded in identifying the effects of Shield Technology™ on material thrombogenicity [171], understanding this technology's performance in the complex environment of flowing blood is a necessary step toward better understanding its ability to resist thrombosis in a clinical setting. Our *ex vivo* minimally invasive technique can safely be used without systemic anticoagulants [106]. Additionally, the *ex vivo* shunt studies allow for consistent device deployment, identical flow conditions, and are performed in the same animal for 1:1 comparisons. Furthermore, this model, which measures activated platelet and fibrin adhesion on devices as an indication of thrombogenicity, was the basis of much of the preclinical work which established DAPT as the drug regimen used for arterial graft patients today [110], allowing direct comparisons with the present study.

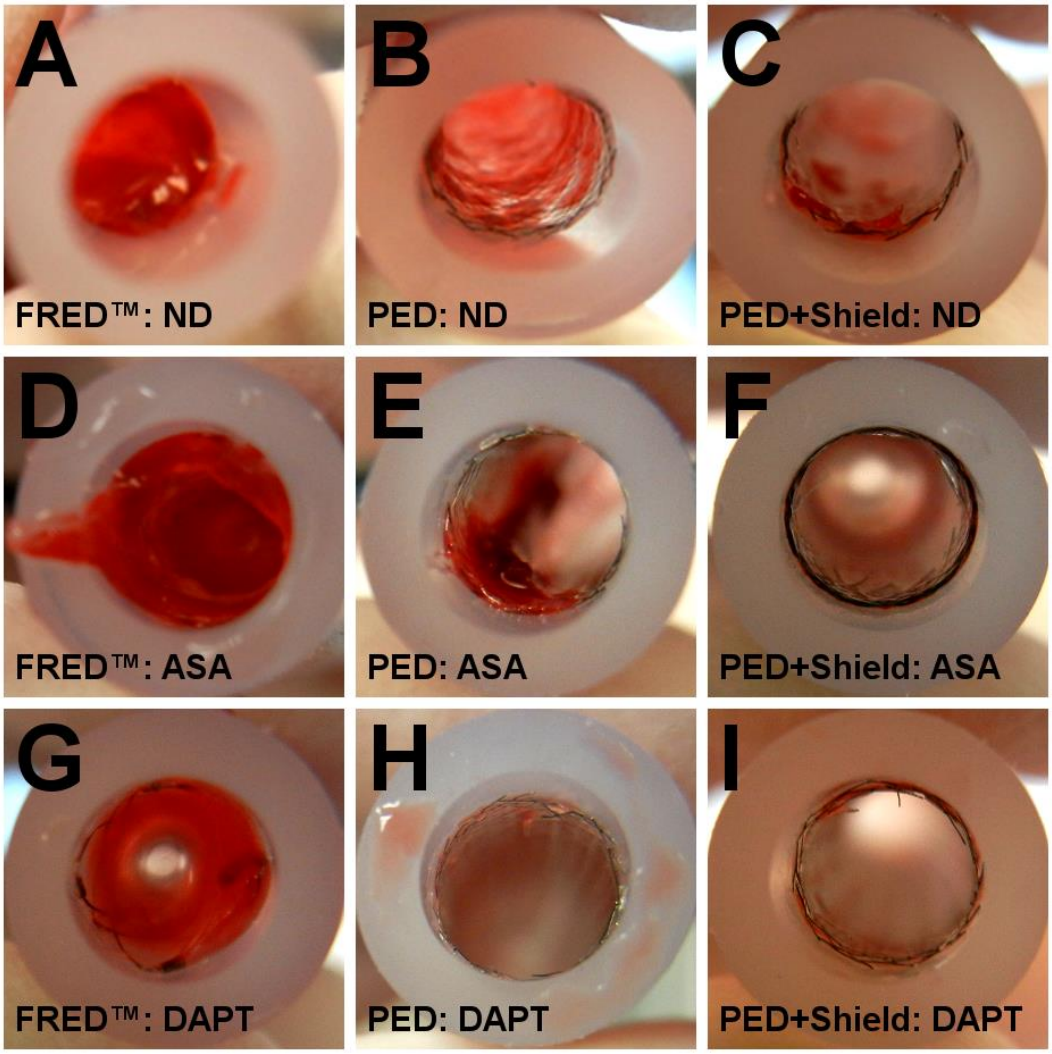

Figure 5.6: Device thrombus photographs

Devices were photographed at the conclusion of arteriovenous shunt studies. All images collected here are taken from the distal end looking into the device proximally. (A-C) are images of (A) FRED™, (B) PED, and (C) PED+Shield without antiplatelet treatment and are repeated from Figure 6.3. (D-F) show (D) FRED™, (E) PED, and (F) PED+Shield with ASA monotherapy. (G-I) show (G) FRED™, (H) PED, and (I) PED+Shield with DAPT.

5.5.2 FRED™ devices accrue platelets and fibrin at a higher rate than PED with Shield Technology™

Fibrin accumulation was found to be greater on FRED™ than unmodified PED devices across antiplatelet conditions, and our cumulative analysis of platelet deposition data found that FRED™ use was associated with a similarly significant increase in platelet attachment. Notably however, in subset analyses the difference between FRED™ and unmodified PED only reached statistical significance under ASA monotherapy, and the devices performed equivalently under DAPT (Table 5.1).

The PED is a single-layer cobalt-chromium braid providing approximately 30% surface coverage with platinum wires incorporated for radiopacity. In contrast, FRED™ is a dual layer Nitinol device consisting of a low porosity inner braid attached to a high porosity outer braid with a double helix of radiopaque tantalum wires [167]. The material thrombogenicities of PED and FRED™ were previously shown to be equivalent in a static measurement of thrombin generation [171], therefore the differences in thrombogenicity observed here are likely flow-related. This may be potentially attributable to the structure of FRED™, as the dual layered design may lead to localized disturbed flow conditions, which could entrap activated platelets causing a nidus for thrombus formation.

5.5.3 Shield Technology™ has a significant platelet-specific thromboresistant effect

In this study, the effective thromboresistance of Shield Technology™, a phosphorylcholine surface modification mimicking the erythrocyte outer membrane, was demonstrated. PED with Shield Technology™ was shown to resist in-stent thrombosis caused by the deposition of activated platelets on the surfaces of bare Pipeline™

devices. ASA, clopidogrel, and Shield Technology™, all individually offered a significant resistance to platelet deposition. This is evident from the comparisons shown in Figure 6.4 for ASA monotherapy and DAPT. Specifically, platelet deposition on PED+Shield without antiplatelet therapy was similar to PED with ASA monotherapy (Figure 5.4A), and PED+Shield with ASA alone exhibited similar platelet deposition as FRED™ and bare PED under DAPT (Figure 5.4B).

5.5.4 PED devices accrue minimal fibrin compared to FRED™

FRED™ showed significantly higher fibrin deposition than PED or PED+Shield across all antiplatelet conditions (Figure 5.5). The modification of PED with Shield Technology™ was associated with a consistent although never statistically significant fibrin decrease relative to bare PED across all antiplatelet conditions. Harker et al. 1998 [110], published a previous study in this baboon model which established ASA with clopidogrel as the standard DAPT following coronary stenting. The lowest level of mean fibrin accumulation they observed was 0.08 mg/cm on a bare stainless steel stent following 10 mg/kg ASA and 20 mg/kg clopidogrel pretreatment (equivalent to our ASA and ten times our clopidogrel dosing) [110]. Here, in contrast, bare PED showed mean fibrin accumulation of only 0.020 mg/cm with DAPT. Thus, while it is possible that Shield Technology™ confers fibrin resistance which this study failed to capture, there is little room for improvement over the current performance of PED as discernible in this model at 60 min.

5.5.5 Study limitations

This study provides a direct comparison between the thrombogenicity of different flow diversion devices under physiological flow and in the presence of systemic antiplatelet therapy. However we are aware of several limitations to our design. All of the experiments reported here were conducted in a single baboon. Due to their high cost and associated ethical considerations, it is the nature of nonhuman primate studies to be low in sample size. Because one of the problems with clopidogrel use clinically is the wide variability in antiplatelet efficacy associated with cytochrome P450 polymorphisms [168], we elected to conduct our studies in a single animal to reduce variability rather than risk the appearance of between-subjects artifacts. We used LTPA to confirm that our subject was a normal responder (Figure 5.2). The sample size of 3 was based on historical data from this same model in which N=3 yielded a power of 90% with $\alpha=0.05$ in a demonstration of clopidogrel efficacy against platelet deposition [110].

Our quantification of platelet and fibrin deposition from flowing blood provides a useful picture of the risks for device thrombosis; however, the model lacks the capability to robustly quantify incidents of micro-thromboembolism. An indirect detection of macro-thromboembolic events is possible by quantifying decreases in real-time platelet attachment. In this study, a single FRED™ with ASA trial had a decrease in platelet attachment at the 57th minute, indicating an embolic event. Future studies in this model could incorporate a distal filter which could capture thromboemboli and microemboli, enabling their quantification.

This study is further limited by its *ex vivo* nature and acute timescale. While our design addresses the blood flow and coagulation elements of Virchow's triad, by conducting these trials outside the native vasculature, we excluded endothelial damage, which is particularly relevant because of potential vessel wall disruption during device

delivery and deployment. Additional factors missing from this *ex vivo* model include aneurysm presence, vessel tortuosity, and varying boundary conditions in different areas of the cerebral vasculature. Future *ex vivo* studies could address this by moving away from a straight conduit model and instead using more complex 3D models such as those used in early studies of flow diverter fluid dynamics [173]. Given that one goal of flow diverter use is the endothelialization of the aneurysm neck [157], it will also be important to assess whether Shield Technology™ is a substrate which encourages endothelial cell ingrowth while resisting potentially stenotic intimal hyperplasia.

5.5.6 Conclusion

Using a well-established *ex vivo* baboon arteriovenous shunt model of stent thrombosis, we have shown that Shield Technology™ substantially reduces platelet deposition. We have furthermore demonstrated differences in the platelet and fibrin-mediated thrombogenicity of PED and FRED™ devices, which we hypothesize to be flow-related given their previously reported equivalent performances in a static study of material thrombogenicity. While the platelet-specific thromboresistance conferred by Shield Technology™ seen in this acute study is encouraging, implications on the clinical use of these devices will depend on several other factors outside the scope of this model.

Chapter VI: Alternative approaches to modeling *ex vivo* arteriovenous shunt data

6.1 Introduction

As demonstrated in Chapter V, the baboon *ex vivo* arteriovenous shunt model of device-initiated thrombosis is a critical and unique tool for the preclinical evaluation of blood contacting biomaterials. The nature of flowing whole blood in a human-like system without the experimental necessity of antithrombotic drugs allows the prediction of clinical device performance while examining many aspects of thrombotic risk, including the fluid dynamic conditions driven by device geometries. The ability to monitor platelet deposition in real time provides unique information about the dynamics of thrombus initiation and stability.

Over the history of this model, numerous strategies have been used for the statistical analysis of the data it yields. These range in complexity from the t-test for the comparison of end point platelet deposition values [174], to the linear [42] and log-transformed (e.g. chapter V [175]) repeated measures ANOVAs. While all of these analyses can be statistically valid, some, such as the endpoint approach, fail to capture the dynamics of thrombus formation.

The temporal resolution of this platform has increased since the completion of the work presented in Chapter V thanks to the acquisition of a new gamma camera. With this purchase comes greater temporal and spatial resolution. While these are obviously beneficial, a more complex dataset brings a more complex decision making process for modeling and statistical evaluation of datasets. When feasible, parametric analyses are preferred for their generally increased power and flexibility in the incorporation of

covariates. Parametric analyses require balanced experimental designs, near-normal distributions of outcome variable values, and unbiased distributions of residuals. Several techniques exist for the normalization of time series datasets and the reduction of model residuals, including log and exponential transformations, the incorporation of variable interacting terms, and the inclusion of fractional polynomial terms. Sections 6.2 and 6.3 below contain excerpts of published studies including *ex vivo* shunt data analyzed during the course of this dissertation. Both of these studies analyze modifications to poly(vinyl alcohol) (PVA) – a tunable hydrogel biomaterial with significant potential for use as a vascular graft material – meant to increase endothelial cell adhesion while resisting platelet deposition. The study described in 6.2 describes a study which took place using an older camera with 5-minute resolution, while 6.3 describes a study which took place following the acquisition of the higher spatial and temporal resolution camera. 6.2 describes a study which was analyzed using the same log-transform without interactions or fractional polynomial incorporation as used in Chapter V, while 6.3 describes an analysis which used log-transformation in addition to coefficient interactions and fractional polynomials in a linear mixed effects model meant to maximize model fit and reduce residuals across the model. Section 6.3.3 contains (unpublished) illustrations of the model fits and residuals to explain the decision-making process which led to the inclusion of the fractional polynomial model ultimately used in 6.3.

Another critical consideration in the design and analysis of experiments involving the *ex vivo* shunt model is the effect of individual animal variability on outcome variables. Primate research is, for important and valid ethical and financial reasons, a low sample size enterprise. When designing experiments using the *ex vivo* shunt, a balance must be struck between the ability to observe device performance across multiple individuals, ensuring representativeness of a study, and the prevention of the confounding effects of individual variability from influencing the experimental question at hand. In the study

described in Chapter V, the decision was made to prioritize the prevention of confounds by running all studies in a single animal. More commonly, studies are spread out across a small number of animals, with efforts taken to divide replicates evenly between animals[10]. The interpretation of shunt results, and the comparison between published shunt studies, would be aided by a fuller understanding of the predictors of animal-to-animal variability in this model. To that end, section 6.4 describes a pilot hypothesis-generating attempt to identify individual predictors of thrombosis in the *ex vivo* shunt by making use of a retrospective analysis of ePTFE and collagen-coated ePTFE negative and positive controls from across several animals.

[10] It is relevant to point out that these studies consider the biomaterial devices tested, *not* the animals, to be biological replicates

6.2 Luminal reactive ion plasma modification of small diameter polyvinyl alcohol tubular scaffolds[11]

6.2.1 Statistical methods

Statistical comparisons of platelet and fibrin accumulation on PVA samples in ex vivo shunts were calculated using R (R foundation for statistical computing, version 3.5.2) packages nlme (version 3.1-137) and multcomp (version 1.4-8). While ePTFE and collagen ePTFE controls are displayed as a reference in figures, only PVA samples (n=6-7 for each surface modification) were included in statistical models. Platelet and fibrin data were natural-log transformed prior to analysis in order to more closely approximate normal distributions. Transformed real-time platelet adhesion data were analyzed with a multi-way repeated measures ANOVA with factors of time, patterning, and reactive ion plasma treatment over the entire 60min time course. Transformed endpoint fibrin data were analyzed with a two-way ANOVA against patterning and reactive ion plasma treatment. Patterning levels were unpatterned, gratings, and concave. Plasma levels were no plasma, fresh plasma treatment (tested 7-11 days post-treatment), and aged plasma treatment (tested 44-60days post-treatment). Statistically significant main effects were analyzed with a Tukey's post hoc as appropriate.

[11] This is an excerpt of research published in *Frontiers in Bioengineering and Biotechnology*. Pohan G, Chevallier P, Anderson DEJ, Tse JW, Yao Y, Hagen MW, Mantovani D, Hinds MT, Yim EKF. Luminal plasma treatment for small diameter polyvinyl alcohol tubular scaffolds. *Frontiers in Bioengineering and Biotechnology* 2019; 7:117.

6.2.2 Results: *Ex vivo* baboon shunt models show higher platelet accumulation on plasma treated microconcave lenses PVA grafts

The platelet accumulation on both reactive ion plasma treated and untreated PVA grafts was measured every 5 minutes over one-hour duration of study. Eight different types of vascular grafts were tested: unpatterned PVA grafts (reactive ion plasma treated and untreated), microgratings PVA grafts (reactive ion plasma treated and untreated), microconcave lenses PVA grafts (reactive ion plasma treated and untreated), ePTFE grafts (untreated), and collagen coated ePTFE grafts (untreated). The highest platelet accumulation was observed on the collagen coated ePTFE which served as the positive control, whereas unpatterned PVA grafts (reactive ion plasma treated and untreated), microgratings PVA grafts (untreated), and microconcave lenses PVA grafts (untreated) demonstrated low platelet activation.

Untransformed shunt data are shown in Figure 6.1 for better biological interpretation, but statistics were performed on log-transformed data as described in the methods section. A multi-way repeated measures ANOVA found significant effects of both plasma treatment ($p=0.004$) and material patterning ($p=0.011$) on platelet attachment. Microconcave lens patterning significantly increased platelet accumulation from unpatterned samples ($p=0.004$), while microgratings patterning did not significantly alter platelet attachment. Fresh plasma treatments (day 7-11 samples) showed a significant increase in platelet attachment compared to no plasma treatment ($p=0.006$); however, this was not reflected when the plasma treatment was aged (day 44-60 samples, $p=0.195$). The change in platelet accumulation between fresh and aged plasma is shown in Figure 6.2.

Plasma modification did not significantly alter fibrin accumulation in the two-way ANOVA (p=0.386), but patterning was a significant factor (p=0.033). In the post hoc, concave patterning showed a significant increase in fibrin accumulation (p=0.034) compared to unpatterned samples similar to the platelet data, however microgratings did not differ significantly from unpatterned samples (p=0.22).

The same approach was used in a second publication in *Arteriosclerosis, Thrombosis, and Vascular Biology* [176], and was omitted from this document to avoid redundancy.

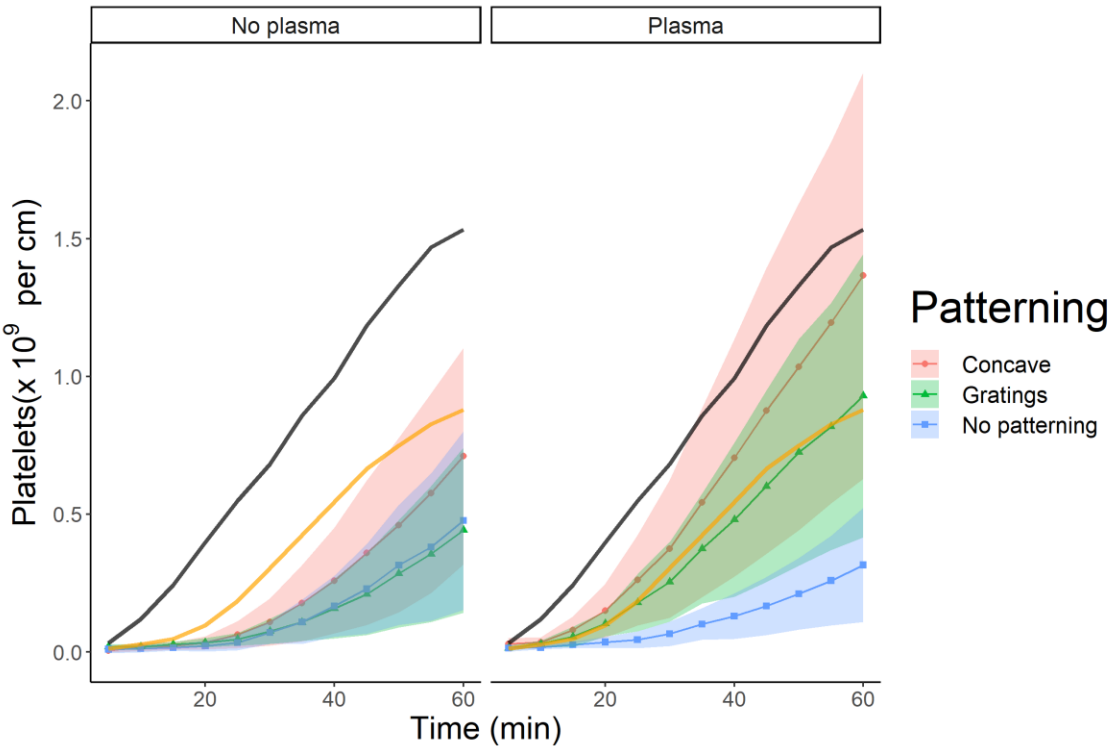

Figure 6.1: Untransformed shunt data for biological interpretation
Platelet accumulation on PVA graft surface after exposure to whole, flowing blood without anticoagulants in the *ex vivo* shunt model. Statistical analysis performed with repeated measures two-way ANOVA. Black overlaid lines: collagen-coated ePTFE. Orange overlaid lines: unmodified ePTFE.

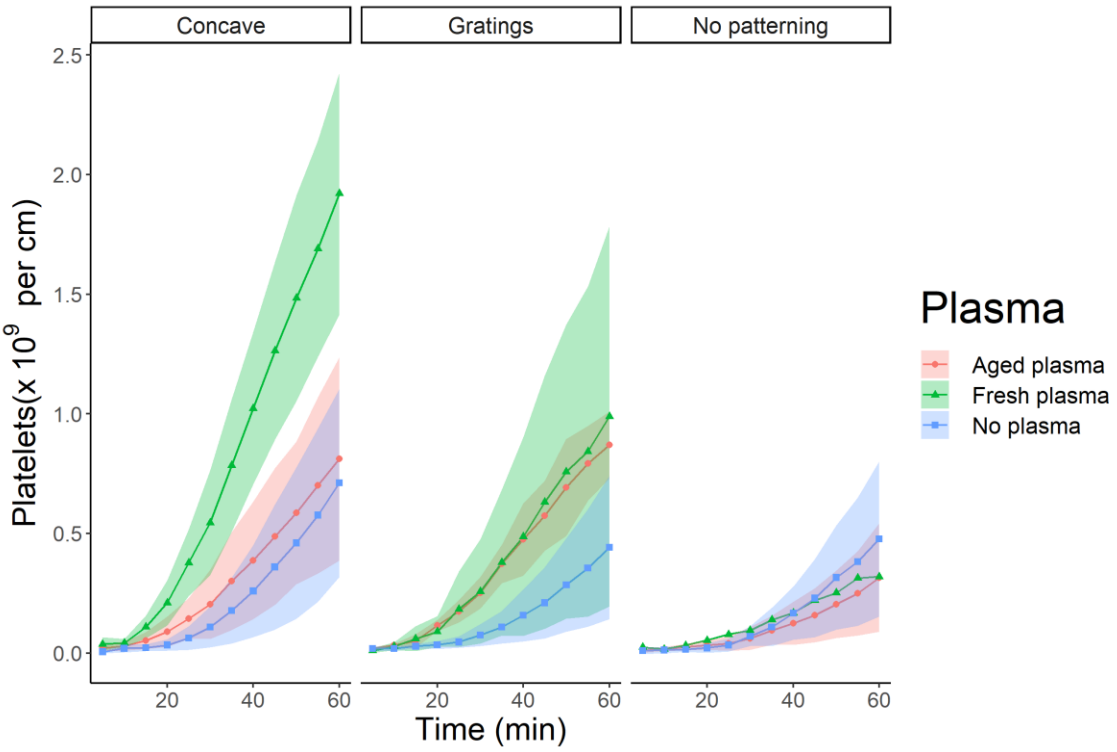

Figure 6.2: Effect of ageing on reactive ion plasma efficacy

Differences in platelet accumulation on patterned and unpatterned PVA graft surfaces between fresh (day 7-11 post-plasma) and aged (day 44-60 post-plasma) reactive ion plasma-treated samples. Fresh plasma showed a significant increase in platelet attachment compared to now plasma samples ($p = 0.006$); however, this was not reflected when the plasma treatment was aged ($p = 0.195$).

6.3 Biomimetic modification of poly(vinyl alcohol): GFPGER performance[12]

6.3.1 Statistical methods

All statistics were calculated using R (R Foundation for Statistical Computing, Vienna, Austria, version 3.5.1). Data are presented as mean ± standard deviation. All statistical analyses were considered significant when $p < 0.05$. Platelet and fibrin data from the ex vivo shunt studies were natural log-transformed in order to approximate a normal distribution. Platelet deposition data were analyzed using multi-way within-drug-groups linear mixed effects models (LME, package nlme version 3.1-137). LMEs included fixed effect coefficients for device material, time, *time* × *ln(time),* interactions, and a random effect term for trial ID. The *time* × *ln(time)* term and its interactions were included to more closely fit the observed data. *Post-hoc* contrasts were manually constructed and p-values were corrected using Tukey contrasts (package multcomp version 1.4-8). Fibrin accumulation was analyzed using within-drug-group 1-way ANOVAs against surface modification with Tukey's *post-hoc* tests when relevant. While the collagen-coated ePTFE controls used to confirm expected reactivity are displayed in figures as references, collagen was not included in statistical models due to low sample size (n = 2 without drugs, n = 1 with ASA or DAPT).

[12] 6.3.1 and 6.3.2 contain excerpts of research published in *Acta Biomaterialia*. Anderson DEJ, Truong KP, Hagen MW, Yim EKF, Hinds MT. Biomimetic modification of poly(vinyl alcohol): encouraging endothelialization and preventing thrombosis with antiplatelet monotherapy. *Acta Biomaterialia* 2019; 86: 291-299.

6.3.2 *ex vivo* shunt platelet deposition results

During ex vivo testing without antiplatelet therapies, GFPGER-PVA accumulated significantly more platelets than ePTFE grafts (Fig 6.3A, p = 0.0035). However under ASA monotherapy, GFPGER and plain PVA devices accumulated significantly fewer platelets than ePTFE (Fig 6.3B, p = 0.001, p < 0.001 respectively). While platelet deposition was minimal across all devices under DAPT, a significant reduction in platelet deposition was seen on plain PVA relative to ePTFE (Fig. 6.3C, p = 0.031).

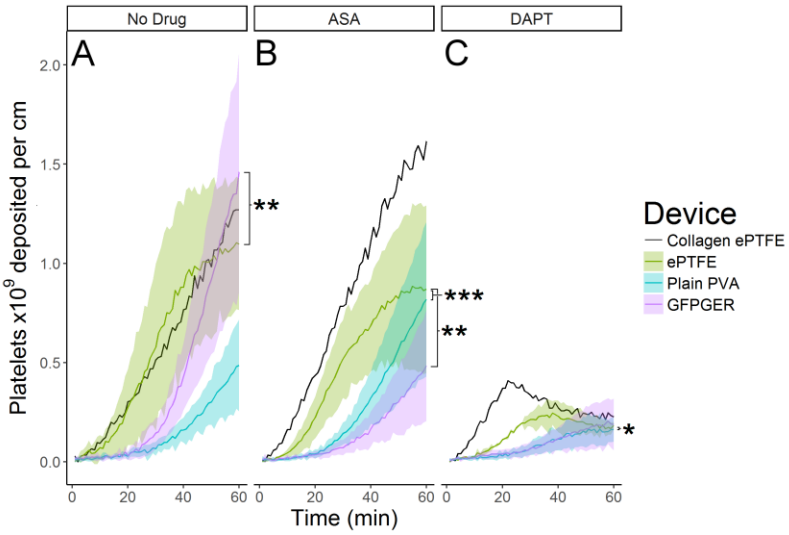

Figure 6.3: Platelet deposition on *ex vivo* shunts.
Tubes of PVA with or without 30 µg GFPGER / g PVA were tested in an *ex vivo* shunt model. Platelet accumulation was quantified over 60 min exposure to whole blood (n = 2 for collagen-eTPFE and N = 5-6 for other groups). (A) in the absence of antiplatelet drugs, ePTFE devices accumulated significantly more platelets than GFPGER devices (LME ANOVA $F_{2,11} = 12.755$ p = 0.001. *post hoc:* ePTFE vs. plain PVA, p = 1.0, ePTFE vs. GFPGER p = 0.0035, plain PVA vs. GFPGER p = 0.0834). (B) Under ASA monotherapy, ePTFE devices accumulated significantly more platelets than either PVA device. (LME ANOVA $F_{2,12} = 13.86$ p = 0.0008, *post hoc:* ePTFE vs. plain PVA p = 0.0008, ePTFE vs. GFPGER p = 0.0013, plain PVA vs. GFPGER p = 1.0). (C) Under DAPT, plain PVA devices accumulated significant fewer platelets than ePTFE devices (LME $F_{2,11} = 3.24$ p = 0.079, *post hoc:* ePTFE vs. plain PVA p = 0.0310, ePTFE vs. GFPGER p = 0.261, plain PVA vs. GFPGER p = 0.681).

6.3.3 Illustrations of model residuals for GFPGER

When constructing a parametric model, the goal is to maximize the fit of normally distributed data while minimizing the possibility of bias in the residuals. Illustrated in Figures 6.4-6.6 are illustrations of the fits and residuals of linear mixed effects models which rely on linear data (Figure 6.4), natural log-transformed data (Figure 6.5) and natural log-transformed data with inclusion of a fractional polynomial term (Figure 6.6). Separate models were constructed for each drug group.

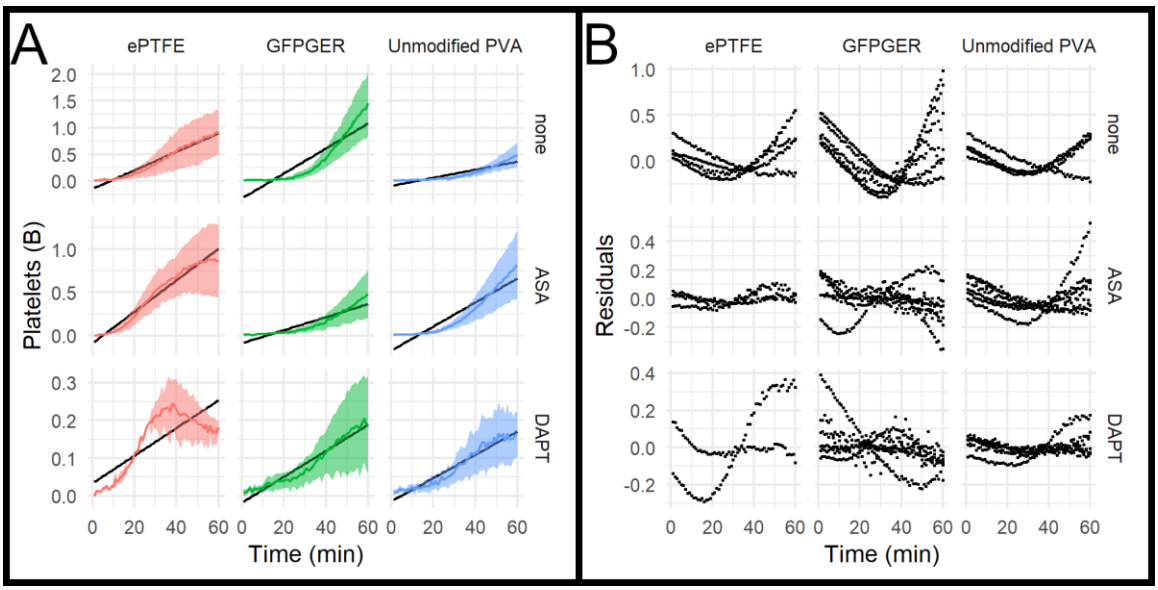

Figure 6.4: Linear LME fit and residuals.
Illustration of linear model with interactions for the GFPGER data summarized in Figure 6.1 (A) Illustration of the predicted values (black) plotted against mean (lines) ± SD (shading) of observed values (colors) (B) Residuals for the linear LME model illustrated in (A).

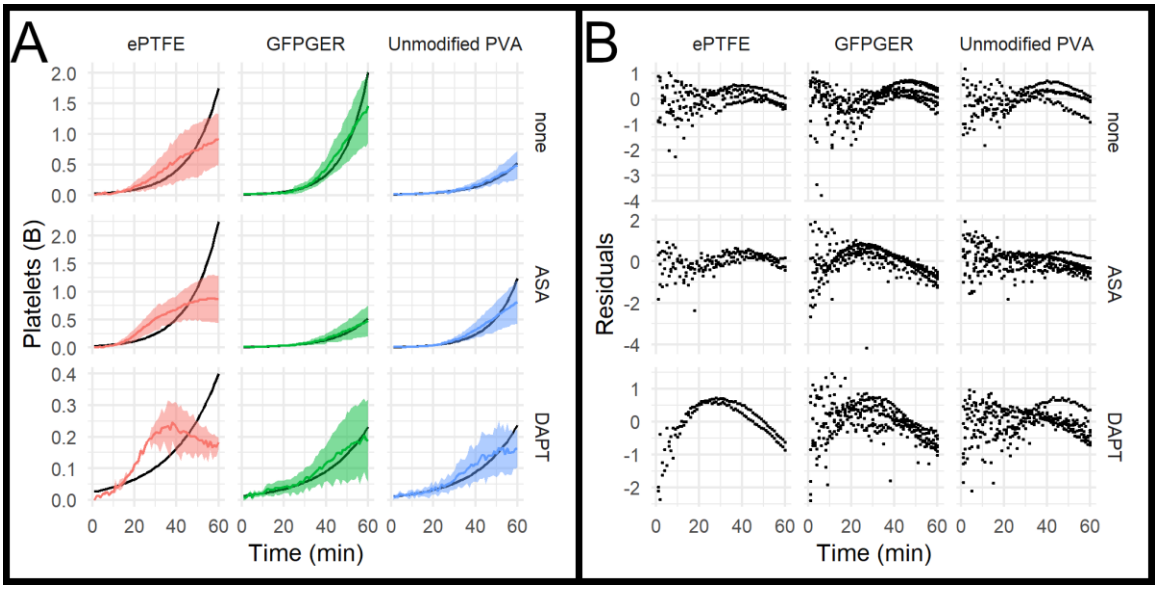

Figure 6.5: Log LME fit and residuals.

Illustration of log-transformed model with interactions for the GFPGER data summarized in Figure 6.3 (A) Illustration of the predicted values (black) plotted against mean (lines) ± SD (shading) of observed values (colors) (B) Residuals for the linear LME model illustrated in (A).

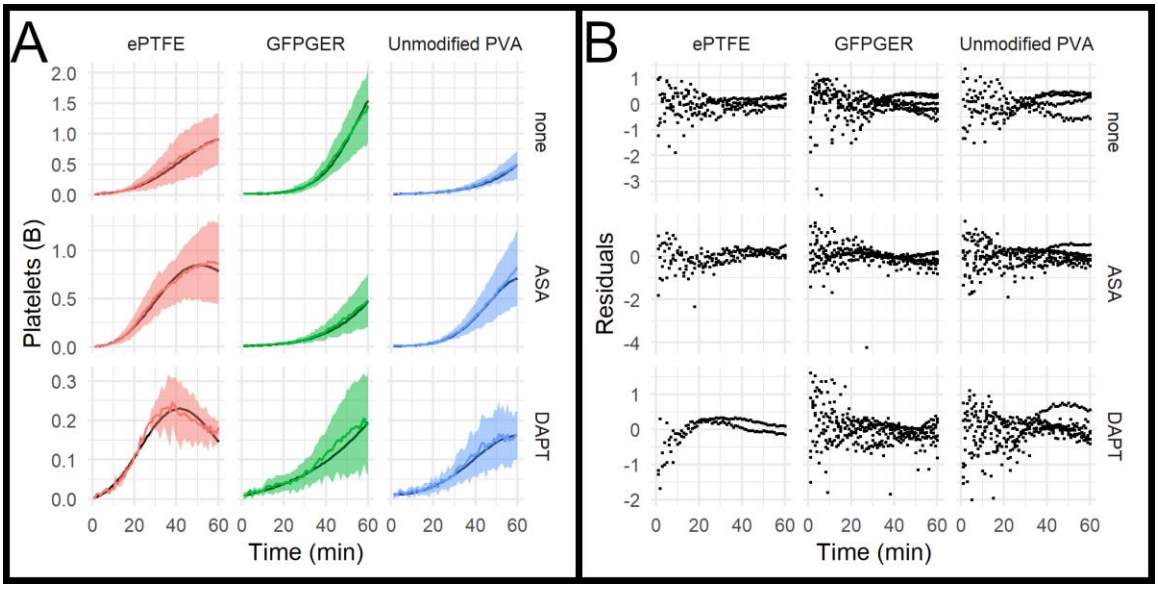

Figure 6.6: Fractional polynomial LME fit and residuals.

Illustration of fractional polynomial model with interactions for the GFPGER data summarized in Figure 6.3 (A) Illustration of the predicted values (black) plotted against mean (lines) ± SD (shading) of observed values (colors) (B) Residuals for the linear LME model illustrated in (A).

6.4 Pilot data: a retrospective analysis of control shunt data, toward the identification of individual predictors of thrombotic risk

Standard arteriovenous shunt studies make use of two controls: an ePTFE current clinical standard “negative” control, and a collagen-coated ePTFE positive control. Given the universality of these control procedures, it was thought that focusing on these controls would be an informative starting point for a retrospective review of shunt experiments in the search for individual predictors of thrombus variability.

6.4.1 Methods

All ePTFE and collagen-coated ePTFE trials which were run in the absence of antiplatelet drugs since the acquisition of the newer gamma camera were included for this pilot analysis. This pilot included ePTFE devices from seven animals, and collagen devices from six animals. Within that set, there were four ePTFE animals with at least two runs, and three collagen animals with at least two runs. The original DICOM files generated by the gamma camera for these trials were identified and imported to FIJI [113]. Using markers placed around the devices prior to the experiment starting point, a box covering 2 cm collagen-coated devices, or 7 cm ePTFE devices was selected as a primary region of interest. Secondary regions of interest were collected in the tail regions in the immediately distal 10 cm. These data were exported as numerical brightness intensity matrices positioning each pixel in x-y-time space. Values were averaged over the height of devices. “Head” data covering the 2 or 7 cm regions occupied by the test devices were averaged by cm, while tail data were examined as functions of time and distance from device.

6.4.2 Results

Direct correlations were sought but could not be identified between platelet deposition and hematocrit, platelet count or white blood cell count. Examination of platelet deposition on ePTFE devices (thrombus head) curves which were grouped by animal, revealed an interesting trend: in the final twenty minutes of a shunt experiment, thrombi tended to either continue growing at a linear rate, level off, or decrease consistently by animal (Figure 6.7). When grouping animal-characterizing statistics by animal, an inverse relationship was found between the final twenty-minute slope and the animal's average aPTT (Figure 6.8), suggesting the possibility of a relationship between these factors.

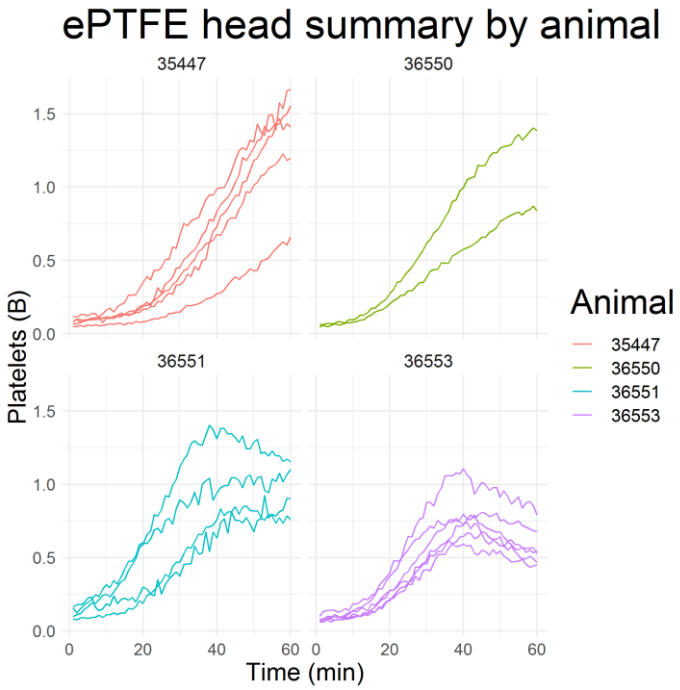

Figure 6.7: ePTFE thrombus head by animal.
The shape of ePTFE head platelet deposition is consistent within the animals examined in this pilot dataset, especially in the highly variable final twenty minutes.

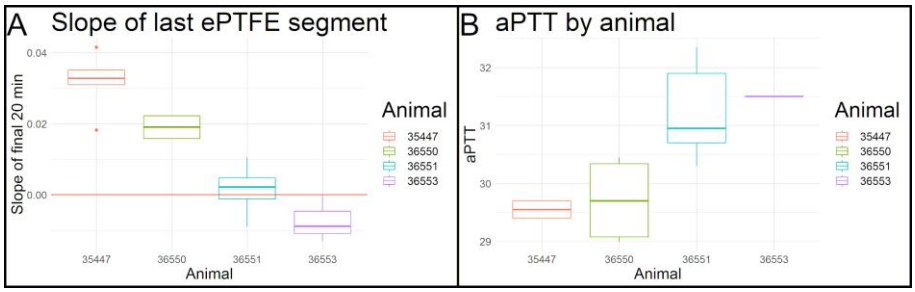

Figure 6.8: Inverse relationship between animal aPTT and final ePTFE slope segment.

There is an inverse relationship between the final 20 minute slope observed in shunt studies and animal average aPTTs. (A) aggregate slope of the final twenty minutes of shunt studies. Red line: average slope of zero. (B) Average animal aPTT.

6.5 Discussion

The nonhuman primate *ex vivo* arteriovenous shunt model continues to be an invaluable tool in the preclinical evaluation of blood-contacting biomaterial devices. As technology increases the resolution and fidelity of real-time platelet deposition data which can be collected from this unique platform, analytical strategies for handling these data should continue to evolve. Increasingly complex linear mixed effects models with the ability to account for numerous interacting predictive variables, and which can be modified with fractional polynomial inclusion to better fit observed data are important tools for this pursuit.

The pilot retrospective analysis undertaken here has identified two unique findings: first that the highly variable platelet aggregation response in the final twenty minutes of an ePTFE graft study may be consistent within animals, and second that that slope may correlate to animal aPTT. These are preliminary findings which can be further investigated with existing datasets. At the outset of this pilot project, there were 57 identified control, antiplatelet drug-free ePTFE trials across 15 animals which could be

further studied. Of these, five animals had n ≥ 3 trials, encompassing 43 trials. Further study of collagen positive controls may be also be informative. 177 collagen trials across 47 animals were identified, with 140 trials across 19 animals having n ≥ 3. The vast majority of these data were produced using an older system with five-minute resolution, however that should be sufficient to confirm the hypothesis generated here.

Chapter VII: Future work

7.1 EC and ECFC micropatterning

The work included in chapters III and IV of this dissertation has demonstrated for the first time that ECFCs can be statically micropatterned through multiple methodologies. As had been previously demonstrated with mature ECs in several studies, the results shown in chapter III demonstrated that static spatial growth restriction micropatterning drove an elongated morphology and increased KLF-2 expression in micropatterned relative to non-patterned ECFCs. In chapter IV it was shown that ECFCs are also sensitive to topographical micropatterning, as indicated by the alignment seen in their cell bodies, actin cytoskeletons, and tubulin cytoskeletons. Notably however, ECFCs did not elongate when topographically patterned, mature ECs showed a far lower degree of elongation on topographical patterns than they previously had in response to either unidirectional fluid shear stress in vivo or on spatial growth restriction micropatterns, and neither cell type showed a gene expression response to micropatterning. The results of chapter IV highlight a result which is not new, but is under-discussed: that topographical micropatterning drives a far weaker degree of endothelial elongation than do unidirectional flow or spatial growth restriction micropatterning. These results raise several questions about (1) the potential utility of luminal topography as a graft modification and (2) the mechanism of endothelial mechanotransduction. Future work in EC and ECFC micropatterning should address three key factors: the interaction of flow with micropatterned cells, the roles of specific ECM components, and the respective roles of the actin and microtubule cytoskeletons.

7.1.1 Interactions between micropatterning and flow

All of the studies documented in chapters III and IV were conducted in fully static culture. Static culture is arguably an injury model, given the similarities in EC morphology and KLF-2 expression levels between cells which are cultured statically and under oscillatory or impinging flow conditions, however it is not fully representative of the complicated realities of the *in vivo* situation. It would be beneficial to understand how topographically micropatterned cells respond, functionally and morphologically, to a variety of unidirectional or oscillating flow regimes.

Of the studies which have examined the combined effects of flow and micropatterning, the vast majority have focused solely on unidirectional flow [80–82]. These reports detail potential synergy between unidirectional fluid shear stress and micropatterning, showing for instance that the combination of unidirectional flow and spatial growth restriction micropatterning drives greater reduction in VCAM-1 expression than either in isolation [81]. Several studies have looked at the effects of unidirectional perpendicular shear stress on the morphology of micropatterned ECs, largely showing that spatial growth restriction micropatterning – and topographical micropatterning on surfaces with pitches exceeding 1 μm – has a greater effect on cell alignment than flow alone [80,82].

These functional flow studies should be expanded to include topographically micropatterned ECs and ECFCs. While no changes in KLF-2, VCAM-1, or E-Selectin expression were found here, it is possible that the pre-alignment of cytoskeletal actin and tubulin might precondition the cells to a more rapid beneficial response to fluid shear stress. At least as relevant would be the study of the responses of topographically patterned cells to oscillatory shear stress. Morphological analyses of micropatterned ECs exposed to perpendicular shear suggest that basal topography has a stronger

influence on cell orientation than apical shear stress, however it is unknown how that translates to the downstream effects of mechanotransduction.

While most of the existing literature examining the combination of flow and patterning has focused on endothelial cell morphology, one study did look more closely at endothelial function. Randomly oriented ECs which had been expanded in static culture were exposed to 30 minutes of unidirectional flow, and cells displayed an orientation-dependent phosphorylation of p65, a component of the NF-κB complex, with cells oriented away from flow showing the greatest level of phosphorylation. Changing the flow direction by 45° or 90° on flow pre-elongated ECs similarly revealed a transient increase in p65 phosphorylation which spiked after 5 minutes and subsided by 15 minutes after the change in direction. Taken together these results suggest that a mismatch between EC orientation and flow direction trigger the atherogenic NF-κB pathway. The same study exposed ECs micropatterned on alternating 5 μm-wide lanes of fibronectin and pluronics to oscillating flow either parallel or perpendicular to the pattern axis. Both regimes increased p65 phosphorylation relative to statically cultured ECs, although perpendicular to a much higher degree than parallel. These experiments only lasted two hours because of weak adhesion to the subcellular biochemical micropatterns used [155]. The micropatterning data further supports the paper's overall conclusion regarding the mechanism of NF-κB upregulation, but also provides a warning to those interested in micropatterning as a technique to mitigate complex flow, namely that establishing a situation of long-term off-axis flow could trigger long-term upregulation of NF-κB signaling, and with it an increased tendency toward inflammation. This could be addressed by exposing topographically micropatterned ECs and ECFCs to perpendicular fluid shear stress, as has been accomplished before [82] and quantifying the expression levels of KLF-2, phosphorylation of NF-κB constituents, and the expression and function of their downstream targets.

7.1.2 Modulation of ECM

The results presented in chapters III and IV used freely adsorbed collagen-I to encourage EC and ECFC adhesion to test surfaces. Collagen-I is affordable, encourages strong adhesion, and is not particularly immunogenic. However, the natural basal lamina contains a diverse collection of ECM components, and it has been shown that ECM composition affects EC function, and vice-versa [112,177]. As a particular example, studies of the pathways linking shear stress with changes in cytoskeletal signaling cited the necessity of the formation of new integrin connections with fibronectin to further signal transduction [77]. While cultured ECs and ECFCs readily begin excreting ECM components, the effect of ECM composition on micropatterned cell function remains a worthy area of study.

The inherent thrombogenicity of collagen makes its potential inclusion in a vascular device dangerous. Novel techniques based on the direct modification of ECM may be useful components to integrate into future studies of micropatterning. Ongoing work into experimental truncated peptide sequences which can encourage EC adhesion without drastically increasing the risk of platelet activation and thrombosis provides one potential avenue for exploration. In a static adhesion assay, GFPGER, a component of collagen, was shown to encourage greater ECFC adhesion than collagen-I, fibronectin, or laminin [138]. As the study of luminal topography toward construction of an *in vitro* endothelializable vascular device moves closer to the clinic, these peptides should be considered.

Other recent work has demonstrated that the orientation of ECM components influences the orientation of the ECs cultured on them. One group has developed a technique for the extrusion of aligned nanofibrillar collagen, from which a hydrogel supporting cultured ECs can be created. Culture on nanofibrillar collagen was found to

align and elongate ECs with SIs near 0.4, close to what has been seen *in vivo* and what was found using spatial growth restriction in chapter III. This study also demonstrated reduced ICAM-1 gene expression by and reduced monocyte adhesion to ECs cultured on nanofibrillar collagen relative to those on disorganized collagen [150]. Importantly, all of those studies took place under flow (either impinging, parallel, or perpendicular to the angle of alignment) making a direct comparison with the static culture results presented here difficult. Biomimetic pre-aligned ECM can also be created using decellularized matrix created from micropatterned SMCs, fibroblasts, or glia [178], however this has yet to be examined with endothelial cells. While these two techniques are a departure from alterations of luminal topography, they do represent another potential avenue for translatable EC or ECFC micropatterning, and collaborations should be considered.

7.1.3 Cell-by-cell correlates of morphology and function

As further study of the interaction of topography and flow is pursued, the single-cell sensitivity of the image analysis tools described in chapter IV should be leveraged. The work in this dissertation assessed morphology using quantitative imaging techniques, and function using qPCR. However, immunofluorescence is another powerful tool which can be used to visualize and quantify the localization and production levels of proteins. By using the cell outline-defined image segmentation techniques described in chapter IV, cell-specific expression level data could be gathered. This would allow the robust quantification of the cell-by-cell expression levels of factors as varied as KLF-2, surface adhesion molecules, NF-κB complex constituents, eNOS, and others, while correlating them to measures of whole-cell and cytoskeletal morphology.

One of the interesting differences between the ECs and ECFCs studied in chapter IV is the increased variability in all metrics of morphology seen in ECFCs relative to ECs. While the bulk trends were as reported, namely that ECFCs showed cellular and

cytoskeletal alignment but not elongation and no changes in gene expression in response to topographic micropatterning, the histograms displayed in figures 4.3-4.6 and A1.1-A1.6 make clear that there is a greater degree of variability within ECFCs than ECs. The novel tools described above would enable a robust quantification of the link between cell morphology and function which could be used to address the hypothesis that cell elongation, not alignment, is the morphological correlate of atheroprotection.

7.2 Ex vivo assessments of material thrombogenicity

In chapter V, data were presented showing that phosphorylcholine-modified cobalt-chromium cerebral flow diverters accumulated far fewer platelets than unmodified devices across all antiplatelet drug conditions tested. Historically, the greatest risk posed by the use of low-thrombogenicity materials is late term device-initiated thrombosis. This has been seen extensively in patients who receive newer generation drug eluting coronary stents [3]. Given the nature of the collaboration which led to Chapter V, the specific mechanism of attachment of phosphorylcholine to the cobalt chromium body of the device is proprietary and unknown to the writer of this dissertation. Long-term testing should be carried out to examine the durability of the phosphorylcholine modification, to ensure that its late term loss does not cause eventual thrombosis in a patient who is not treated with adequate antiplatelet therapy.

Chapter VI discussed strategies for the analysis of *ex vivo* arteriovenous shunt data, and introduced the pilot results of a retrospective study of historical shunt controls. This hypothesis-generating study successfully generated the hypothesis that animal aPTT may be a predictor of the dynamics of platelet accumulation on hydrophobic devices. The completion of this retrospective review with all available data will be

informative. However, a critical weakness in the pilot dataset is that animal aPTT is not typically recorded simultaneous with *ex vivo* shunt studies. Including this recording at the time of control experiments will yield a more robust dataset with which to address this novel hypothesis.

Appendix A: Supplemental data for topographical micropatterning

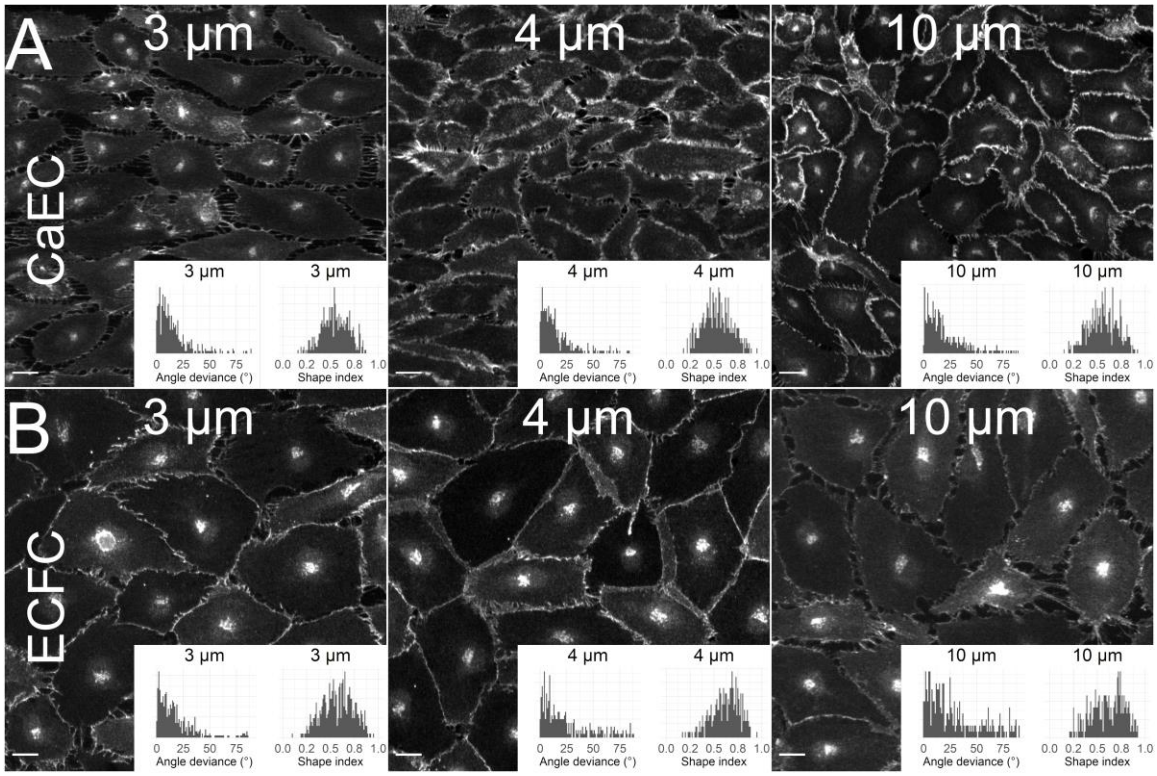

Figure A1.1: Representative images of VE-Cadherin staining on topographical micropatterns with pitches of 3, 4, and 10 µm.
Micrographs showing VE-Cadherin staining of (A) CaECs and (B) ECFCs on topographical patterns after 24 hours with (left) 3 µm (center) 4 µm, and (right) 10 µm pitches. Insets: histograms showing the distribution of whole-cell angle deviances (left) and shape indices (right) for the full dataset.

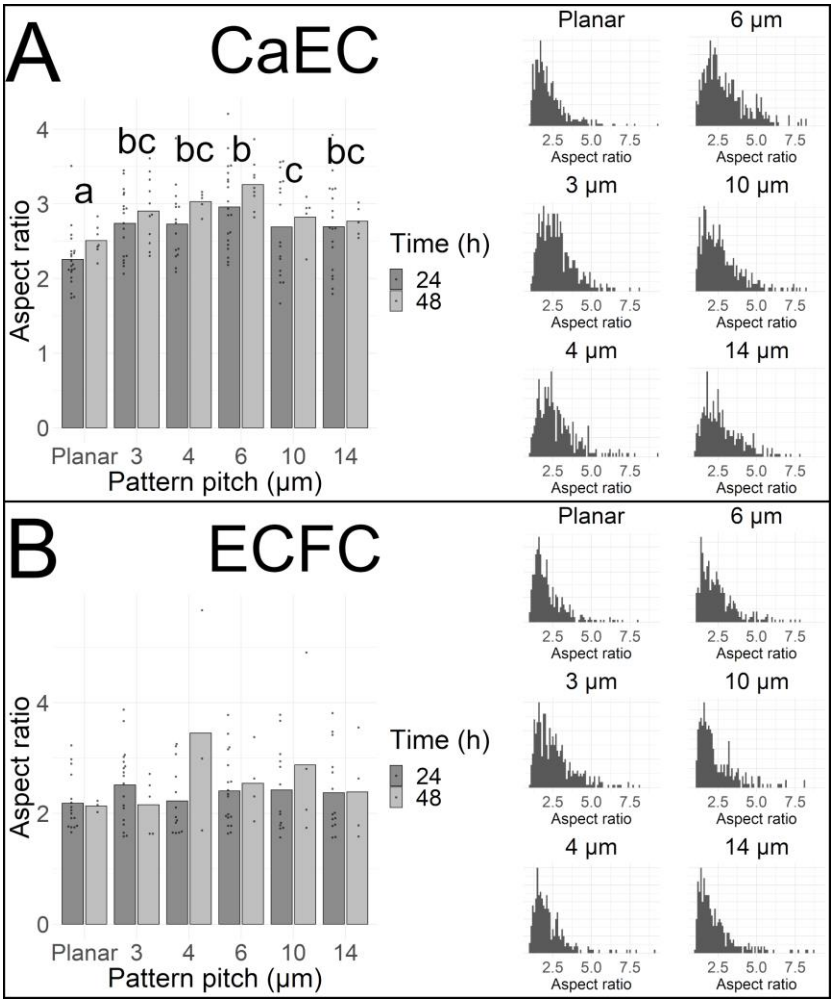

Figure A1.2: Cell elongation reported as aspect ratio.

Cell elongation data were also recorded as aspect ratio, the quotient of cells' major axis by its minor axis. (A) CaECs displayed statistically significant increases in cell aspect ratio on every pattern pitch tested compared to planar. (B) ECFCs showed no significant aspect ratio effect of micropatterning. Main plots: summaries displaying mean (bars) and biological replicate mean (dots) aspect ratios. Pitch groups sharing letters are not statistically different by post-hoc Tukey test ($p > 0.05$). Inset panels: histograms showing the raw distributions of aspect ratio measurements of every cell traced at 24 hours.

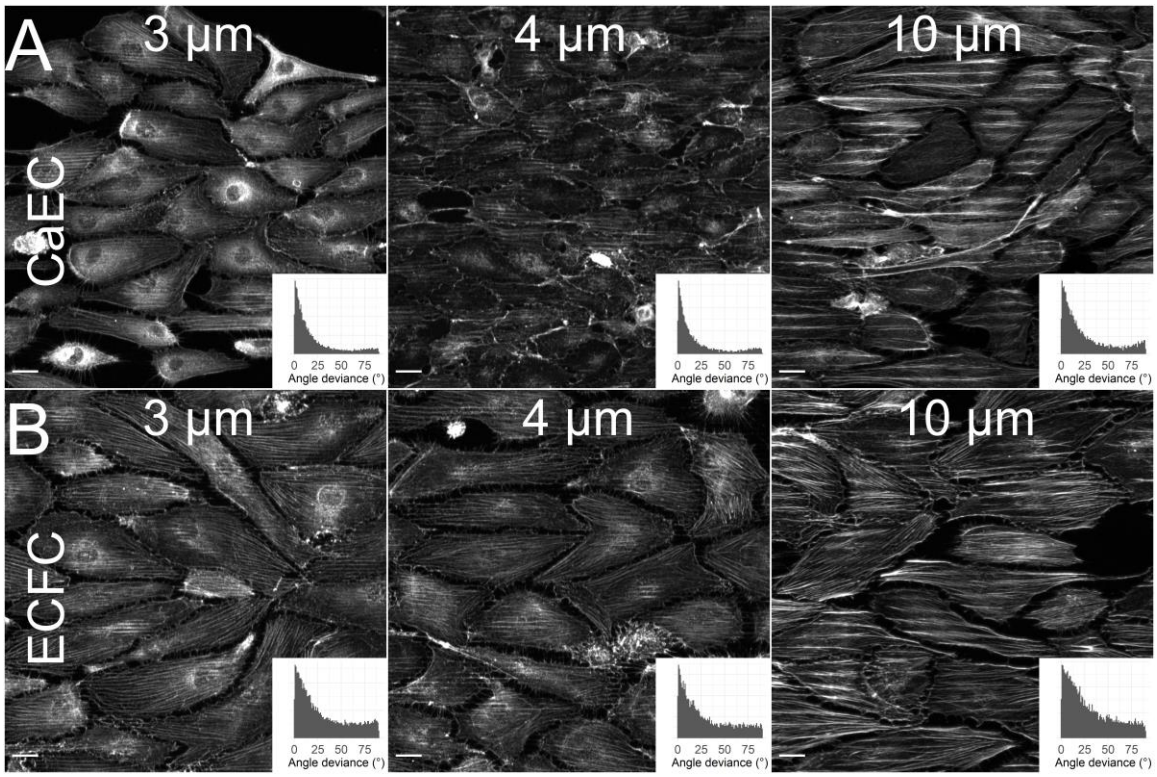

Figure A1.3: Representative images of actin staining on topographical micropatterns with pitches of 3, 4, and 10 μm.

Micrographs showing F-actin staining in (A) CaECs and (B) ECFCs on topographical patterns after 24 hours with (left) 3 μm (center) 4 μm, and (right) 10 μm pitches. Insets: histograms showing the distribution of actin fiber alignments in each cell type-pitch combination.

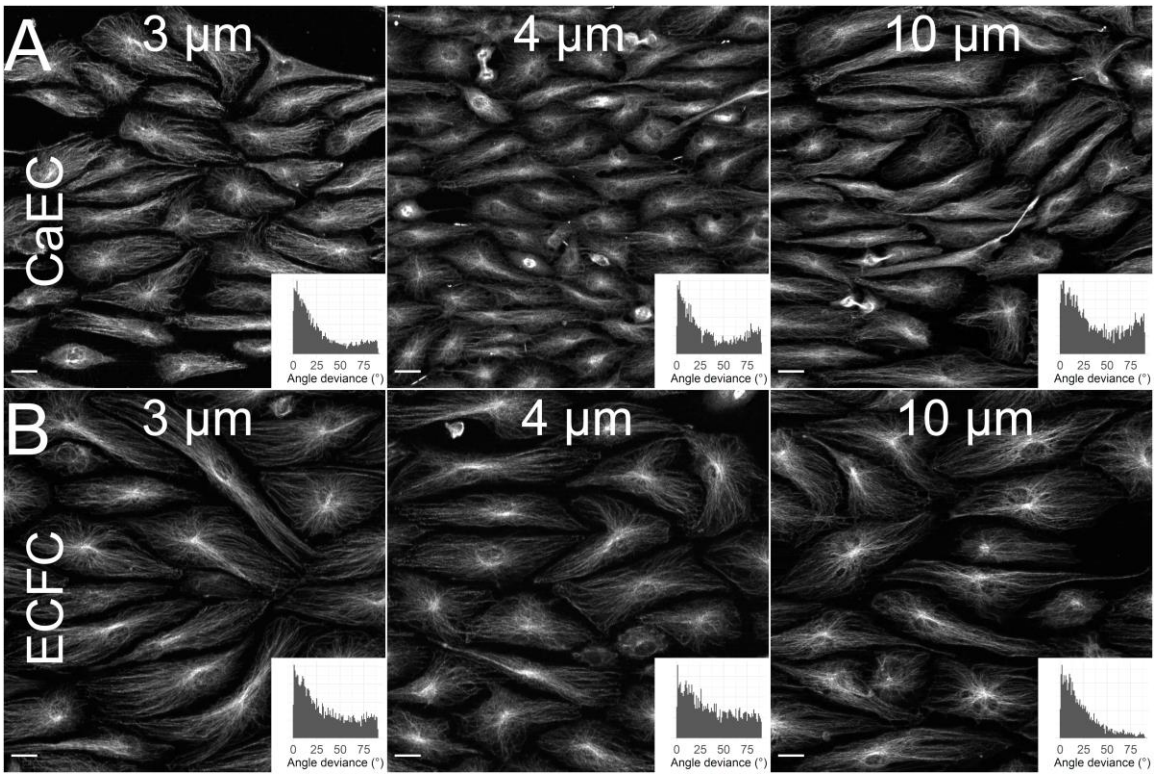

Figure A1.4: Representative images of tubulin staining on topographical micropatterns with pitches of 3, 4, and 10 μm.

Micrographs showing β-Tubulin staining in (A) CaECs and (B) ECFCs on topographical patterns after 24 hours with (left) 3 μm, (center) 4 μm, and (right) 10 μm pitches. Insets: histograms showing the distribution of tubulin fiber alignments in each cell type-pitch combination.

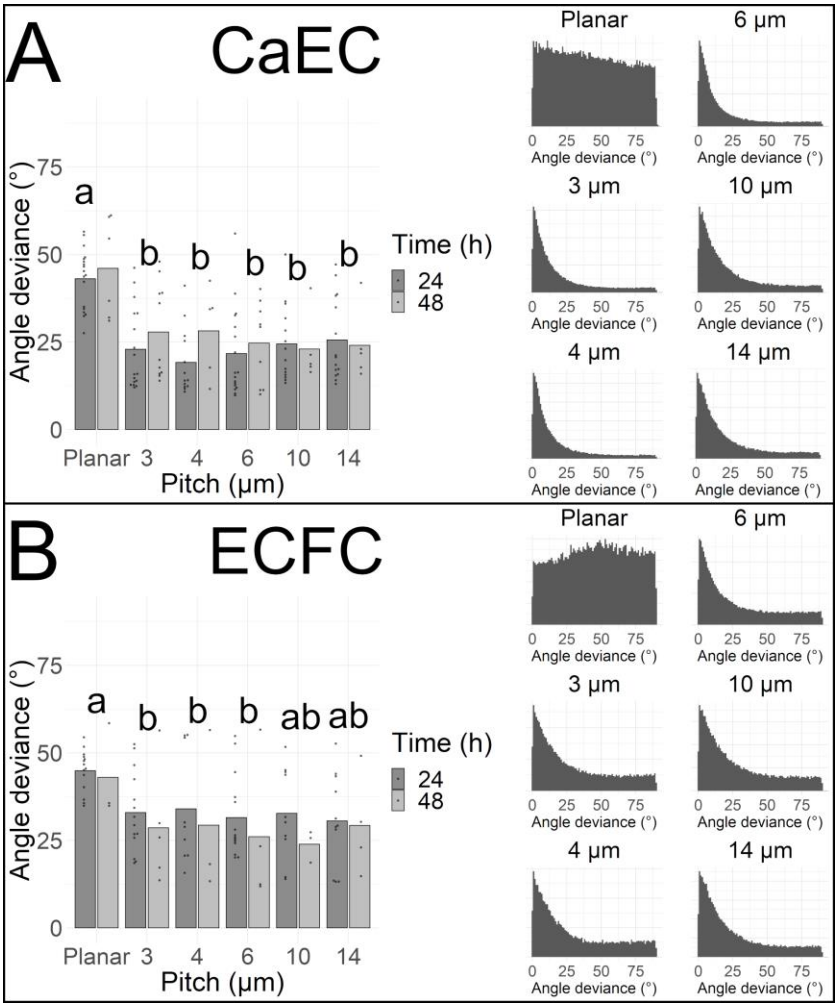

Figure A1.5: Aggregate actin alignment.

Summary of actin alignment as measured using an image aggregate, rather than cell-by-cell technique. (A) CaEC actin alignment, (B) ECFC actin alignment. Main plots show mean (bars) and biological replicate mean (dots) angle deviances. Pitch groups sharing letters are not statistically different by post-hoc Tukey test ($p > 0.05$). Insets: histograms illustrating the raw distribution of all measured actin fibers.

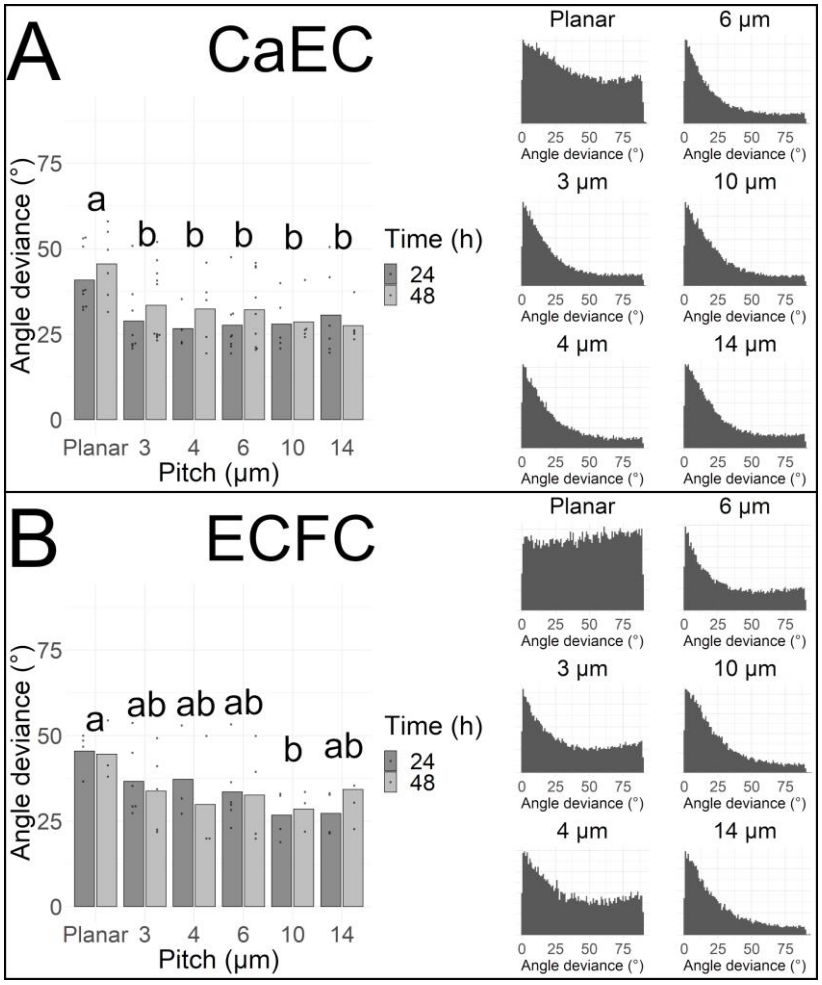

Figure A1.6: Aggregate tubulin alignment.

Summary of tubulin alignment as measured using an image aggregate, rather than cell-by-cell technique. (A) CaEC tubulin alignment, (B) ECFC tubulin alignment. Main plots show mean (bars) and biological replicate mean (dots) angle deviances. Pitch groups sharing letter groups are not statistically different by post-hoc Tukey test ($p > 0.05$). Insets: histograms illustrating the raw distribution of all measured tubulin fibers.

Appendix B: IJM code

9.1 Single-cell actin and tubulin tracing

```
// Language: IJM1. Written by Matthew Hagen, 2019
// Prerequisites: FIJI with ImageJ 1.52p or above, ensure pre-
// installation of 'Find focused slices' plugin.
// CRITICAL: ensure no spaces in file paths or file names

// Setup and define file paths:
stack_path = "X:\\sample\\path1"; // Where are the stacks?
roi_path = "X:\\sample\\path2"; // Where are the ROIs?
apto = "X:\\sample\\path3"; //Send single cell results to
imgto = "X:\\sample\\path5"; // path for image montages
//files = getFileList(stack_path); //Option 1: pull filenames
roots = newArray("file1", "file2"); // Option 2: list files
run("Set Measurements...", "area perimeter fit shape redirect=None
decimal=3");

//Start for loop:
for(i = 0; i< roots.length; i++){
      root = roots[i];
      run("Bio-Formats (Windowless)", "open=" + stack_path +"\\" + root
      + ".czi"); //Change .ext if necessary
      rename(root);
      roiManager("open", roi_path + "\\" + root + ".zip");


      z = roiManager("count");
      for(j = 0; j<z; j++){
            roiManager("Select", j);
            run("Duplicate...", "duplicate");
            rename("Stack" + j);
            run("Clear Outside", "stack");
            run("Split Channels");
            selectWindow("C3-" + "Stack" + j); //ALWAYS CHECK THIS
            run("Close"); // close DAPI


            // start Tubulin analysis:
            selectWindow("C2-" + "Stack" + j); //Again: check yourself
            before you wreck yourself.
            run("Find focused slices", "select=100 variance=0.000");
            //Select single slice
            rename("Tubulin_focus_" + j);
            run("8-bit"); //Anything below 32 bit will also work here
            run("Subtract Background...", "rolling=50");
```

```
            run("Auto Local Threshold", "method=MidGrey radius=15
            parameter_1=0 parameter_2=0 white");
            run("Analyze Particles...", "size=2-200 circularity=0.00-
            0.30 show=[Overlay Masks] display ");
            run("Flatten");
            rename("Tubulin" + j);
            saveAs("Results", apto + "\\" + root + "Tubulin" + j +
            ".csv"); // Yes, you need to save as .csv
            run("Clear Results"); //Owen if you find this by 12/16/19
            I'll buy you coffee for a month
            selectWindow("Tubulin_focus_" + j);
            run("Close");
            selectWindow("C2-" + "Stack" + j);
            run("Close");
            //end tubulin analysis


            // start Actin analysis
            selectWindow("C1-" + "Stack" + j); //Again: check this
            run("Find focused slices", "select=100 variance=0.000");
            rename("Actin_focus_" + j);
            run("8-bit");
            run("Subtract Background...", "rolling=50");
            run("Auto Local Threshold", "method=MidGrey radius=15
            parameter_1=0 parameter_2=0 white");
            run("Analyze Particles...", "size=2-200 circularity=0.00-
            0.30 show=[Overlay Masks] display ");
            run("Flatten");
            rename("Actin" + j);
            saveAs("Results", apto + "\\" + root + "Actin" + j +
            ".csv");
            run("Clear Results");
            selectWindow("Actin_focus_" + j);
            run("Close");
            selectWindow("C1-" + "Stack" + j);
            run("Close");
            // end actin analysis
            selectWindow(root);
            }

      // Create Tubulin summary graphic
      run("Images to Stack", "method=[Copy (center)]
      name=Tubulin_summary title=Tubulin use");
      run("Make Montage...", "columns=4 rows=3 scale=1 border=10");
      saveAs("PNG", imgto + "\\" + root + "Tubulin.png");
      run("Close");
      // Create actin summary graphic
      run("Images to Stack", "method=[Copy (center)] name=Actin_summary
      title=Actin use");
      run("Make Montage...", "columns=4 rows=3 scale=1 border=10");
      saveAs("PNG", imgto + "\\" + root + "Actin.png");
      roiManager("Deselect");
      roiManager("Delete");
      run("Close All");
}
//fin
```

9.2 Aggregate actin and tubulin tracing

```
// Language: IJM1. Written by Matthew Hagen, 2019
// Prerequisites: FIJI with ImageJ 1.52p or above, ensure pre-
// installation of 'Find focused slices' plugin.
// CRITICAL: ensure no spaces in file paths or file names

// Setup and define file paths:
stack_path = "X:\\sample\\path1"; // Where are the stacks?
apto = "X:\\sample\\path3"; //Send single cell results to
imgto = "X:\\sample\\path5"; // path for image montages
//files = getFileList(stack_path); //Option 1: pull filenames
roots = newArray("file1", "file2"); // Option 2: list file names w/out
.ext
run("Set Measurements...", "area perimeter fit shape redirect=None
decimal=3");

//Start for loop:
for(i = 0; i< roots.length; i++){
      root = roots[i];
      run("Bio-Formats (Windowless)", "open=" + stack_path +"\\" + root
      + ".czi"); //Change .ext if necessary
      rename(root);

      //ACTIN:
      selectWindow(root);
      run("Split Channels");
      selectWindow("C3-" + root); //Close DAPI
      run("Close");
      selectWindow("C1-" + root); //ALWAYS CHECK THIS
      run("8-bit");
      for(j = 0; j< 20; j++){
            for(k = 0; k<20; k++){
                  index = (j*20)+k+1;
                  xmin = j*193;
                  ymin = k*193;
                  makeRectangle(xmin, ymin, 193, 193);
                  run("Duplicate...", "duplicate");
                  rename("raw_crop");
                  run("Find focused slices", "select=100
                  variance=0.000");
                  rename("frame");
                  run("Subtract Background...", "rolling=50");
                  run("Auto Local Threshold", "method=MidGrey radius=15
                  parameter_1=0 parameter_2=0 white");
                  run("Analyze Particles...", "size=2-200
                  circularity=0.00-0.30 show=[Overlay Masks] display
                  ");
                  selectWindow("frame");
                  run("Close");
                  selectWindow("raw_crop");
                  run("Close");
                  selectWindow("C1-" + root);
            }
      }
```

```
	saveAs("Results", apto + "\\" + root + "_ACTIN.csv");
	run("Clear Results");

	// TUBULIN:
	selectWindow("C2-" + root); //ALWAYS CHECK THIS
	run("8-bit");
	for(j = 0; j< 20; j++){
		for(k = 0; k<20; k++){
			index = (j*20)+k+1;
			xmin = j*193;
			ymin = k*193;
			makeRectangle(xmin, ymin, 193, 193);
			run("Duplicate...", "duplicate");
			rename("raw_crop");
			run("Find focused slices", "select=100
			variance=0.000");
			rename("frame");
			run("Subtract Background...", "rolling=50");
			run("Auto Local Threshold", "method=MidGrey radius=15
			parameter_1=0 parameter_2=0 white");
			run("Analyze Particles...", "size=2-200
			circularity=0.00-0.30 show=[Overlay Masks] display
			");
			selectWindow("frame");
			run("Close");
			selectWindow("raw_crop");
			run("Close");
			selectWindow("C2-" + root);
		}
	}
	saveAs("Results", apto + "\\" + root + "_TUBULIN.csv");
	run("Clear Results");

	run("Close All");
}

//fin
```

References

1. Benjamin EJ, Muntner P, Alonso A, Bittencourt MS, Callaway CW, Carson AP, et al. Heart Disease and Stroke Statistics-2019 Update: A Report From the American Heart Association. Circulation. 2019. doi:10.1161/CIR.0000000000000659
2. Hansson GK. Inflammation, atherosclerosis, and coronary artery disease. N Engl J Med. 2014;352: 1685–1695. doi:10.1056/NEJM200507283530425
3. Bangalore S, Kumar S, Fusaro M, Amoroso N, Attubato MJ, Feit F, et al. Short-and long-term outcomes with drug-eluting and bare-metal coronary stents: A mixed-treatment comparison analysis of 117 762 patient-years of follow-up from randomized trials. Circulation. 2012;125: 2873–2891. doi:10.1161/CIRCULATIONAHA.112.097014
4. Donker JMW, Ho GH, Te Slaa A, De Groot HGW, Van Der Waal JCH, Veen EJ, et al. Midterm results of autologous saphenous vein and ePTFE pre-cuffed bypass surgery in peripheral arterial occlusive disease. Vasc Endovascular Surg. 2011;45: 598–603. doi:10.1177/1538574411414923
5. Taylor LM, Edwards JM, Brant B, Phinney ES, Porter JM. Autogenous reversed vein bypass for lower extremity ischemia in patients with absent or inadequate greater saphenous vein. Am J Surg. 1987;153: 505–510. doi:10.1016/0002-9610(87)90803-8
6. Aird WC. Endothelial cell heterogeneity. Cold Spring Harb Perspect Med. 2012;2: 1–13. doi:10.1101/cshperspect.a006429
7. Borysenko M. Functional histology: a core text. 1st ed. Boston, MA: Little, Brown; 1979.
8. Gutterman DD. Adventitia-dependent influences on vascular function. Am J Physiol - Hear Circ Physiol. 1999;277. doi:10.1152/ajpheart.1999.277.4.h1265
9. van der Loo B, Martin JF. The Adventitia, Endothelium and Atherosclerosis. Int J Microcirc. 1997;17: 280–288. doi:10.1159/000179240
10. Hu Y, Xu Q. Adventitial biology: Differentiation and function. Arterioscler Thromb Vasc Biol. 2011;31: 1523–1529. doi:10.1161/ATVBAHA.110.221176
11. Hoglund VJ, Rong Dong X, Majesky MW. Neointima formation: A local affair. Arterioscler Thromb Vasc Biol. 2010;30: 1877–1879. doi:10.1161/ATVBAHA.110.211433
12. Daniel JM, Bielenberg W, Stieger P, Weinert S, Tillmanns H, Sedding DG. Time-course analysis on the differentiation of bone marrow-derived

progenitor cells into smooth muscle cells during neointima formation. Arterioscler Thromb Vasc Biol. 2010;30: 1890–1896. doi:10.1161/ATVBAHA.110.209692

13. Pugsley MK, Tabrizchi R. The vascular system: An overview of structure and function. J Pharmacol Toxicol Methods. 2000;44: 333–340. doi:10.1016/S1056-8719(00)00125-8

14. Rodrigues SF, Granger DN. Blood cells and endothelial barrier function. Tissue Barriers. 2015;3. doi:10.4161/21688370.2014.978720

15. Chistiakov DA, Orekhov AN, Bobryshev Y V. Endothelial barrier and its abnormalities in cardiovascular disease. Front Physiol. 2015;6: 1–11. doi:10.3389/fphys.2015.00365

16. Lertkiatmongkol P, Liao D, Mei H, Hu Y, Newman PJ. Endothelial functions of PECAM-1 (CD31). Curr Opin Hematol. 2016;23: 253–259. doi:10.1097/MOH.0000000000000239.Endothelial

17. Reitsma S, Slaaf DW, Vink H, Van Zandvoort MAMJ, Oude Egbrink MGA. The endothelial glycocalyx: Composition, functions, and visualization. Pflugers Arch Eur J Physiol. 2007;454: 345–359. doi:10.1007/s00424-007-0212-8

18. Klitzman B, Duling BR. Microvascular hematocrit and red cell flow in resting and contracting striated muscle. Am J Physiol. 1979;237: H481-90. doi:10.1152/ajpheart.1979.237.4.H481

19. Vink H, Duling BR. Identification of distinct luminal domains for macromolecules, erythrocytes, and leukocytes within mammalian capillaries. Circ Res. 1996;79: 581–9. doi:10.1161/01.res.79.3.581

20. Megens RTA, Reitsma S, Schiffers PHM, Hilgers RHP, De Mey JGR, Slaaf DW, et al. Two-photon microscopy of vital murine elastic and muscular arteries. Combined structural and functional imaging with subcellular resolution. J Vasc Res. 2007;44: 87–98. doi:10.1159/000098259

21. Potter DR, Damiano ER. The hydrodynamically relevant endothelial cell glycocalyx observed in vivo is absent in vitro. Circ Res. 2008;102: 770–776. doi:10.1161/CIRCRESAHA.107.160226

22. Potter DR, Jiang J, Damiano ER. The recovery time course of the endothelial cell glycocalyx in vivo and its implications in vitro. Circ Res. 2009;104: 1318–1325. doi:10.1161/CIRCRESAHA.108.191585

23. Barakat AI. Dragging along: The glycocalyx and vascular endothelial cell mechanotransduction. Circ Res. 2008;102: 747–748. doi:10.1161/CIRCRESAHA.108.174839

24. Lin J, Kakkar V, Lu X. Impact of MCP-1 in atherosclerosis. Curr Pharm Des. 2014;20: 4580–8. doi:10.2174/1381612820666140522115801

25. Rao RM, Yang L, Garcia-Cardena G, Luscinskas FW. Endothelial-dependent mechanisms of leukocyte recruitment to the vascular wall. Circ

Res. 2007;101: 234–247. doi:10.1161/CIRCRESAHA.107.151860b

26. Metcalf DJ, Nightingale TD, Zenner HL, Lui-Roberts WW, Cutler DF. Formation and function of Weibel-Palade bodies. J Cell Sci. 2008;121: 19–27. doi:10.1242/jcs.03494

27. Springer TA. von Willebrand factor, Jedi knight of the bloodstream. Blood. 2014;124: 1412–1425. doi:10.1182/blood-2014-05-378638

28. Nightingale T, Cutler D. The secretion of von Willebrand factor from endothelial cells; an increasingly complicated story. J Thromb Haemost. 2013;11: 192–201. doi:10.1111/jth.12225

29. Tohgi H, Utsugisawa K, Yoshimura M, Nagane Y, Ukitsu M. Local variation in expression of pro- and antithrombotic factors in vascular endothelium of human autopsy brain. Acta Neuropathol. 1999;98: 111–118. doi:10.1007/s004010051058

30. Förstermann U, Sessa WC. Nitric oxide synthases: Regulation and function. Eur Heart J. 2012;33: 829–837. doi:10.1093/eurheartj/ehr304

31. Beaulieu LM, Freedman JE. Inhibition of platelet function by the endothelium. Third. In: Michelson AD, editor. Platelets. Third. London: Elsevier; 2013. pp. 313–342.

32. Leslie M. Beyond clotting: The powers of platelets. Science (80-). 2010;328: 562–564. doi:10.1126/science.328.5978.562

33. McCarty OJT, Mousa SA, Bray PF, Konstantopoulos K. Immobilized platelets support human colon carcinoma cell tethering, rolling, and firm adhesion under dynamic flow conditions. Blood. 2000;96: 1789–97.

34. Tangelder GJ, Teirlinck HC, Slaaf DW, Reneman RS. Distribution of blood platelets flowing in arterioles. Am J Physiol - Hear Circ Physiol. 1985;17. doi:10.1152/ajpheart.1985.248.3.h318

35. Mccarty OJT, Calaminus SDJ, Berndt MC, Machesky LM, Watson SP. von Willebrand factor mediates platelet spreading through glycoprotein Ib and αIIbβ3 in the presence of botrocetin and ristocetin, respectively. J Thromb Haemost. 2006;4: 1367–1378. doi:10.1111/j.1538-7836.2006.01966.x

36. Broos K, Feys HB, De Meyer SF, Vanhoorelbeke K, Deckmyn H. Platelets at work in primary hemostasis. Blood Rev. 2011;25: 155–167. doi:10.1016/j.blre.2011.03.002

37. Davie EW, Ratnoff OD. Waterfall sequence for intrinsic blood clotting. Science (80-). 1964;145: 1310–2. doi:10.1126/science.145.3638.1310

38. Mann KG, Orfeo T, Butenas S, Undas A, Brummel-Ziedins K. Blood coagulation dynamics in haemostasis. Hamostaseologie. 2009;29: 7–16.

39. Renné T. The procoagulant and proinflammatory plasma contact system. Semin Immunopathol. 2012;34: 31–41. doi:10.1007/s00281-011-0288-2

40. Gailani D, Bane CE, Gruber A. Factor XI and contact activation as targets

for antithrombotic therapy. J Thromb Haemost. 2015;13: 1383–1395. doi:10.1111/jth.13005

41. Loghmani H, Conway EM. Exploring traditional and nontraditional roles for thrombomodulin. Blood. 2018;132: 148–158. doi:10.1182/blood-2017-12-768994

42. Hanson SR, Griffin JH, Harker LA, Kelly AB, Esmon CT, Gruber A. Antithrombotic effects of thrombin-induced activation of endogenous protein C in primates. J Clin Invest. 1993;92: 2003–2012. doi:10.1172/JCI116795

43. Griffin JH, Fernández JA, Gale AJ, Mosnier LO. Activated protein C. J Thromb Haemost. 2007;5 Suppl 1: 73–80. doi:10.1111/j.1538-7836.2007.02491.x

44. Cesarman-Maus G, Hajjar KA. Molecular mechanisms of fibrinolysis. Br J Haematol. 2005;129: 307–321. doi:10.1111/j.1365-2141.2005.05444.x

45. Puy C, Ngo ATP, Pang J, Keshari RS, Hagen MW, Hinds MT, et al. Endothelial PAI-1 (Plasminogen Activator Inhibitor-1) Blocks the Intrinsic Pathway of Coagulation, Inducing the Clearance and Degradation of FXIa (Activated Factor XI). Arterioscler Thromb Vasc Biol. 2019;39: 1390–1401. doi:10.1161/atvbaha.119.312619

46. Caro GG, Fitz-Gerald JM, Schroter RC. Arterial wall shear and distribution of early atheroma in man. Nature. 1969;223: 1159–1160. doi:10.1038/2231159a0

47. Caro CG. Discovery of the role of wall shear in atherosclerosis. Arterioscler Thromb Vasc Biol. 2009;29: 158–161. doi:10.1161/ATVBAHA.108.166736

48. Davies PF. Flow-mediated endothelial mechanotransduction. Physiol Rev. 1995;75: 519–60. doi:7624393

49. Langille BL, Adamson SL. Relationship between blood flow direction and endothelial cell orientation at arterial branch sites in rabbits and mice. Circ Res. 1981;48: 481–487. doi:10.1161/01.res.48.4.481

50. Dewey CF, Bussolari SR, Gimbrone MA, Davies PF. The Dynamic Response of Vascular Endothelial Cells to Fluid Shear Stress. J Biomech Eng. 1981;103: 177–185. doi:10.1115/1.3138276

51. Davies PF, Remuzzi A, Gordon EJ, Dewey CF, Gimbrone MA. Turbulent fluid shear stress induces vascular endothelial cell turnover in vitro. Proc Natl Acad Sci. 1986;83: 2114–2117. doi:10.1073/pnas.83.7.2114

52. Nerem RM, Levesque MJ, Cornhill JF. Vascular Endothelial Morphology as an Indicator of the Pattern of Blood Flow. J Biomech Eng. 1981;103: 172–176. doi:10.1115/1.3138275

53. Franke RP, Gräfe M, Schnittler H, Seiffge D, Mittermayer C, Drenckhahn D. Induction of human vascular endothelial stress fibres by fluid shear stress. Nature. 1984;307: 648–9. doi:10.1038/307648a0

54. Dekker RJ, Van Soest S, Fontijn RD, Salamanca S, De Groot PG, VanBavel E, et al. Prolonged fluid shear stress induces a distinct set of endothelial cell genes, most specifically lung Krüppel-like factor (KLF2). Blood. 2002;100: 1689–1698. doi:10.1182/blood-2002-01-0046

55. Kawanami D, Atkins GB, Hamik A, Jain MK. Role of Krüppel-like factors in shear stress-mediated vasoprotection. Hemodynamics and mechanobiology of endothelium. 2014. pp. 97–122. doi:10.1016/B978-0-12-385983-9.00004-1

56. Dekker RJ, van Thienen J V, Rohlena J, de Jager SC, Elderkamp YW, Seppen J, et al. Endothelial KLF2 links local arterial shear stress levels to the expression of vascular tone-regulating genes. Am J Pathol. 2005;167: 609–618. doi:10.1016/S0002-9440(10)63002-7

57. van Thienen J V., Fledderus JO, Dekker RJ, Rohlena J, van IJzendoorn GA, Kootstra NA, et al. Shear stress sustains atheroprotective endothelial KLF2 expression more potently than statins through mRNA stabilization. Cardiovasc Res. 2006;72: 231–240. doi:10.1016/j.cardiores.2006.07.008

58. Parmar KM, Larman HB, Dai G, Zhang Y, Wang ET, Moorthy SN, et al. Integration of flow-dependent endothelial phenotypes by Kruppel-like factor 2. J Clin Invest. 2006;116: 49–58. doi:10.1172/JCI24787

59. SenBanerjee S, Lin Z, Atkins GB, Greif DM, Rao RM, Kumar A, et al. KLF2 is a novel transcriptional regulator of endothelial proinflammatory activation. J Exp Med. 2004;199: 1305–1315. doi:10.1084/jem.20031132

60. Boon RA, Fledderus JO, Volger OL, Van Wanrooij EJA, Pardali E, Weesie F, et al. KLF2 suppresses TGF-β signaling in endothelium through induction of Smad7 and inhibition of AP-1. Arterioscler Thromb Vasc Biol. 2007;27: 532–539. doi:10.1161/01.ATV.0000256466.65450.ce

61. Mohan S, Mohan N, Sprague EA. Differential activation of NF-κB in human aortic endothelial cells conditioned to specific flow environments. Am J Physiol - Cell Physiol. 1997;273. doi:10.1152/ajpcell.1997.273.2.c572

62. Baeriswyl DC, Prionisti I, Peach T, Tsolkas G, Chooi KY, Vardakis J, et al. Disturbed flow induces a sustained, stochastic NF-κB activation which may support intracranial aneurysm growth in vivo. Sci Rep. 2019;9: 1–14. doi:10.1038/s41598-019-40959-y

63. Kallakuri S, Yu JA, Li J, Li Y, Weinstein BM, Nicoli S, et al. Endothelial cilia are essential for developmental vascular integrity in zebrafish. J Am Soc Nephrol. 2015;26: 864–875. doi:10.1681/ASN.2013121314

64. Iomini C, Tejada K, Mo W, Vaananen H, Piperno G. Primary cilia of human endothelial cells disassemble under laminar shear stress. J Cell Biol. 2004;164: 811–817. doi:10.1083/jcb.200312133

65. Van der Heiden K, Hierck BP, Krams R, de Crom R, Cheng C, Baiker M, et al. Endothelial primary cilia in areas of disturbed flow are at the base of atherosclerosis. Atherosclerosis. 2008;196: 542–550.

doi:10.1016/j.atherosclerosis.2007.05.030

66. Baeyens N, Mulligan-Kehoe MJ, Corti F, Simon DD, Ross TD, Rhodes JM, et al. Syndecan 4 is required for endothelial alignment in flow and atheroprotective signaling. Proc Natl Acad Sci U S A. 2014;111: 17308–17313. doi:10.1073/pnas.1413725111

67. Tarbell JM, Ebong E. Endothelial glycocalyx structure and role in mechanotransduction. In: Hsiai T, Blackman B, Jo H, editors. Hemodynamics and Mechanobiology of Endothelium. Singapore: World Scientific; 2010. pp. 69–95.

68. Weinbaum S, Tarbell JM, Damiano ER. The Structure and Function of the Endothelial Glycocalyx Layer. Annu Rev Biomed Eng. 2007;9: 121–167. doi:10.1146/annurev.bioeng.9.060906.151959

69. Givens C, Tzima E. Endothelial Mechanosignaling: Does One Sensor Fit All? Antioxidants Redox Signal. 2016;25: 373–388. doi:10.1089/ars.2015.6493

70. Fleming I, Fisslthaler B, Dixit M, Busse R. Role of PECAM-1 in the shear-stress-induced activation of Akt and the endothelial nitric oxide synthase (eNOS) in endothelial cells. J Cell Sci. 2005;118: 4103–4111. doi:10.1242/jcs.02541

71. Liu Y, Collins C, Kiosses WB, Murray AM, Joshi M, Shepherd TR, et al. A novel pathway spatiotemporally activates Rac1 and redox signaling in response to fluid shear stress. J Cell Biol. 2013;201: 863–873. doi:10.1083/jcb.201207115

72. Tzima E, Irani-Tehrani M, Kiosses WB, Dejana E, Schultz D a, Engelhardt B, et al. A mechanosensory complex that mediates the endothelial cell response to fluid shear stress. Nature. 2005;437: 426–431. doi:10.1038/nature03952

73. Matthews BD, Overby DR, Mannix R, Ingber DE. Cellular adaptation to mechanical stress: Role of integrins, Rho, cytoskeletal tension and mechanosensitive ion channels. J Cell Sci. 2006;119: 508–518. doi:10.1242/jcs.02760

74. Katsumi A, Orr AW, Tzima E, Schwartz MA. Integrins in Mechanotransduction. J Biol Chem. 2004;279: 12001–12004. doi:10.1074/jbc.R300038200

75. Collins C, Guilluy C, Welch C, O'Brien ET, Hahn K, Superfine R, et al. Localized tensional forces on PECAM-1 elicit a global mechanotransduction response via the integrin-RhoA pathway. Curr Biol. 2012;22: 2087–2094. doi:10.1016/j.cub.2012.08.051

76. Tzima E, Kiosses WB, Del Pozo MA, Schwartz MA. Localized Cdc42 activation, detected using a novel assay, mediates microtubule organizing center positioning in endothelial cells in response to fluid shear stress. J Biol Chem. 2003;278: 31020–31023. doi:10.1074/jbc.M301179200

77. Tzima E, Del Pozo MA, Shattil SJ, Chien S, Schwartz MA. Activation of integrins in endothelial cells by fluid shear stress mediates Rho-dependent cytoskeletal alignment. EMBO J. 2001;20: 4639–4647. doi:10.1093/emboj/20.17.4639

78. Anderson DEJ, Hinds MT. Endothelial cell micropatterning: Methods, effects, and applications. Ann Biomed Eng. 2011;39: 2329–2345. doi:10.1007/s10439-011-0352-z

79. Dike LE, Chen CS, Mrksich M, Tien J, Whitesides GM, Ingber DE. Geometric control of switching between growth, apoptosis, and differentiation during angiogenesis using micropatterned substrates. In Vitro Cell Dev Biol Anim. 1999;35: 441–448. doi:10.1007/s11626-999-0050-4

80. Vartanian KB, Kirkpatrick SJ, Hanson SR, Hinds MT. Endothelial cell cytoskeletal alignment independent of fluid shear stress on micropatterned surfaces. Biochem Biophys Res Commun. 2008;371: 787–92. doi:10.1016/j.bbrc.2008.04.167

81. Vartanian KB, Berny MA, McCarty OJT, Hanson SR, Hinds MT. Cytoskeletal structure regulates endothelial cell immunogenicity independent of fluid shear stress. Am J Physiol Physiol. 2010;298: C333–C341. doi:10.1152/ajpcell.00340.2009

82. Morgan JT, Wood JA, Shah NM, Hughbanks ML, Russell P, Barakat AI, et al. Integration of basal topographic cues and apical shear stress in vascular endothelial cells. Biomaterials. 2012;33: 4126–35. doi:10.1016/j.biomaterials.2012.02.047

83. Schieber R, Lasserre F, Hans M, Fernández-Yagüe M, Díaz-Ricart M, Escolar G, et al. Direct Laser Interference Patterning of CoCr Alloy Surfaces to Control Endothelial Cell and Platelet Response for Cardiovascular Applications. Adv Healthc Mater. 2017;6: 1–14. doi:10.1002/adhm.201700327

84. Liliensiek SJ, Wood J a., Yong J, Auerbach R, Nealey PF, Murphy CJ. Modulation of human vascular endothelial cell behaviors by nanotopographic cues. Biomaterials. 2010;31: 5418–5426. doi:10.1016/j.biomaterials.2010.03.045

85. Cutiongco MFA, Chua BMX, Neo DJH, Rizwan M, Yim EKF. Functional differences between healthy and diabetic endothelial cells on topographical cues. Biomaterials. 2018;153: 70–84. doi:10.1016/j.biomaterials.2017.10.037

86. Vandrangi P, Gott SC, Kozaka R, Rodgers VGJ, Rao MP. Comparative Endothelial Cell Response on Topographically Patterned Titanium and Silicon Substrates with Micrometer to Sub-Micrometer Feature Sizes. Pisignano D, editor. PLoS One. 2014;9: e111465. doi:10.1371/journal.pone.0111465

87. Asahara T, Murohara T, Sullivan A, Silver M, van der Zee R, Li T, et al. Isolation of putative progenitor endothelial cells for angiogenesis. Science. 1997;275: 964–7. doi:10.1126/science.275.5302.964

88. Pearson JD. Endothelial progenitor cells-an evolving story. Microvasc Res. 2010;79: 162–168. doi:10.1016/j.mvr.2009.12.004

89. Medina RJ, Barber CL, Sabatier F, Dignat-George F, Melero-Martin JM, Khosrotehrani K, et al. Endothelial progenitors: a consensus statement on nomenclature. Stem Cells Transl Med. 2017;6: 1316–1320. doi:10.1002/sctm.16-0360

90. Lin Y, Weisdorf DJ, Solovey A, Hebbel RP. Origins of circulating endothelial cells and endothelial outgrowth from blood. J Clin Invest. 2000;105: 71–77. doi:10.1172/JCI8071

91. Tura O, Skinner EM, Barclay R, Samuel K, Gallagher RCJ, Brittan M, et al. Late outgrowth endothelial cells resemble mature endothelial cells and are not derived from bone marrow. Stem Cells. 2013;31. doi:10.1002/stem.1280

92. Toshner M, Dunmore BJ, McKinney EF, Southwood M, Caruso P, Upton PD, et al. Transcript analysis reveals a specific HOX signature associated with positional identity of human endothelial cells. PLoS One. 2014;9. doi:10.1371/journal.pone.0091334

93. Peichev M, Naiyer AJ, Pereira D, Zhu Z, Lane WJ, Williams M, et al. Expression of VEGFR-2 and AC133 by circulating human CD34+ cells identifies a population of functional endothelial precursors. Blood. 2000;95: 952–958. doi:10.1182/blood.V95.3.952.003k27_952_958

94. Case J, Mead LE, Bessler WK, Prater D, White HA, Saadatzadeh MR, et al. Human CD34+AC133+VEGFR-2+ cells are not endothelial progenitor cells but distinct, primitive hematopoietic progenitors. Exp Hematol. 2007;35: 1109–1118. doi:10.1016/j.exphem.2007.04.002

95. Starke RD, Paschalaki KE, Dyer CEF, Harrison-lavoie KJ, Cutler JA, Mckinnon TAJ, et al. Cellular and molecular basis of von Willebrand disease : studies on blood outgrowth endothelial cells. Blood. 2015;121: 2773–2785. doi:10.1182/blood-2012-06-435727.The

96. Ingram DA, Lien IZ, Mead LE, Estes M, Prater DN, Derr-Yellin E, et al. In vitro hyperglycemia or a diabetic intrauterine environment reduces neonatal endothelial colony-forming cell numbers and function. Diabetes. 2008;57: 724–731. doi:10.2337/db07-1507

97. Paschalaki KE, Randi AM. Recent advances in endothelial colony forming cells toward their use in clinical translation. Front Med. 2018;5: 1–12. doi:10.3389/fmed.2018.00295

98. Schwarz TM, Leicht SF, Radic T, Rodriguez-Araboalaza I, Hermann PC, Berger F, et al. Vascular incorporation of endothelial colony-forming cells is essential for functional recovery of murine ischemic tissue following cell

therapy. Arterioscler Thromb Vasc Biol. 2012;32: 13–21. doi:10.1161/ATVBAHA.111.239822

99. Kang KT, Lin RZ, Kuppermann D, Melero-Martin JM, Bischoff J. Endothelial colony forming cells and mesenchymal progenitor cells form blood vessels and increase blood flow in ischemic muscle. Sci Rep. 2017;7: 1–11. doi:10.1038/s41598-017-00809-1

100. Moubarik C, Guillet B, Youssef B, Codaccioni JL, Piercecchi MD, Sabatier F, et al. Transplanted Late Outgrowth Endothelial Progenitor Cells as Cell Therapy Product for Stroke. Stem Cell Rev Reports. 2011;7: 208–220. doi:10.1007/s12015-010-9157-y

101. Taljaard M, Ward MR, Kutryk MJB, Courtman DW, Camack NJ, Goodman SG, et al. Rationale and design of Enhanced Angiogenic Cell Therapy in Acute Myocardial Infarction (ENACT-AMI): The first randomized placebo-controlled trial of enhanced progenitor cell therapy for acute myocardial infarction. Am Heart J. 2010;159: 354–360. doi:10.1016/j.ahj.2009.12.021

102. Glynn JJ, Hinds MT. Endothelial outgrowth cells: function and performance in vascular grafts. Tissue Eng Part B Rev. 2013;20. doi:10.1089/ten.teb.2013.0285

103. Glynn JJ, Hinds MT. Endothelial outgrowth cells regulate coagulation, platelet accumulation, and respond to tumor necrosis factor similar to carotid endothelial cells. Tissue Eng Part A. 2015;21: 174–182. doi:10.1089/ten.tea.2014.0032

104. Ensley AE, Nerem RM, Anderson DEJ, Hanson SR, Hinds MT. Fluid shear stress alters the hemostatic properties of endothelial outgrowth cells. Tissue Eng Part A. 2012;18: 127–36. doi:10.1089/ten.TEA.2010.0290

105. Ankeny RF, Hinds MT, Nerem RM. Dynamic shear stress regulation of inflammatory and thrombotic pathways in baboon endothelial outgrowth cells. Tissue Eng Part A. 2013;19: 1573–82. doi:10.1089/ten.TEA.2012.0300

106. Anderson DEJ, Glynn JJ, Song HK, Hinds MT. Engineering an endothelialized vascular graft: a rational approach to study design in a non-human primate model. PLoS One. 2014;9: e115163. doi:10.1371/journal.pone.0115163

107. Vartanian KB, Kirkpatrick SJ, McCarty OJT, Vu TQ, Hanson SR, Hinds MT. Distinct extracellular matrix microenvironments of progenitor and carotid endothelial cells. J Biomed Mater Res Part A. 2009;91A: 528–539. doi:10.1002/jbm.a.32225

108. Anderson DEJ, McKenna K a, Glynn JJ, Marzec U, Hanson SR, Hinds MT. Thrombotic Responses of Endothelial Outgrowth Cells to Protein-Coated Surfaces. Cells Tissues Organs. 2014;199: 238–248. doi:10.1159/000368223

109. Harker LA, Hanson SR, Kirkman TR. Experimental Arterial

Thromboembolism in Baboons. J Clin Invest. 1979;64: 559–569. doi:10.1172/JCI109494

110. Harker LA, Marzec UM, Kelly AB, Chronos NRF, Sundell IB, Hanson SR, et al. Clopidogrel Inhibition of Stent, Graft, and Vascular Thrombogenesis With Antithrombotic Enhancement by Aspirin in Nonhuman Primates. Circulation. 1998;98: 2461–2469. doi:10.1161/01.CIR.98.22.2461

111. Peng H, Schlaich EM, Row S, Andreadis ST, Swartz DD. A novel ovine ex vivo arteriovenous shunt model to test vascular implantability. Cells Tissues Organs. 2011;195: 108–121. doi:10.1159/000331415

112. Anderson DEJ, Hinds MT. Extracellular matrix production and regulation in micropatterned endothelial cells. Biochem Biophys Res Commun. 2012;427: 159–164. doi:10.1016/j.bbrc.2012.09.034

113. Schindelin J, Arganda-Carreras I, Frise E, Kaynig V, Longair M, Pietzsch T, et al. Fiji: An open-source platform for biological-image analysis. Nat Methods. 2012;9: 676–682. doi:10.1038/nmeth.2019

114. Koerker DJ, Harker LA, Goodner CJ. Effects of Somatostatin on Hemostasis in Baboons. N Engl J Med. 1975;293: 476–479. doi:10.1056/NEJM197509042931004

115. Pashneh-Tala S, MacNeil S, Claeyssens F. The tissue-engineered vascular graft—past, present, and future. Tissue Eng Part B Rev. 2015;22: ten.teb.2015.0100. doi:10.1089/ten.teb.2015.0100

116. Klinkert P, Post PN, Breslau PJ, van Bockel JH. Saphenous vein versus PTFE for above-knee femoropopliteal bypass. A review of the literature. Eur J Vasc Endovasc Surg. 2004;27: 357–362. doi:10.1016/j.ejvs.2003.12.027

117. Deutsch M, Meinhart J, Fischlein T, Preiss P, Zilla P. Clinical autologous in vitro endothelialization of infrainguinal ePTFE grafts in 100 patients: A 9-year experience. Surgery. 1999;126: 847–855. doi:10.1016/S0039-6060(99)70025-5

118. Deutsch M, Meinhart J, Zilla P, Howanietz N, Gorlitzer M, Froeschl A, et al. Long-term experience in autologous in vitro endothelialization of infrainguinal ePTFE grafts. J Vasc Surg. 2009;49: 352–362. doi:10.1016/j.jvs.2008.08.101

119. Meier LA, Syedain ZH, Lahti MT, Johnson SS, Chen MH, Hebbel RP, et al. Blood outgrowth endothelial cells alter remodeling of completely biological engineered grafts implanted into the sheep femoral artery. J Cardiovasc Transl Res. 2014;7: 242–249. doi:10.1007/s12265-013-9539-z

120. Poole JC, Florey HW. Changes in the endothelium of the aorta and the behaviour of macrophages in experimental atheroma of rabbits. J Pathol Bacteriol. 1958;75: 245–251. doi:10.1002/path.1700750202

121. Walpola PL, Gotlieb AI, Cybulsky MI, Langille BL. Expression of ICAM-1

and VCAM-1 and monocyte adherence in arteries exposed to altered shear stress. Arterioscler Thromb Vasc Biol. 1995;15: 2–10. doi:10.1161/01.ATV.15.1.2

122. Loth F, Fischer PF, Hisham S, Bassiouny HS, Hisham S. Blood flow in end-to-side anastomoses. Annu Rev Fluid Mech. 2008;40: 1–26. doi:10.1146/annurev.fluid.40.111406.102119

123. Bassiouny HS, White S, Glagov S, Choi E, Giddens DP, Zarins CK. Anastomotic intimal hyperplasia: Mechanical injury or flow induced. J Vasc Surg. 1992;15: 708–717. doi:10.1016/0741-5214(92)90019-5

124. Tan JL, Liu W, Nelson CM, Raghavan S, Chen CS. Simple approach to micropattern cells on common culture substrates by tuning substrate wettability. Tissue Eng. 2004;10: 865–872. doi:10.1089/1076327041348365

125. Lin X, Helmke BP. Micropatterned structural control suppresses mechanotaxis of endothelial cells. Biophys J. 2008;95: 3066–3078. doi:10.1529/biophysj.107.127761

126. R Core Team. R: A language and environment for statistical computing. R Foundation for Statistical Computing; 2019.

127. Bray A, Ismay C, Baumer B, Cetinkaya-Rundel M. infer: Tidy Statistical Inference. 2018.

128. Hothorn T, Bretz F, Westfall P. Simultaneous inference in general parametric models. Biometrical J. 2008;50: 346–363.

129. Ernst MD. Permutation Methods: A Basis for Exact Inference. Stat Sci. 2004;19: 676–685. doi:10.1214/088342304000000396

130. Hinds MT, Ma M, Tran N, Ensley AE, Kladakis SM, Vartanian KB, et al. Potential of baboon endothelial progenitor cells for tissue engineered vascular grafts. J Biomed Mater Res Part A. 2008;86A: 804–812. doi:10.1002/jbm.a.31672

131. Kues WA, Anger M, Carnwath JW, Paul D, Motlik J, Niemann H. Cell cycle synchronization of porcine fetal fibroblasts: effects of serum deprivation and reversible cell cycle inhibitors. Biol Reprod. 2000;62: 412–419. doi:10.1095/biolreprod62.2.412

132. Egorova AD, DeRuiter MC, De Boer HC, Van De Pas S, Gittenberger-De Groot AC, Van Zonneveld AJ, et al. Endothelial colony-forming cells show a mature transcriptional response to shear stress. Vitr Cell Dev Biol - Anim. 2012;48: 21–29. doi:10.1007/s11626-011-9470-z

133. Gebrane-Younès J, Drouet L, Caen JP, Orcel L. Heterogeneous distribution of Weibel-Palade bodies and von Willebrand factor along the porcine vascular tree. Am J Pathol. 1991;139: 1471–84.

134. Cutiongco MFA, Goh SH, Aid-Launais R, Le Visage C, Low HY, Yim EKF. Planar and tubular patterning of micro and nano-topographies on poly(vinyl

alcohol) hydrogel for improved endothelial cell responses. Biomaterials. 2016;84: 184–195. doi:10.1016/j.biomaterials.2016.01.036

135. Paschalaki KE, Starke RD, Hu Y, Mercado N, Margariti A, Gorgoulis VG, et al. Dysfunction of endothelial progenitor cells from smokers and chronic obstructive pulmonary disease patients due to increased dna damage and senescence. Stem Cells. 2013;31: 2813–2826. doi:10.1002/stem.1488

136. Kohn JC, Zhou DW, Bordeleau F, Zhou AL, Mason BN, Mitchell MJ, et al. Cooperative effects of matrix stiffness and fluid shear stress on endothelial cell behavior. Biophys J. 2015;108: 471–478. doi:10.1016/j.bpj.2014.12.023

137. Scott DM, Griffin B, Pepper DS, Barnes MJ. The binding of purified factor VIII/von Willebrand factor to collagens of differing type and form. Thromb Res. 1981;24: 467–472.

138. Anderson DEJ, Truong KP, Hagen MW, Yim EKF, Hinds MT. Biomimetic Modification of Poly(vinyl alcohol): Encouraging Endothelialization and Preventing Thrombosis with Antiplatelet Monotherapy. Acta Biomater. 2019; 1–9. doi:10.1016/J.ACTBIO.2019.01.008

139. de Mel A, Bolvin C, Edirisinghe M, Hamilton G, Seifalian AM. Development of cardiovascular bypass grafts: endothelialization and applications of nanotechnology. Expert Rev Cardiovasc Ther. 2008;6: 1259–77. doi:10.1586/14779072.6.9.1259

140. Hagen MW, Hinds MT. Static spatial growth restriction micropatterning of endothelial colony forming cells influences their morphology and gene expression. PLoS One. 2019;14: e0218197. doi:10.1371/journal.pone.0218197

141. Dreier B, Gasiorowski JZ, Morgan JT, Nealey PF, Russell P, Murphy CJ. Early responses of vascular endothelial cells to topographic cues. Am J Physiol Cell Physiol. 2013;305: C290-8. doi:10.1152/ajpcell.00264.2012

142. Jeon H, Tsui JH, Jang SI, Lee JH, Park S, Mun K, et al. Combined effects of substrate topography and stiffness on endothelial cytokine and chemokine secretion. ACS Appl Mater Interfaces. 2015;7: 4525–4532. doi:10.1021/acsami.5b00554

143. Ding Y, Yang M, Yang Z, Luo R, Lu X, Huang N, et al. Cooperative control of blood compatibility and re-endothelialization by immobilized heparin and substrate topography. Acta Biomater. 2015;15: 150–163. doi:10.1016/j.actbio.2014.12.014

144. Pinheiro J, Bates D, DebRoy S, Sarkar D, Team RC. nlme: Linear and Nonlinear Mixed Effects Models. 2016. Available: http://cran.r-project.org/package=nlme

145. Kovacevic J, Rohde GK. Overview of image analysis tools and tasks for microscopy. In: Rittscher J, Machiraju R, Wong STC, editors. Microscopic Image Analysis for Life Science Applications. Boston, MA: Artech House;

2008. pp. 49–84.

146. Osborn E a, Rabodzey A, Dewey CF, Hartwig JH. Endothelial actin cytoskeleton remodeling during mechanostimulation with fluid shear stress. Am J Physiol Cell Physiol. 2006;290: C444–C452. doi:10.1152/ajpcell.00218.2005

147. Noria S, Xu F, McCue S, Jones M, Gotlieb AI, Langille BL. Assembly and reorientation of stress fibers drives morphological changes to endothelial cells exposed to shear stress. Am J Pathol. 2004;164: 1211–1223. doi:10.1016/S0002-9440(10)63209-9

148. Girard PR, Nerem RM. Endothelial cell signaling and cytoskeletal changes in response to shear stress. Front Med Biol Eng. 1993;5: 31–36.

149. McCormick ME, Goel R, Fulton D, Oess S, Newman D, Tzima E. Platelet-endothelial cell adhesion molecule-1 regulates endothelial NO synthase activity and localization through signal transducers and activators of transcription 3-dependent NOSTRIN expression. Arterioscler Thromb Vasc Biol. 2011;31: 643–649. doi:10.1161/ATVBAHA.110.216200

150. Nakayama KH, Surya VN, Gole M, Walker TW, Yang W, Lai ES, et al. Nanoscale Patterning of Extracellular Matrix Alters Endothelial Function under Shear Stress. Nano Lett. 2016;16: 410–419. doi:10.1021/acs.nanolett.5b04028

151. Uttayarat P, Perets A, Li M, Pimton P, Stachelek SJ, Alferiev I, et al. Micropatterning of three-dimensional electrospun polyurethane vascular grafts. Acta Biomater. 2010;6: 4229–4237. doi:10.1016/j.actbio.2010.06.008

152. Rana D, Keerthana R, Leena M, Jiménez C, Campos J, Ibarra P, et al. Surface functionalization of nanobiomaterials for application in stem cell culture, tissue engineering and regenerative medicine. Biotechnol Prog. 2016; n/a-n/a. doi:10.1002/btpr.2262

153. Sprague EA, Tio F, Ahmed SH, Granada JF, Bailey SR. Impact of parallel micro-engineered stent grooves on endothelial cell migration, proliferation, and function: An in vivo correlation study of the healing response in the coronary swine model. Circ Cardiovasc Interv. 2012;5: 499–507. doi:10.1161/CIRCINTERVENTIONS.111.967901

154. Vartanian KB. Role of Cytoskeletal Alignment, Independent of Fluid Shear Stress, in Endothelial Cell Functions. 2009.

155. Wang C, Baker BM, Chen CS, Schwartz MA. Endothelial Cell Sensing of Flow Direction. Arterioscler Thromb Vasc Biol. 2013;33: 2130–2136. doi:10.1161/ATVBAHA.113.301826

156. Starke RM, Turk A, Ding D, Crowley RW, Liu KC, Chalouhi N, et al. Technology developments in endovascular treatment of intracranial aneurysms. J Neurointerv Surg. 2016;8: 135–44. doi:10.1136/neurintsurg-2014-011475

157. Alderazi YJ, Shastri D, Kass-Hout T, Prestigiacomo CJ, Gandhi CD. Flow Diverters for Intracranial Aneurysms. Stroke Res Treat. 2014;2014: 1–12. doi:10.1155/2014/415653

158. Zuckerman SL, Eli IM, Morone PJ, Dewan MC, Mocco J. Novel technologies in the treatment of intracranial aneurysms. Neurol Res. 2014;36: 368–82. doi:10.1179/1743132814Y.0000000318

159. Phillips TJ, Wenderoth JD, Phatouros CC, Rice H, Singh TP, Devilliers L, et al. Safety of the Pipeline Embolization Device in Treatment of Posterior Circulation Aneurysms. Am J Neuroradiol. 2012;33: 1225–1231. doi:10.3174/ajnr.A3166

160. Kan P, Siddiqui AH, Veznedaroglu E, Liebman KM, Binning MJ, Dumont TM, et al. Early Postmarket Results After Treatment of Intracranial Aneurysms With the Pipeline Embolization Device. Neurosurgery. 2012;71: 1080–1088. doi:10.1227/NEU.0b013e31827060d9

161. Szikora I, Berentei Z, Kulcsar Z, Marosfoi M, Vajda ZS, Lee W, et al. Treatment of Intracranial Aneurysms by Functional Reconstruction of the Parent Artery: The Budapest Experience with the Pipeline Embolization Device. Am J Neuroradiol. 2010;31: 1139–1147. doi:10.3174/ajnr.A2023

162. Kocer N, Islak C, Kizilkilic O, Kocak B, Saglam M, Tureci E. Flow Re-direction Endoluminal Device in treatment of cerebral aneurysms: initial experience with short-term follow-up results. J Neurosurg. 2014;120: 1158–1171. doi:10.3171/2014.1.JNS131442

163. Poncyljusz W, Sagan L, Safranow K, Rać M. Initial experience with implantation of novel dual layer flow-diverter device FRED. Videosurgery Other Miniinvasive Tech. 2013;3: 258–264. doi:10.5114/wiitm.2011.35794

164. Murayama Y, Nien YL, Duckwiler G, Gobin YP, Jahan R, Frazee J, et al. Guglielmi Detachable Coil embolization of cerebral aneurysms: 11 years' experience. J Neurosurg. 2003;98: 959–966. doi:10.3171/jns.2003.98.5.0959

165. Shapiro M, Becske T, Sahlein D, Babb J, Nelson PK. Stent-Supported Aneurysm Coiling: A Literature Survey of Treatment and Follow-Up. Am J Neuroradiol. 2012;33: 159–163. doi:10.3174/ajnr.A2719

166. Leung GKK, Tsang ACO, Lui WM. Pipeline embolization device for intracranial aneurysm: A systematic review. Clin Neuroradiol. 2012;22: 295–303. doi:10.1007/s00062-012-0178-6

167. Mohlenbruch MA, Herweh C, Jestaedt L, Stampfl S, Schonenberger S, Ringleb PA, et al. The FRED Flow-Diverter Stent for Intracranial Aneurysms: Clinical Study to Assess Safety and Efficacy. Am J Neuroradiol. 2015;36: 1155–1161. doi:10.3174/ajnr.A4251

168. Yamamoto K, Hokimoto S, Chitose T, Morita K, Ono T, Kaikita K, et al. Impact of CYP2C19 polymorphism on residual platelet reactivity in patients with coronary heart disease during antiplatelet therapy. J Cardiol. 2011;57:

194–201. doi:10.1016/j.jjcc.2010.10.007

169. Campbell EJ, O'Byrne V, Stratford PW, Quirk I, Vick TA, Wiles MC, et al. Biocompatible surfaces using methacryloylphophoylcholine laurylmethacrylate copolymer. ASAIO Journal. 1994. pp. M853–M857.

170. Chen C, Lumsden AB, Ofenloch JC, Noe B, Campbell EJ, Stratford PW, et al. Phosphorylcholine coating of ePTFE grafts reduces neointimal hyperplasia in canine model. Ann Vasc Surg. 1997;11: 74–9. doi:10.1007/s100169900013

171. Girdhar G, Li J, Kostousov L, Wainwright J, Chandler WL. In-vitro thrombogenicity assessment of flow diversion and aneurysm bridging devices. J Thromb Thrombolysis. 2015;40: 437–443. doi:10.1007/s11239-015-1228-0

172. Hanson SR, Harker LA, Ratner BD, Hoffman AS. In vivo evaluation of artificial surfaces with a nonhuman primate model of arterial thrombosis. J Lab Clin Med. 1980;95: 289–304.

173. Lieber BB, Stancampiano AP, Wakhloo AK. Alteration of hemodynamics in aneurysm models by stenting: Influence of stent porosity. Ann Biomed Eng. 1997;25: 460–469. doi:10.1007/BF02684187

174. Gruber A, Hanson SR. Factor XI – dependence of surface- and tissue factor – initiated thrombus propagation in primates. Blood. 2003;102: 953. doi:10.1182/blood-2003-01-0324.Supported

175. Hagen MW, Girdhar G, Wainwright J, Hinds MT. Thrombogenicity of flow diverters in an ex vivo shunt model: Effect of phosphorylcholine surface modification. J Neurointerv Surg. 2017;9: 1006–1011. doi:10.1136/neurintsurg-2016-012612

176. Lorentz CU, Verbout NG, Wallisch M, Hagen MW, Shatzel JJ, Olson SR, et al. Contact Activation Inhibitor and Factor XI Antibody, AB023, Produces Safe, Dose-Dependent Anticoagulation in a Phase 1 First-In-Human Trial. Arterioscler Thromb Vasc Biol. 2019; 1–11. doi:10.1161/ATVBAHA.118.312328

177. Chiang HY, Korshunov VA, Serour A, Shi F, Sottile J. Fibronectin is an important regulator of flow-induced vascular remodeling. Arterioscler Thromb Vasc Biol. 2009;29: 1074–1079. doi:10.1161/ATVBAHA.108.181081

178. Harris GM, Madigan NN, Lancaster KZ, Enquist LW, Windebank AJ, Schwartz J, et al. Nerve Guidance by a Decellularized Fibroblast Extracellular Matrix. Matrix Biol. 2017;60–61: 176–189. doi:10.1016/j.matbio.2016.08.011

179. Van den Berg BM, Vink H, Spaan JAE. The endothelial glycocalyx protects against myocardial edema. Circ Res. 2003;92: 592–594. doi:10.1161/01.RES.0000065917.53950.75

180. Singh A, Satchell SC, Neal CR, McKenzie EA, Tooke JE, Mathieson PW. Glomerular endothelial glycocalyx constitutes a barrier to protein permeability. J Am Soc Nephrol. 2007;18: 2885–93. doi:10.1681/ASN.2007010119

Biographical sketch

Peer-reviewed publications:

Hagen MW, Hinds MT. Static spatial growth restriction micropatterning of endothelial colony forming cells influences their morphology and gene expression. *PLoS ONE* 2019, 14(6) e0218197.

Anderson DEJ, Truong KP, **Hagen MW,** Yim EKF, Hinds MT. Biomimetic modification of poly(vinyl alcohol): encouraging endothelialization and prevention thrombosis with antiplatelet monotherapy. *Acta biomater.* 2019 86:291-299.

Pohan G, Chevallier P, Anderson DEJ, Tse JW, Yao Y, **Hagen MW**, Mantovani D, Hinds MT, Yim EKF. Luminal plasma treatment for small diameter polyvinyl alcohol tubular scaffolds. *Front Bioeng Biotechnol.* 2019 7:117.

Lorentz CU, Verbout NG, Wallisch M, **Hagen MW,** Shatzel JJ, Olson SR, Puy C, Hinds MT, McCarty OJT, Gailani D, Gruber A, Tucker EI. Contact activation inhibitor and factor XI antibody, AB023, produces safe, dose-dependent anticoagulation in a phase-1 first-in-human trial. *Ateriosclerr Thromb Vasc Biol.* 2019 39(4):799-809.

Puy C, Ngo ATP, Pang J, Keshari RS, **Hagen MW,** Hinds MT, Gailani D, Gruber A, Lupu F, McCarty OJT. Endothelial PAI-1 (plasminogen activator inhibitor-1) blocks the intrinsic pathway of coagulation, inducing he clearance and degredation of FXIa (activated factor XI). *Arterioscler Thromb Vasc Biol.* 2019 39(7):1390-1401.

Hagen MW, Girdhar G, Wainwright J, Hinds MT. Thrombogenicity of flow diverters in an ex vivo shunt model: effect of phosphorylcholine surface modification. *J Neurointerv surg.* 2017 9(10):1006-1011.

Hagen MW, Riddle A, McClendon E, Gong X, Shaver D, Srivastava T, Dean JM, Bai JZ, Fowke TM, Gunn AJ, Jones DF, Sherman LS, Grafe MR, Hohimer AR, Back SA. Role of recurrent hypoxia-ischemia in preterm white matter injury severity. *PLoS ONE.* 2014 9(11): e112800.

McClendon E, Wang K, Degener-O'Brien K, **Hagen MW**, Gong X, Ngyuen T, Wu WW, Maylie J, Back SA. Transient hypoxemia disrupts anatomical and functional maturation of preterm fetal ovine CA1 pyramidal neurons. *J Neurosci* 2019 39(40):7853-7871.

Srivastava T, Diba P, Dean JM, Banine F, Shaver D, **Hagen MW**, Gong X, Su W, Emery B, Marks DL, Harris EN, Baggenstoss B, Weigel PH, Sherman LS, Back SA. A TLR/AKT/FoxO3 immune tolerance-like pathway disrupts the repair capacity of oligodendrocyte progenitors. *J Clin Invest* 2018 128(5): 2025-2041.

McClendon E, Chen K, Gong X, Sharifnia E, **Hagen MW**, Cai V, Shaver DC, Riddle A, Dean JM, Gunn AJ, Mohr C, Kaplan JS, Rossi DJ, Kroenke CD, Hohimer AR, Back SA. Prenatal cerebral ischemia triggers dysmaturation of caudate projection neurons. *Ann Neurol.* 2014 75(4):508-24.

Dean JM, McClendon E, Hansen K, Azimi-Zonooz A, Chen K, Riddle A, Gong X, Sharifnia E, **Hagen MW**, Ahmad T, Leigland LA, Hohimer AR, Kronke CD, Back SA. Prenatal cerebral ischemia disrupts MRI-defined cortical microstructure through disturbances in neuronal arborization. *Sci Transl Med.* 2013 5(168): 168ra7.

Sheets L, **Hagen MW**, Nicolson T., Characterizatino of ribeye subunits in zebrafish hair cells reveals that exogenous ribeye B-domain and CtBP1 localize to the basal ends of synaptic ribbons. *PLoS ONE.* 2014 9(9):e107256.

Selected conference abstracts:

Presenting author is underlined.

Hagen, M.W., Louey, S., Davis, B., Carbone, L., Barnes, A.P., Giraud, G., Thornburg, K., Hinds, M.T. (October 2019) "Development of a novel guinea pig model of transgenerational atherosclerotic risk driven by maternal malnutrition", Poster given at the Vascular Biology 2019 NAVBO annual meeting, Pacific Grove, CA.

Hagen, M.W., Hinds, M.T. (October 2019) "Static topographical micropatterning of endothelial colony forming cells drives alignment without elongation or atheroprotection", Poster given at the Vascular Biology 2019 NAVBO annual meeting, Pacific Grove, CA.

Hagen, M.W., Hinds, M.T. (October 2019) "Static micropatterning modalities modify morphology & function of endothelial colony forming cells", Poster given at the 51st Biomedical Engineering Society Annual Meeting, Philadelphia, PA.

Hagen, M.W., Hinds, M.T. (October 2019) "Individual predictors of biomaterial thrombogenicity in an ex vivo shunt model", Poster given at the 51st Biomedical Engineering Society Annual Meeting, Philadelphia, PA.

Hagen, M.W., Hinds, M.T. (April 2019) "Endothelial colony forming cell (ECFC) micropatterning influences function indpendent of fluid shear", Poster given at the First Annual Blood Microenvironment Research Retreat, Portland, OR.

Hagen, M.W., Hinds, M.T. (October 2018) "Endothelial colony forming cell (ECFC) micropatterning influences function independent of fluid shear", Poster given at the 50th Biomedical Engineering Society Annual Meeting, Atlanta, GA.

Hagen, M.W., Hinds, M.T. (May 2018) "Growth restrictive micropatterning enhances potential endothelial colony forming cell performance on cardiovascular biomaterials by lowering immunogenicity", Talk given at the 34th Annual Meeting of the Canadian Biomaterials Society, Victoria, BC, Canada.

Hagen, M.W., Hinds, M.T. (October 2017) "Micropatterning induced morphological and functional alterations of endothelial colony forming cells (ECFCs)", Poster given at Vascular Biology 2017, Pacific Grove, CA.

Hagen, M.W., Van, T., Hinds, M.T. (July 2017) "Micropatterning induced alterations of endothelial outgrowth cells", Poster given at 26th Biennial Congress of the International Society on Thrombosis and Haemostasis, Berlin, Germany.

Hagen, M.W., Anderson, D.E., Hinds, M.T. (June 2017), "Micropatterning drives endothelial cell alignment and function on vascular grafts", SB3C 2017, Tuscon, AZ.

Hagen, M.W., Girdhar, G., Wainwright, J., Hinds, M.T. (April, 2017) "Novel covalent surface modifications reduce flow diverter thrombogenicity in an ex vivo shunt model", Poster given at the KCVI Research Retreat 2017, Portland, OR.

Hagen, M.W., Girdhar, G., Wainwright, J., Hinds, M.T. (November, 2016) "Phosphorylcholine surface modification reduces thrombogenicity of flow diverters in an ex vivo shunt model", Poster given at 19th International Vascular Biology Meeting, Boston, MA.